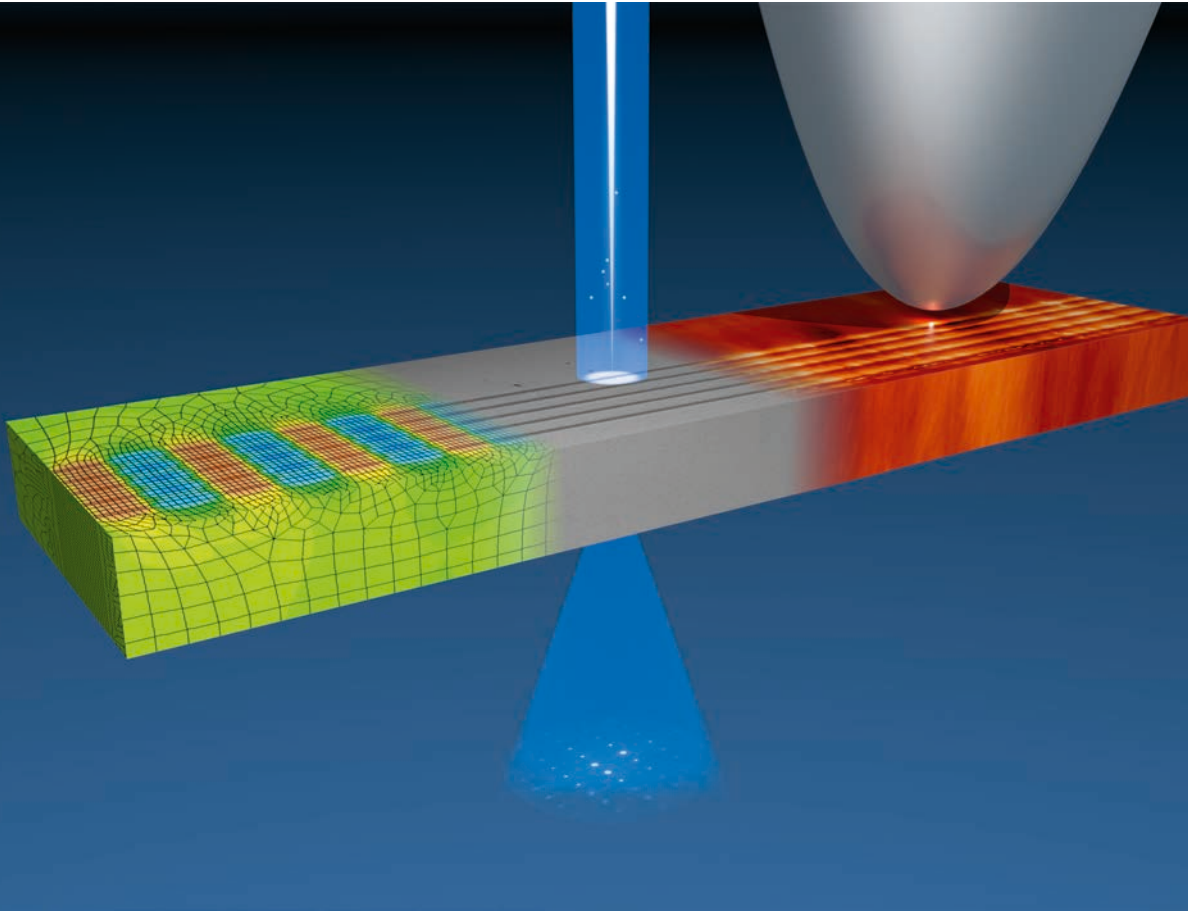


# Investigation of ternary nitride semiconductor alloys by scanning tunneling microscopy

Verena Portz



Information  
Band/ Volume 48  
ISBN 978-3-95806-232-0





Forschungszentrum Jülich GmbH  
Peter Grünberg Institute (PGI)  
Microstructure Research (PGI-5)

# Investigation of ternary nitride semiconductor alloys by scanning tunneling microscopy

Verena Portz

Schriften des Forschungszentrums Jülich  
Reihe Information / Information

Band / Volume 48

---

ISSN 1866-1777

ISBN 978-3-95806-232-0

Bibliographic information published by the Deutsche Nationalbibliothek.  
The Deutsche Nationalbibliothek lists this publication in the Deutsche  
Nationalbibliografie; detailed bibliographic data are available in the  
Internet at <http://dnb.d-nb.de>.

Publisher and  
Distributor: Forschungszentrum Jülich GmbH  
Zentralbibliothek  
52425 Jülich  
Tel: +49 2461 61-5368  
Fax: +49 2461 61-6103  
Email: [zb-publikation@fz-juelich.de](mailto:zb-publikation@fz-juelich.de)  
[www.fz-juelich.de/zb](http://www.fz-juelich.de/zb)

Cover Design: Grafische Medien, Forschungszentrum Jülich GmbH

Printer: Grafische Medien, Forschungszentrum Jülich GmbH

Copyright: Forschungszentrum Jülich 2017

Schriften des Forschungszentrums Jülich  
Reihe Information / Information, Band / Volume 48

D 82 (Diss. RWTH Aachen University, 2017)

ISSN 1866-1777  
ISBN 978-3-95806-232-0

Vollständig frei verfügbar über das Publikationsportal des Forschungszentrums Jülich (JuSER)  
unter [www.fz-juelich.de/zb/openaccess](http://www.fz-juelich.de/zb/openaccess).



This is an Open Access publication distributed under the terms of the [Creative Commons Attribution License 4.0](https://creativecommons.org/licenses/by/4.0/),  
which permits unrestricted use, distribution, and reproduction in any medium, provided the original work is properly cited.

# Contents

<b>1</b>	<b>Introduction</b>	<b>7</b>
<b>2</b>	<b>Theoretical background</b>	<b>11</b>
2.1	Scanning tunneling microscopy . . . . .	11
2.1.1	One dimensional tunneling effect . . . . .	11
2.1.2	Tunnel current . . . . .	14
2.1.3	WKB approximation of the tunnel current . . . . .	17
2.2	Simulation of the tunnel current . . . . .	19
2.2.1	Derivation of the tip induced band bending . . . . .	19
2.2.2	Derivation of the tunnel current . . . . .	22
2.2.3	Components of the tunnel current . . . . .	24
2.3	Transmission electron microscopy . . . . .	28
2.3.1	Selected Area Electron Diffraction Mode . . . . .	29
2.3.2	Algorithm for the identification of peak positions in SAED images . . . . .	33
2.4	Scanning near-field optical microscopy . . . . .	34
2.5	Stress and strain . . . . .	36
2.6	Polarization . . . . .	39
2.7	Concepts of roughness analysis . . . . .	40
2.7.1	Power-Spectral Density . . . . .	40
2.7.2	Auto-Covariance and Auto-Correlation Function . . . . .	42
2.7.3	Cross-Covariance and Cross-Correlation Function . . . . .	43
<b>3</b>	<b>Experimental details</b>	<b>45</b>
3.1	Cross-sectional scanning tunneling microscopy . . . . .	45
3.1.1	Sample preparation and cleavage . . . . .	45

3.1.2	Tip preparation . . . . .	46
3.2	Cross-sectional atom force microscopy and scanning near-field optical microscopy . . . . .	47
3.3	Cross-sectional scanning transmission electron microscopy . . . . .	48
3.4	Sample specifications . . . . .	48
3.4.1	A2314 . . . . .	48
3.4.2	A2688 . . . . .	49
3.4.3	A3162 . . . . .	49
<b>4</b>	<b>Electronic properties of the <math>\text{Al}_{1-x}\text{In}_x\text{N}(10\bar{1}0)</math> surface</b>	<b>51</b>
4.1	Experimental results . . . . .	51
4.2	DFT calculations of the $\text{Al}_{1-x}\text{In}_x\text{N}(10\bar{1}0)$ surface . . . . .	54
4.3	Analysis of tunnel spectra obtained on the $\text{Al}_{1-x}\text{In}_x\text{N}(10\bar{1}0)$ surface	56
4.4	Conclusion . . . . .	58
<b>5</b>	<b>About the electron affinity</b>	<b>59</b>
5.1	Definition of the electron affinity . . . . .	60
5.2	Electron affinity of GaN . . . . .	61
5.3	Electron affinity of AlN . . . . .	63
5.4	Electron affinity of InN . . . . .	63
5.5	Discussion . . . . .	65
5.6	Influence of the electron affinity on the tunnel current . . . . .	66
5.7	Estimation of the electron affinity of $\text{Al}_{0.81}\text{In}_{0.19}\text{N}$ using STS . . . . .	69
5.8	Conclusion . . . . .	70
<b>6</b>	<b>Strain and compositional fluctuations in <math>\text{Al}_{0.81}\text{In}_{0.19}\text{N}/\text{GaN}</math> heterostruc- tures</b>	<b>71</b>
6.1	Investigation of $\text{Al}_{0.81}\text{In}_{0.19}\text{N}$ layers by STM . . . . .	72
6.1.1	Cleavage surfaces of $\text{GaN}/\text{Al}_{0.81}\text{In}_{0.19}\text{N}$ heterostructures . . . . .	72
6.1.2	Height profiles of $\text{GaN}/\text{Al}_{0.81}\text{In}_{0.19}\text{N}$ heterostructures . . . . .	72
6.1.3	Roughness analysis . . . . .	75
6.2	Investigation of $\text{Al}_{0.81}\text{In}_{0.19}\text{N}$ by STEM and SAED . . . . .	80
6.3	Discussion . . . . .	84
6.3.1	Stress relaxation at the surface . . . . .	84
6.3.2	Strain induced piezoelectric polarization . . . . .	89

---

6.3.3	Changes of the tunnel current due to compositional fluctuations	91
6.3.4	Dislocations . . . . .	93
6.4	Conclusion . . . . .	94
<b>7</b>	<b>Defects in <math>\text{Al}_{1-x}\text{In}_x\text{N}</math></b>	<b>97</b>
7.1	Experimental results . . . . .	97
7.2	Discussion . . . . .	100
7.3	Conclusion . . . . .	102
<b>8</b>	<b>Contrast between GaN- and <math>\text{Al}_{x-1}\text{In}_x\text{N}</math>-layers</b>	<b>103</b>
8.1	Experimental results . . . . .	103
8.2	Discussion . . . . .	107
8.3	Conclusion . . . . .	109
<b>9</b>	<b>Summary</b>	<b>111</b>
	<b>Material parameters</b>	<b>115</b>
	<b>Bibliography</b>	<b>117</b>
	<b>List of own publications</b>	<b>137</b>

---

# Chapter 1

## Introduction

The idea of "materials of semiconducting nature" was first mentioned by Volta in 1782.[1, 2] However, the term "semiconductor" in today's sense was introduced much later by Weiss in 1910.[1, 3] The first to describe a semiconductor effect was Faraday in 1833. He realized that, contrary to metals, the conductivity of silver sulfide increases with temperature.[1, 4] This was corroborated by Hittorf in 1851.[1, 5] However it took nearly 100 years until this phenomenon could be described theoretically by Wilson, who developed the model of filled and empty energy bands to explain the difference between metals, insulators, and semiconductors in 1931.[1, 6, 7]

Since then the semiconductor technology developed rapidly. The theoretical basis to explain the rectifying effect of semiconductors, discovered by Braun in 1874, was given by Schottky and Mott in 1939. They developed a model for the presence of a potential barrier in a metal-semiconductor junction.[8, 9] In 1938 Hilsch and Pohl were the first to show that electronic signals can be amplified and switched with a three-electrode crystal,[10] followed by the implementation of the first bipolar transistor in 1947 by Bardeen and Brattain, and the first commercially available silicon devices in 1954.[8, 9] In 1958 the first integrated circuit as well as the first tunneling diode was presented.[9, 11] The first semiconductor lasers were developed around 1962.[9]

Today semiconductors find application in various electronic and optoelectronic devices, for example in light-emitting diodes (LEDs), bipolar transistors, high-electron

mobility transistors (HEMTs), and solar cells.[12] Significant progress was achieved with the use of GaN.[13] Due to its wide band gap, GaN permits the production of lasers and LEDs in the blue to ultraviolet wavelength range.[13, 14]

However, for several applications including distributed Bragg reflectors (DBRs), a second semiconductor combined in heterostructures with GaN is needed. The requirements for this second semiconductor are a close proximity of the lattice constants and concurrently a substantial refractive index contrast to GaN.[12] For this purpose, over the past decade especially ternary nitride semiconductor alloys attracted significant attention. For example in  $\text{Al}_x\text{Ga}_{1-x}\text{N}$  a refractive index contrast to GaN can be achieved with a high Al content, only. However, in that case a lattice mismatch between GaN and  $\text{Al}_x\text{Ga}_{1-x}\text{N}$  is inevitable, leading to tensile strain.[15, 16] Consequently dislocations and cracks are generated, regardless of whether GaN or AlN is used as buffer material.[15, 17–19] These defects negatively affect the implementation of optoelectronic devices and are only containable by elaborate stress engineering.[18, 20]

In contrast to  $\text{Al}_x\text{Ga}_{1-x}\text{N}$  and  $\text{In}_x\text{Ga}_{1-x}\text{N}$ ,  $\text{Al}_{1-x}\text{In}_x\text{N}$  can be grown nearly lattice-matched (LM) to GaN.[15, 21] According to Vegard's law, at room temperature lattice matched-conditions of  $\text{Al}_{1-x}\text{In}_x\text{N}$  to fully relaxed GaN are achieved at an In content of  $\sim 17.5\%$ .[16, 22] Concurrently at that In content,  $\text{Al}_{1-x}\text{In}_x\text{N}$  exhibits a substantial refractive index contrast to GaN.[15, 21] Thus, the formation of dislocations and cracks, and their critical effects on device properties may be avoided.[15] LM  $\text{Al}_{1-x}\text{In}_x\text{N}/\text{GaN}$  multilayers, assembled to high reflectivity DBRs, are used to implement resonant-cavity LEDs, optically pumped polariton lasers, and serve as optical cavities in vertical cavity surface emitting lasers (VCSELs).[15, 17–19, 21, 23–33] Furthermore applications of GaN/ $\text{Al}_{1-x}\text{In}_x\text{N}$  heterostructures in HEMTs are considered.[34–36] In these transistors, the commonly used  $p$ - $n$  homojunction is replaced by a heterojunction consisting of two semiconductors with different band gaps. This requirement is met by  $\text{Al}_{1-x}\text{In}_x\text{N}$  as well, since the band gaps of GaN and LM  $\text{Al}_{0.82}\text{In}_{0.18}\text{N}$  at room temperature amount to approximately 3.4 eV and 4.4 eV, respectively.[23, 37] Recently even the growth of  $p$ -type  $\text{Al}_{1-x}\text{In}_x\text{N}$  layers lattice-matched to GaN was achieved.[38] All of these properties make  $\text{Al}_{1-x}\text{In}_x\text{N}$  especially attractive for applications in electronic and optoelectronic devices.

---

The quality of  $\text{Al}_{1-x}\text{In}_x\text{N}$  materials depends, however, sensitively on strain and compositional fluctuations. For example, tensile strain occurring at  $\text{GaN}/\text{Al}_{1-x}\text{In}_x\text{N}$  interfaces was attributed to In surface segregation, causing the formation of dislocations.[19] Also the large Stokes shifts of up to 1 eV measured on  $\text{Al}_{1-x}\text{In}_x\text{N}$  were attributed to fluctuations of the In content.[15,39–42] Even small In fluctuations affect the local band gap, photoluminescence, carrier scattering, and spontaneous polarization, hence changing the properties of quantum heterostructures or HEMTs.[15,41–43] For layers thicker than the critical thickness for the formation of V-shaped defects, compositional fluctuations were found in connection with threading dislocations and V-shaped defects.[44–48] It is therefore of high importance to identify and control strain and In composition fluctuations in  $\text{Al}_{1-x}\text{In}_x\text{N}$ .

Furthermore, thus far mostly polar  $c$ -plane grown  $\text{Al}_{1-x}\text{In}_x\text{N}$  layers were investigated, but recently growth along non-polar directions has attracted significant interest [49–52] due to the absence of out-of-plane electric fields caused by piezoelectricity and spontaneous polarization mismatch.[53] It is known that the presence of surface states and the Fermi level position at the growth surface critically affect atomic processes during growth, such as the incorporation of dopants and impurities.[54,55] Hence, in order to achieve controlled growth conditions along non-polar directions, an accurate knowledge of the electronic structure of  $\text{Al}_{1-x}\text{In}_x\text{N}$  non-polar surfaces is necessary.

Therefore, in this thesis different LM  $\text{Al}_{1-x}\text{In}_x\text{N}/\text{GaN}$  heterostructures with layer thicknesses below the critical thickness for the development of V-shaped defects [48] are investigated by cross-sectional scanning tunneling microscopy and spectroscopy, force and near-field optical microscopy, and transmission electron microscopy. The aim is to identify strain and compositional fluctuations. In addition the presence of defects and their influence are investigated. Moreover, the electronic properties of  $\text{Al}_{1-x}\text{In}_x\text{N}(10\bar{1}0)$  surfaces are studied with the focus on surface states. A pinning of the Fermi level is investigated and the electron affinity is discussed in detail.

The thesis is structured as follows: In Chaps. 2 and 3 an overview of the theoretical and experimental concepts, which form the basis of the analyses and measurements presented in this thesis, is given. Investigations of the energetic position of the cation derived surface state on  $\text{Al}_{1-x}\text{In}_x\text{N}(10\bar{1}0)$  surfaces by cross-sectional

scanning tunneling spectroscopy in combination with density functional theory calculations are presented in Chap. 4. In addition, a polarity dependent Fermi-level pinning by the surface state is identified. The fitting of simulated to experimentally obtained tunnel spectra suggests an unexpectedly large electron affinity, which is discussed in Chap. 5. Strain and compositional fluctuations of nearly lattice-matched  $\text{Al}_{0.81}\text{In}_{0.19}\text{N}/\text{GaN}$  heterostructures are investigated in Chap. 6. Cross-sectional scanning tunneling microscopy images of the  $(10\bar{1}0)$  cleavage surface reveal height modulations in the vicinity of the  $\text{Al}_{0.81}\text{In}_{0.19}\text{N}$  layers. Selected area electron diffraction patterns show spatial fluctuations of the  $c$  and  $a$  lattice constants. The height modulations at the cleavage surface and the local changes of the lattice constants are assigned to alternating compressive and tensile strained domains, arising from compositional fluctuations. The strain additionally gives rise to steps in the  $\text{Al}_{1-x}\text{In}_x\text{N}/\text{GaN}$  layers on the  $(10\bar{1}0)$  cleavage surface, which are investigated in Chap. 7. In Chap. 8 it is deduced that strain and dislocations at the interfaces lead to height differences between  $\text{Al}_{1-x}\text{In}_x\text{N}$  and GaN on the cleavage surface. In Chap. 9 a summary is provided.

# Chapter 2

## Theoretical background

### 2.1 Scanning tunneling microscopy

The scanning tunneling microscope (STM) invented by Binnig and Rohrer [56–58] consists of a metal tip, which is brought close to the surface of a semiconducting or metallic sample. A voltage is applied between them, enabling electrons to overcome the vacuum barrier between tip and sample by tunneling.[59] Thus, a tunnel current flows that depends exponentially on the tip-sample separation. By scanning the tip over the sample this exponential dependence allows to obtain an image of the sample's surface. Hence, the STM allows direct real space access to the electronic and geometric properties of a surface, enabling for instance the investigation of isolated steps, defects, and impurities.[59]

#### 2.1.1 One dimensional tunneling effect

To begin with, the tunneling effect in the one dimensional case is recalled here.[60] The vacuum gap between the metal tip and the semiconductor sample can be described as a rectangular potential barrier of height  $V_0$  localized spatially between  $-a$  and  $+a$ :

$$V(x) = \begin{cases} V_0, & |x| < a \\ 0, & \text{otherwise.} \end{cases} \quad (2.1)$$

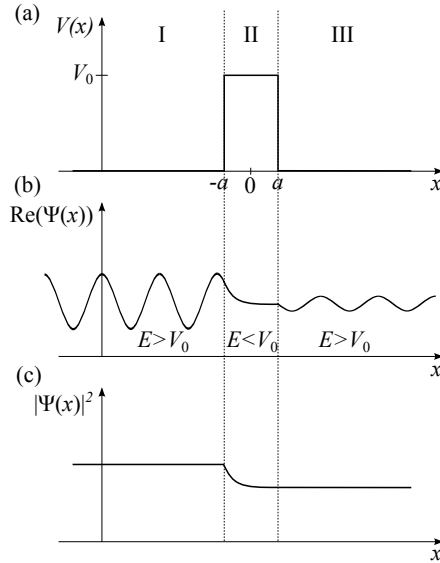


**Figure 2.1:** One-dimensional tunneling effect for an electron traveling from  $x = -\infty$  in  $+x$  direction. (a) Rectangular potential barrier of height  $V_0$ . (b) Real part of an incoming plane wave whose energy is lower than the potential barrier height ( $E < V_0$ ). In quantum mechanics the wave can enter the classically forbidden area with an exponentially decaying probability density function  $|\Psi(x)|^2$  (c). Hence for sufficiently narrow barriers the wave exhibits a non-zero probability density behind the potential barrier.

An electron approaching the barrier can be described by a plane wave with energy  $E$ . If the kinetic energy of the electron is lower than the potential barrier height  $0 < E < V_0$ , in classical mechanics the wave would be reflected at the barrier completely. In quantum mechanics, however, the wave can enter the classically forbidden area with an exponentially decaying probability density function  $|\Psi(x)|^2$ . Hence for sufficiently narrow barriers the wave exhibits a non-zero probability density behind the potential barrier, which the electron can thus overcome (cf. Fig. 2.1).

In order to solve the time independent one-dimensional Schrödinger equation presented in Eq. 2.2 [61]

$$H\Psi(x) = E\Psi(x), \quad H = -\frac{\hbar^2}{2m}\partial_x^2 + V(x), \quad (2.2)$$

where  $H$  is the Hamiltonian,  $E$  the electrons's energy (i.e. the eigenvalues),  $\Psi(x)$  the wave function (i.e. the eigenfunction),  $m$  the electron mass, and  $\hbar$  the reduced Plank constant, the three areas in Fig. 2.1 labeled I, II, and III are evaluated separately. Let  $e^{ikx}$  be a plane wave with wave vector  $k$  and normalized amplitude propagating from  $x = -\infty$  towards  $x = +\infty$ . When the wave encounters the potential barrier in area I it is partly reflected ( $Ae^{-ikx}$ ). The remaining part of the wave,  $B_+e^{ik'x}$ , enters area II and again is partially reflected at the right side of the barrier ( $B_-e^{-ik'x}$ ). The part of the wave  $Ce^{ikx}$ , which passes into area III, continues with reduced amplitude in  $+\infty$  direction. The wave functions in the three areas consist of the superposition of incoming and reflected wave, respectively [60]

$$\begin{aligned}\Psi_{\text{I}}(x) &= e^{ikx} + Ae^{-ikx}, \\ \Psi_{\text{II}}(x) &= B_+e^{ik'x} + B_-e^{-ik'x}, \\ \Psi_{\text{III}}(x) &= Ce^{ikx},\end{aligned}\tag{2.3}$$

with wave vectors

$$k^2 = \frac{2m}{\hbar^2}(E - V(x)).\tag{2.4}$$

In areas I and III the potential  $V(x)$  is zero, simplifying Eq. 2.4 to

$$k = \sqrt{\frac{2m}{\hbar^2}E}, \quad |x| > a.\tag{2.5}$$

In area II, the region of the potential barrier,  $V(x)$  exhibits the value  $V_0$ . Since in this area  $E < V_0$  applies according to definition,  $k'$  becomes complex (cf. Eq. 2.6). Thus, the wave function within the barrier region becomes real and shows an exponential decay.

$$k' = \sqrt{\frac{2m}{\hbar^2}(V_0 - E)} = \sqrt{\frac{2m}{\hbar^2}(E - V_0)} = i\kappa, \quad |x| < a.\tag{2.6}$$

As the current has to be conserved overall, the wave function and its derivation has to be continuous. Therefore four continuity conditions can be established at the walls of the barrier  $x = -a$  and  $x = +a$  from which the amplitudes  $A$ ,  $B_+$ ,  $B_-$ , and  $C$  are determined.  $|A|^2$  is identified as the reflection coefficient  $R$ , while  $|C|^2$

is equal to the transmittance  $T$ : [61]

$$T = |C|^2 = \frac{4E(V_0 - E)}{4E(V_0 - E) + V_0^2 \sinh^2(2a\kappa)}. \quad (2.7)$$

Thus, in contrast to the classical prediction, indeed the wave exhibits a non-zero probability to transmit through the potential barrier. Hence, the electron tunnels through the barrier. For  $\kappa a \gg 1$  it can be deduced that the tunneling probability decreases exponentially with the width  $2a$  of the potential barrier and with the square-root of the effective potential barrier  $V_0 - E$ . [61]

Transferred to the tunneling microscope, area I represents the metallic probe tip while area III can be associated with the (metallic) sample. In order to achieve a more realistic treatment, in the following many electrons are considered instead of one.

## 2.1.2 Tunnel current

In 1961 Bardeen described tunneling in a metal-insulator-metal tunneling junction of a many particle system using time-dependent first-order perturbation theory. [62] The application to the scanning tunneling microscope followed by Tersoff and Hamann in 1983. [59, 63] They treated the surface exactly while modeling the electronic wave-functions of the probe tip as a spherical  $s$ -orbital state. For low temperatures and biases the tunnel current was found to be proportional to the local density of states of the semiconductor surface, only.

Bardeen [62] defined separate potentials for the tip ( $V_t(\mathbf{r})$ ) and the sample ( $V_s(\mathbf{r})$ ), which drop smoothly to zero in the respective other region. Since he neglected electron-electron interaction, single-electron Hamiltonians (cf. Eq. 2.2) can be defined for tip and sample individually. The associated eigenfunctions  $\psi_t(\mathbf{r})$  and  $\psi_s(\mathbf{r})$  are called tip states and sample states, respectively. Then the tunnel current consists of the transfer of electrons from tip into sample states and vice versa. Further, it is assumed that the occupation probabilities of tip and sample are constant and independent of each other. It is supposed that tip and sample are in thermal equilibrium, respectively. [64] Thus, occupation probabilities of the tip and sample are

described by Fermi-Dirac statistics

$$f(E) = \frac{1}{\exp((E - E_F)/k_B T) + 1}, \quad (2.8)$$

with temperature  $T$ , Fermi energy  $E_F$  and Boltzmann's constant  $k_B$ . The transition probability of an electron in the tip at energy level  $E_t$  tunneling into a state  $\psi_s$  in the sample with an energy  $E_s$  is characterized by Fermi's golden rule [65, 66]

$$\Gamma_{t \rightarrow s} = \frac{2\pi}{\hbar} |M_{ts}|^2 \rho, \quad (2.9)$$

where  $M_{ts}$  is the tunneling matrix element between  $\psi_t$  and  $\psi_s$  and  $\rho$  is the density of final states. The total transition rate is obtained by summing over all states. In order to obtain the tunnel current, the total transition rate is multiplied by the elementary charge  $e$ , yielding

$$I = \frac{2\pi e}{\hbar} \sum_{t,s} f(E_t) [1 - f(E_s + eV)] |M_{ts}|^2 \delta(E_t - E_s), \quad (2.10)$$

where  $V$  is the applied voltage. The  $\delta$ -function ensures the energy conservation. Bardeen showed that the tunneling matrix element can be described by [62]

$$M_{ts} = \frac{\hbar^2}{2m} \int d\vec{S} (\psi_t^* \vec{\nabla} \psi_s - \psi_s^* \vec{\nabla} \psi_t), \quad (2.11)$$

with the surface integral lying entirely inside the vacuum region between tip and sample.

Tersoff and Hamann applied this formalism to scanning tunneling microscopy.[59, 63] In the limit of low temperatures and voltages the tunnel current (Eq. 2.10) can be rewritten to

$$I = \frac{2\pi}{\hbar} e^2 V \sum_{t,s} |M_{ts}|^2 \delta(E_s - E_F) \delta(E_t - E_F). \quad (2.12)$$

Then, in order to calculate  $M_{ts}$ , Tersoff and Hamann approximated the tip and surface wave functions,  $\psi_t$  and  $\psi_s$ . The surface wave function is evaluated by a

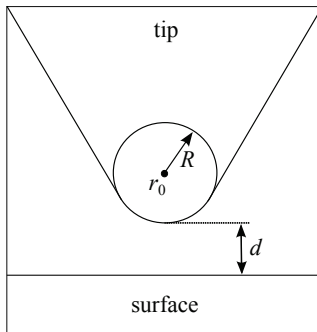


**Figure 2.2:** Tersoff and Hamann approximated the tip as a spherical state.  $d$  symbolizes the shortest distance between tip and surface, while  $R$  denotes the radius of the spherical approximation of the tip and  $r_0$  its center of curvature. The image is adapted from Ref.[63]

Fourier series expansion

$$\psi_s = \Omega_s^{-1/2} \sum_{\mathbf{G}} a_{\mathbf{G}} \cdot \exp[(\kappa^2 + |\vec{\kappa}_{\mathbf{G}}|^2)^{1/2} z] \cdot \exp(i\vec{\kappa}_{\mathbf{G}}\vec{x}), \quad (2.13)$$

with  $\Omega_s$  being the sample volume.  $\kappa = \hbar^{-1}(2m\Phi)^{1/2}$  is the inverse decay length of the wave functions into the vacuum, with  $\Phi$  being the work function.  $\vec{\kappa}_{\mathbf{G}}$  is defined as  $\vec{k}_{\parallel} + \vec{G}$ , where  $\vec{k}_{\parallel}$  is the surface Bloch wave vector of the surface state, and  $\vec{G}$  is a surface reciprocal-lattice vector.[59] The tip apex can be approximated as a sphere with radius  $R$  and center  $\vec{r}_0$  as shown in Fig. 2.2.  $d$  symbolizes the shortest distance between tip and surface. Based on this assumption the wave functions of the tip are approximated by

$$\psi_t = \Omega_t^{-1/2} c_t \kappa R e^{\kappa R} (\kappa |\vec{r} - \vec{r}_0|)^{-1} e^{-\kappa |\vec{r} - \vec{r}_0|}, \quad (2.14)$$

with  $\Omega_t$  being the tip's volume. By expanding the tip wave function in analogy to the surface wave function and assuming that the work functions  $\Phi$  of tip and sample are equal, the tunneling matrix element is derived to

$$M_{ts} = \frac{\hbar^2}{2m} 4\pi \kappa^{-1} \Omega_t^{-1/2} \kappa R \cdot \exp(\kappa R) \psi_s(\vec{r}_0). \quad (2.15)$$

Substituting the matrix element into Eq. 2.12 yields the tunnel current

$$I = 32\pi^3\hbar^{-1}e^2V\Phi^2D_t(E_F)R^2\kappa^{-4} \cdot \exp(2\kappa R) \sum_s |\psi_s(\vec{r}_0)|^2 \delta(E_s - E_F), \quad (2.16)$$

where  $D_t$  denotes the density of states per unit volume of the tip. The summation over the surface states expresses the local density of states (LDOS) per unit volume of the sample's surface at  $E_F$ ,  $\rho(\vec{r}_0, E_F)$ . The tunnel current is thus proportional to the applied voltage and the LDOS of the sample's surface at the position of the tip

$$I \propto V\rho(\vec{r}_0, E_F). \quad (2.17)$$

Consequently an STM image is mainly determined by the behavior of  $\rho(\vec{r}_0, E_F)$  without influence of the tip. By only taking the distance  $d$  between tip and sample in normal direction  $z$  into account, the local density of states near the Fermi energy can be expressed as

$$\rho(\vec{r}_0, E_F) = \rho(x, y, z, E_F) = \rho(x, y, z = 0, E_F) \cdot e^{-2\kappa d}, \quad (2.18)$$

with  $\kappa$  being the inverse decay length  $\kappa = \sqrt{\frac{2mB}{\hbar^2}}$ , where  $B$  is the barrier height. Thus, for low temperatures ( $T \approx 0$  K) and low voltages ( $V \ll \phi$ ), the tunnel current (cf. Eq. 2.17) can simply be expressed as

$$I = I_0 \cdot e^{-2\kappa d}. \quad (2.19)$$

### 2.1.3 WKB approximation of the tunnel current

For larger voltages and temperatures a simple planar tunneling model based on Wenzel-Kramers-Brillouin (WKB) approximation, can be applied.[67] In this model the matrix element is approximated by a transmission factor, which yields a tunnel current of

$$I = \int_0^{eV} \rho_s(r, E)\rho_t(r, E - eV)TdE, \quad (2.20)$$

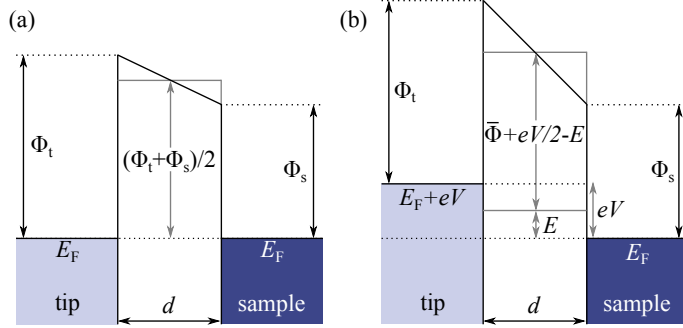


**Figure 2.3:** (a) Tunneling barrier if the work functions of tip  $\Phi_t$  and sample  $\Phi_s$  are different. (b) Tunneling barrier if additionally a tunnel voltage is applied between tip and sample. The image was modified from Ref.[68]

where  $T$  is the tunneling transmission probability [68]

$$T \propto \exp\left(-2d\sqrt{\frac{2m}{\hbar^2}\Phi}\right). \quad (2.21)$$

This equation applies for equal work functions of tip and sample  $\Phi$  and if no voltage between tip and sample is applied ( $V = 0$ ). However, in the majority of cases the work functions of tip,  $\Phi_t$ , and sample,  $\Phi_s$ , cannot be assumed to be equal. Without a tunnel voltage applied, tip and sample are in thermal equilibrium.[67] Hence, their Fermi levels align and the potential barrier, so far assumed to be rectangular, becomes trapezoidal, as shown in Fig. 2.3(a). Nevertheless, for simplicity the trapezoidal barrier also in this case is approximated as a rectangular barrier with average height  $\bar{\Phi} = (\Phi_t + \Phi_s)/2$ . If in addition a voltage is applied between tip and sample, the energy level of the tip shifts upwards or downwards depending on the polarity of the applied voltage. If a positive voltage  $V$  is applied at the sample, the energy level of the tip shifts upward by  $eV$  as shown in Fig. 2.3(b). For a state at energy  $E$  the tunnel barrier height thus changes to  $\Phi = \bar{\Phi} + eV/2 - E$ , with  $0 < E < eV$ . Consequently, electrons located at an energy  $E = eV$  inside the tip, experience a reduced barrier height of  $\bar{\Phi} - eV/2$  and are thus more likely to tunnel from the tip into the sample. (Vice versa, if a negative voltage is applied between tip and sample, tip states are shifted downwards compared to the Fermi energy of the sample. Thus electrons from occupied states in the sample are enabled to

tunnel into empty tip states.) Overall, if these considerations for the effective barrier height are taken into account, the transmission (Eq. 2.21) results in [67, 68]

$$T(E, eV, r) \propto \exp\left(-\frac{2d\sqrt{2m}}{\hbar}\sqrt{\frac{\Phi_s + \Phi_t}{2} + \frac{|eV|}{2} - E}\right). \quad (2.22)$$

For lower electron energies  $E$ , the transmission probability thus decreases exponentially, due to the higher barrier these states experience. Additionally it should be noted, that in analogy to the interpretation of the one-dimensional tunneling effect, the transmission probability exponentially depends on the width of the tunnel barrier  $d$ , i.e. on the tip-sample separation.

## 2.2 Simulation of the tunnel current

Calculations of the tunnel current in this thesis are performed as described in Ref. [69]. A potential difference between tip and semiconductor induces a space charge region within the semiconductor. Depending on the polarity of the potential difference, an upward or downward band bending in the semiconductor is caused.[70] The expansion of the space charge region into the semiconductor and its magnitude depend on the physical properties of the semiconductor. For instance the doping concentration influences the screening of the potential at the surface. However, the band bending can be influenced by other factors such as intrinsic or extrinsic surface states.[70] Hence, in a first step the electrostatic potential and the charge carrier distributions are calculated by numerically solving the Poisson and continuity equations simultaneously. Second, the carrier concentration and the potential distribution along the central axis through the tip apex are used to derive the tunnel current in a one-dimensional parabolic band approximation.[71]

### 2.2.1 Derivation of the tip induced band bending

In order to obtain the electrostatic potential and the charge carrier distributions, three coupled partial differential equations, the Poisson equation and two continuity equations, are solved in three dimensions.[69] The Poisson equation for the

electrostatic potential  $\phi(x, y, z)$  at the position  $(x, y, z)$  is defined as

$$\Delta\phi(x, y, z) + \frac{e}{\varepsilon_0\varepsilon_r}[p(x, y, z) - n(x, y, z) + N_D^+ - N_A^-] = 0, \quad (2.23)$$

with the vacuum permittivity  $\varepsilon_0$  and the relative permittivity of the semiconductor  $\varepsilon_r$ .  $n(x, y, z)$  and  $p(x, y, z)$  describe the electron and hole concentration at the position  $(x, y, z)$ , respectively. The density of ionized donors  $N_D^+$  and acceptors  $N_A^-$  can be calculated by [72]

$$\begin{aligned} N_D^+ &= N_D\{1 + 2 \exp[(E_F - E_D)k_B T]\}^{-1}, \\ N_A^- &= N_A\{1 + 2 \exp[(E_A - E_F)k_B T]\}^{-1}, \end{aligned} \quad (2.24)$$

where,  $N_D$  and  $N_A$  are the donor and acceptor concentration and  $E_D$  and  $E_A$  denote the energy level of donors and acceptors, respectively. The continuity equations for electrons and holes are [73]

$$\begin{aligned} \nabla \cdot \vec{J}_n - eR &= 0, \\ \nabla \cdot \vec{J}_p + eR &= 0, \end{aligned} \quad (2.25)$$

with  $R$  being a time-averaged generation or recombination rate.  $\vec{J}_n$  and  $\vec{J}_p$  are the current densities for electrons and holes, respectively, each consisting of a drift and diffusion term

$$\begin{aligned} \vec{J}_n &= e[\mu_n n(x, y, z)\vec{E} + D_n \nabla n(x, y, z)], \\ \vec{J}_p &= e[\mu_p p(x, y, z)\vec{E} - D_p \nabla p(x, y, z)]. \end{aligned} \quad (2.26)$$

$\mu_n$  and  $\mu_p$  are the electron and hole mobilities and  $D_n$  and  $D_p$  are their diffusion coefficients. Mobilities and diffusion coefficients are connected by the Einstein relation  $D_{n(p)} = (k_B T/e)\mu_{n(p)}$ . With  $\vec{E} = -\nabla\phi$ , the continuity equations are transformed to

$$\begin{aligned} \nabla \cdot [D_n \nabla n(x, y, z) - \mu_n n(x, y, z) \nabla \phi] - R &= 0, \\ \nabla \cdot [D_p \nabla p(x, y, z) - \mu_p p(x, y, z) \nabla \phi] - R &= 0. \end{aligned} \quad (2.27)$$

Assuming thermal equilibrium, the net recombination rate  $R$  can be described by [74]

$$R(x, y, z) = B \cdot [n(x, y, z)p(x, y, z) - n_0p_0], \quad (2.28)$$

where  $n_0$  and  $p_0$  are the number of electrons and holes in thermal equilibrium, and  $B$  is the bimolecular recombination coefficient. For direct band gaps  $B$  can be approximated by [75, 76]

$$B = 3 \cdot 10^{-10} \left( \frac{300 \text{ K}}{T} \right)^{3/2} \left( \frac{E_g}{1.5 \text{ eV}} \right)^2 \cdot 10^{21} \frac{\text{nm}^3}{\text{s}}. \quad (2.29)$$

In order to solve the three coupled differential equations (Eq. 2.23 and Eq. 2.27), the differential operators are replaced by their respective difference operator, following Selberherr's discretization approach.[77] The resulting equations can be found in Ref. [69]. In order to account for the Pauli exclusion principle in quantum dots which may occur near the surface, additionally a quantum correction in the drift and diffusion model (Eqs. 2.26) is needed. Therefore a repulsive potential is added in the discretization of the continuity equation for electrons and holes.[78] At the borders of the simulated three-dimensional grid, Neumann boundary conditions are applied. At the semiconductor's surface the interface condition

$$\vec{n} \cdot (\vec{D}_{\text{vac}} - \vec{D}_{\text{semi}}) = \sigma \quad (2.30)$$

is applied, with  $\vec{n}$  being the normal vector of the surface and  $\vec{D} = -\varepsilon_0\varepsilon_r\nabla\phi$  the dielectric displacement density.  $\sigma$  refers to the surface charge density. Thus, at the semiconductor's surface the electrostatic potential is obtained by solving

$$\varepsilon_0\varepsilon_r \left. \frac{\partial\phi}{\partial z} \right|_{\text{semi}} - \varepsilon_0 \left. \frac{\partial\phi}{\partial z} \right|_{\text{vac}} - \sigma = 0. \quad (2.31)$$

The initial values for the electrostatic potential in the semiconductor and in the vacuum are set to zero, while the potential of the tip is set to a constant value  $\phi_{\text{tip}}$ . The electrostatic potential of the tip is defined relative to the semiconductor [70]

$$\phi_{\text{tip}} = V + (E_F - E_C - \chi + \Phi_t)/e, \quad (2.32)$$

where  $V$  is the voltage applied between tip and semiconductor,  $\chi$  the electron affinity of the semiconductor, and  $\Phi_t$  the work function of the tip. The part in parentheses is called the contact potential  $\Delta\phi$  and describes the work function difference between tip and sample.[70] The electron and hole concentrations in the parabolic band approximation [73]

$$\begin{aligned} n &= N_C \frac{2}{\pi} F_{1/2} \left( \frac{E_F - E_C}{k_B T} \right), \\ p &= N_V \frac{2}{\pi} F_{1/2} \left( \frac{E_V - E_F}{k_B T} \right), \end{aligned} \quad (2.33)$$

respectively, are used as initial values for the carrier densities.  $F_{1/2}$  is the Fermi-Dirac integral,  $E_F$  the Fermi energy,  $E_C$  the minimum of the conduction band and  $E_V$  the maximum of the valence band.  $N_C$  and  $N_V$  describe the effective density of states of the conduction and valence band, respectively.

$$\begin{aligned} N_C &= 2 \left( \frac{2\pi m_{\text{eff},C} k_B T}{h^2} \right)^{3/2}, \\ N_V &= 2 \left( \frac{2\pi m_{\text{eff},V} k_B T}{h^2} \right)^{3/2}, \end{aligned} \quad (2.34)$$

with  $m_{\text{eff},C}$  being the density of states effective mass for electrons,  $m_{\text{eff},V}$  the density of states effective mass for holes, and  $h$  being Planck's constant. The electron effective mass  $m_{\text{eff},C} = (m_1^* \cdot m_2^* \cdot m_3^*)^{1/3}$  is the product of the effective masses of the ellipsoidal energy surface along the principal axes, while the hole effective mass is calculated from the light and heavy hole masses  $m_{\text{eff},V} = (m_{lh}^{*3/2} + m_{hh}^{*3/2})^{2/3}$ . The concentration of electrons and holes mainly depends on the position of conduction and valence band edges relative to the Fermi energy.

## 2.2.2 Derivation of the tunnel current

The tunnel current is computed in a one-dimensional approach following Refs. [71, 79]. The total current  $I = A \cdot J$  is composed of the tunnel area  $A$  and the current density  $J = J_V + J_C$ , which is separated into a valence band and a conduction band

component given by [71]

$$\begin{aligned}
 J_V &= -\frac{m_e e}{2\pi^2 \hbar^3} \int_{E_{F,\text{tip}}}^{E_F} dE \Theta(E_V - E) \int_E^{E+\alpha(E_V-E)} dW D(W), \\
 J_C &= -\frac{m_e e}{2\pi^2 \hbar^3} \int_{E_{F,\text{tip}}}^{E_F} dE \Theta(E - E_C) \int_E^{E+\alpha'(E_C-E)} dW D(W)
 \end{aligned} \tag{2.35}$$

where  $\Theta(E)$  is the step function limiting the contributions to the integrals to energies below the valence band maximum and above the conduction band minimum, respectively.  $\alpha = m_{\text{eff},V}/m_e$  and  $\alpha' = m_{\text{eff},C}/m_e$  are the density-of-states effective masses for valence and conduction band divided by the electron mass, respectively.  $D(W)$  denotes the transmission coefficient at energy  $W = E - \frac{\hbar^2 k_{\parallel}^2}{2m}$  normal to the sample's surface in the WKB approximation.[79]

$$D(W) = \exp\left(-2\frac{\sqrt{2m_e}}{\hbar} \int_0^d [V(z) - W]^{1/2} dz\right) \tag{2.36}$$

Note, this definition of the transmission coefficient applies for any potential which changes sufficiently slow with the position. The integration over a constant potential would yield Eq. 2.22.

The vacuum barrier used for the derivation of  $D(W)$  is the sum of a term derived from the solution of the Poisson equation in the vacuum region and an image force term [71, 80]

$$V_{\text{img}}(z) = -1.15 \frac{e^2 \ln 2}{2 \cdot 8\pi\epsilon_0 d} \frac{d^2}{z(d-z)}. \tag{2.37}$$

This term reduces the vacuum barrier near the surface of the tip and the semiconductor in order to account for image charges.

In analogy, for the calculation of the transmission through the space charge region in the semiconductor near the surface, the term  $[V(z) - W]$  in Eq. 2.36 is replaced by  $[E_C - W]$ . [81]

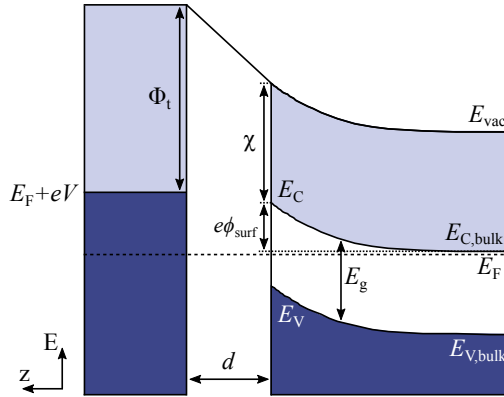


**Figure 2.4:** Band diagram of the tip (left) and the semiconductor (right) separated by the distance  $d$ . The band gap of the semiconductor is denoted  $E_g$ .  $E_V$  and  $E_C$  are the valence band maximum and conduction band minimum, respectively. A potential difference between tip and semiconductor induces a band bending near the surface of the semiconductor, shifting  $E_V$  and  $E_C$  upward compared to the bulk values  $E_{V,\text{bulk}}$  and  $E_{C,\text{bulk}}$ . The electrostatic potential at the surface of the semiconductor is denoted  $\phi_{\text{surf}}$ . The Fermi level of the semiconductor and the tip are labeled  $E_F$  and  $E_F + eV$ , respectively.  $\Phi_t$  is the work function of the tip and  $\chi$  the electron affinity of the semiconductor.

### 2.2.3 Components of the tunnel current

The tunnel current can be divided into ten components. Which case applies depends on the electrostatic potential at the surface of the semiconductor  $\phi_{\text{surf}}$ , on the Fermi level position  $E_F$  of the semiconductor, and on the Fermi level position of the tip  $E_F + eV$ , as shown in Fig. 2.4 for a positive surface potential.  $E_g$  denotes the band gap of the semiconductor.  $E_{V,\text{bulk}}$  and  $E_{C,\text{bulk}}$  are the valence and conduction band edges in the bulk, respectively.

First, tunneling into or out of the conduction band is discussed. All possible configurations are presented in Fig. 2.5, where occupied states are depicted in dark blue while empty states are shown in blue-gray. In Fig. 2.5(a)-(c) upward band bending is shown. If a positive voltage  $V$  is applied, electrons can tunnel out of occupied tip states into empty states in the conduction band of the semiconductor. Electrons in the tip with an energy  $E > (E_{C,\text{bulk}} + e\phi_{\text{surf}})$  can overcome the vacuum

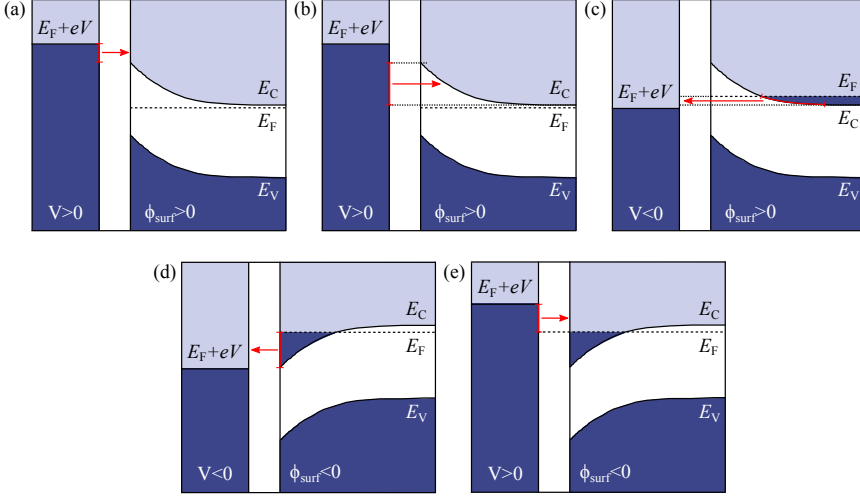


**Figure 2.5:** Different configurations of tunneling into or out of the conduction band with occupied states depicted in dark blue while empty states are shown in light gray. (a) For the case of an upward band bending and a positive voltage applied between tip and semiconductor, electrons in the tip with an energy  $E > (E_{C,\text{bulk}} + e\phi_{\text{surf}})$  can overcome the vacuum barrier and directly tunnel into the conduction band. (b) Electrons with an energy  $E_{C,\text{bulk}} < E < (E_{C,\text{bulk}} + e\phi_{\text{surf}})$  additionally have to cross the space charge region. (c) If a negative voltage is applied at upward band bending, a conduction band current occurs for degenerately doped semiconductors. (d) For a downward band bending, the conduction band is dragged below the Fermi level at the surface of the semiconductor which leads to an accumulation of electrons in the conduction band. At negative voltages these electrons can tunnel out of the accumulation zone into empty tip states. (e) At positive voltages electrons in the tip can tunnel into empty conduction band states of the semiconductor.

barrier and directly tunnel into the conduction band as shown in Fig. 2.5(a). In contrast electrons with an energy  $E_{C,\text{bulk}} < E < (E_{C,\text{bulk}} + e\phi_{\text{surf}})$  have to cross the space charge region in addition to the vacuum barrier (cf. Fig. 2.5(b)). For negative voltages ( $V < 0$ ) upward band bending only leads to a conduction band current, if the semiconductor is degenerately doped (cf. Fig. 2.5(c)). In this case the Fermi level is situated within the conduction band. Thus, the conduction band in the bulk exhibits occupied states from which electrons can tunnel into empty tip states. Configurations of a downward band bending in the semiconductor are illustrated in Fig. 2.5(d) and (e). If the bands are bend down far enough, the conduction band is dragged below the Fermi level at the surface of the semiconductor. This leads to an accumulation of electrons in the conduction band of an  $n$ -type semiconductor. In  $p$ -type semiconductors this phenomenon is called inversion. If a negative voltage is applied between tip and sample (cf. Fig. 2.5(d)) electrons can tunnel out of the accumulation zone of the semiconductor into empty tip states. At positive voltages electrons in the tip can tunnel into empty conduction band states of the semiconductor (cf. Fig. 2.5(e)).

The valence band current can be divided into five analog components that are outlined in Fig. 2.6. In Fig. 2.6(a)-(c) downward band bending is illustrated. At negative voltages electrons occupying the valence band with energy  $E < (E_{V,\text{bulk}} + eV)$  can overcome the vacuum barrier and tunnel into empty tip states. This configuration is shown in Fig. 2.5(a). Electrons in the valence band exhibiting an energy  $(E_{V,\text{bulk}} + eV) > E > E_{V,\text{bulk}}$  additionally need to overcome the space charge region of the semiconductor (cf. Fig. 2.5(b)). If a positive voltage is applied at downward band bending, a valence band current only occurs if the Fermi level is below the valence band edge. As shown in Fig. 2.5(c), in this case empty states exist in the valence band, into which electrons can tunnel from the tip through the vacuum barrier and the space charge region. In Fig. 2.5(d) and (e) upward band bending is shown. If the valence band at the surface of the semiconductor is pushed above the Fermi level, a depletion of the valence band (i.e. an accumulation of holes at  $p$ -type surfaces, called inversion in  $n$ -type semiconductors) occurs. For  $V > 0$ , electrons can tunnel out of the tip into the hole accumulation zone (cf. Fig. 2.5(d)). At negative voltages, electrons with an energy  $(E_{\text{F}} + eV) < E < E_{\text{F}}$  can tunnel from occupied states in the valence band into empty tip states.

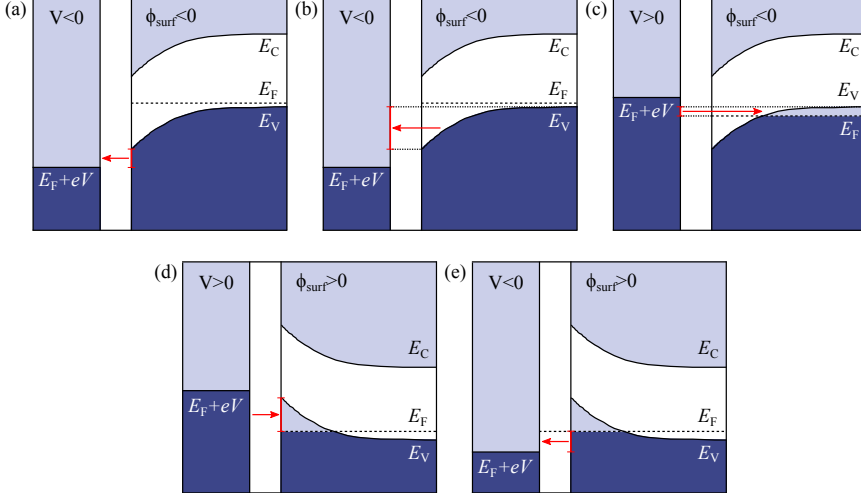


**Figure 2.6:** Different configurations of tunneling into or out of the valence band. (a) For a downward band bending and at negative voltages, electrons occupying the valence band with energy  $E < (E_{V, \text{bulk}} + eV)$  can overcome the vacuum barrier and tunnel into empty tip states. (b) Electrons in the valence band exhibiting an energy  $(E_{V, \text{bulk}} + eV) > E > E_{V, \text{bulk}}$  additionally need to overcome the space charge region of the semiconductor. (c) For  $V > 0$  valence band tunneling only occurs if the Fermi level is below the valence band edge  $E_F < E_{V, \text{bulk}}$ . In this case empty states exist in the valence band, into which electrons can tunnel from the tip through the vacuum barrier and the space charge region. (d) Upward band bending can lead to an accumulation of holes in the valence band at the surface of the semiconductor. For  $V > 0$  electrons can tunnel out of the tip into this hole accumulation zone. (e) For  $V < 0$  electrons with an energy  $(E_F + eV) < E < E_F$  can tunnel from occupied states in the valence band into empty tip states.

## 2.3 Transmission electron microscopy

The resolution of a microscope, regardless of whether it is a transmission electron microscope (TEM) or an optical microscope, depends on the wavelength  $\lambda$  of the incident beam.[82] The minimal distance  $d$  between two features that can still be distinguished in the image of a microscope is given by the Abbe diffraction limit [83]

$$d = \frac{\lambda}{n \sin \vartheta}, \quad (2.38)$$

where  $n$  is the refractive index and  $\vartheta$  the diffraction angle. Thus,  $d$  decreases linearly with decreasing wavelength. Hence, by replacing the photon sources of optical microscopes by electrons exhibiting a much smaller wavelength, the microscope's resolution improves significantly. The de Broglie wavelength of electrons with a correction for relativistic effects is given by [83]

$$\lambda = \frac{h}{\sqrt{2m_0 E_0 (1 + \frac{E_0}{2m_0 c^2})}}, \quad (2.39)$$

where  $h$  is Planck's constant,  $m_0$  the rest mass of electrons,  $c$  the speed of light, and  $E_0 = eV$  is the kinetic energy of an accelerated electron.

In a TEM the electron beam with electrons of wavelength  $\lambda$ , produced by the electron gun, is directed to the sample by the magnetic lenses. After transmission through the sample, the electron beam is projected onto a screen. The resulting image shows the interaction between the electron beam and the sample and thus contains information about the morphology, crystallography, and composition of the sample. The image contrast depends on the deflection of the primary electrons at the atomic nuclei, i.e. on the sample's thickness, on its density of atoms, on the atomic number, and on the energy of incident electrons. Assuming elastic interaction, the number  $N_E$  of electrons deflected after passing the sample with thickness  $s$  is given by [83]

$$N_E = N_{E,0} \cdot \exp\left(-\frac{s}{\Lambda_{\text{el}}}\right), \quad (2.40)$$

where  $N_{E,0}$  is the number of incident electrons and  $\Lambda_{\text{el}}$  is called the mean free path

of elastic scattering and can be approximated by [83]

$$\Lambda_{\text{el}} = \left( \frac{8\varepsilon_0 E_0}{Z \cdot e^2} \right)^2 \frac{\pi \tan^2 \frac{\alpha}{2}}{N_A \cdot \rho}. \quad (2.41)$$

$Z$  is the atomic number of the nucleus the electron interacts with,  $N_A$  Avogadro's constant,  $\rho$  the density of atoms within the sample, and  $\alpha$  the acceptance angle. The acceptance angle selects all electrons deflected into a narrow solid angle segment.

### 2.3.1 Selected Area Electron Diffraction Mode

For the *selected area electron diffraction mode* (SAED) of the transmission electron microscope the sample is illuminated by a defocused and therefore parallel electron beam.[82] After passing the sample and the objective lens, a selected area aperture limits the field of view of the beam.[83] Thereby the resulting diffraction pattern originates from a small selected area of the sample in the order of few nm, only.[83]

In the sample the incoming beam is partly reflected at the lattice planes. Reflected waves from different lattice planes interfere with each other [84] and constructive interference can be found according to Bragg's law at

$$n \cdot \lambda = 2d_{hkl} \cdot \sin \frac{\theta}{2}, \quad (2.42)$$

with  $d_{hkl}$  being the distance between two lattice planes and  $\frac{\theta}{2}$  the angle between the lattice plane and the incident wave.  $n$  is a positive integer that gives the order of diffraction.  $d_{hkl}$  can be determined from Eq. 2.42 if the wavelength and the angle of incidence are known. Additionally, the structure factor and thereby forbidden reflections have to be considered. In TEM measurements the diffraction angle  $\theta$  is given by

$$\theta = \frac{r}{L}, \quad (2.43)$$

with  $r$  being the radial distance from the central reflection within the diffraction pattern and  $L$  being the camera length, i.e. the distance between the sample and the detector. Due to the lenses in the TEM,  $L$  is the product of the magnification by the projective lenses and the focal length of the objective lens.[83] Usually  $\theta$

is not calculated, but rather calibrated by using the diffraction pattern of a well-known reference sample [83] such as gold. Because of spherical aberration, which increases with diffraction angle, measured values of  $r$  are systematically lower than theoretically expected values.[83]

In order to derive lattice constants of wurtzite structure crystals from SAED images, the theoretical determination of the lattice plane distances  $d_{hkl}$  is elucidated first. Theoretically the distances  $d_{hkl}$  between lattice planes for the primitive hexagonal crystal system can be obtained from the equation [83]

$$d_{hkl} = \frac{1}{\sqrt{\frac{4}{3a^2}(h^2 + hk + k^2) + \frac{l^2}{c^2}}}, \quad (2.44)$$

with  $a$  and  $c$  being the lattice constants of the hexagonal crystal system.  $h$ ,  $k$  and  $l$  are Miller's indices and depend on the orientation of the sample. For hexagonal crystal systems often Miller-Bravais indices instead of Miller indices are used for the description of lattice planes. The Miller-Bravais indices are denoted  $(hkil)$ , where  $i = -(h + k)$  is redundant.[85, 86] This four-fold labeling makes symmetrically equivalent lattice planes apparent, since they are generated by permutations of the first three indices.[87] For example equivalent  $m$ -planes are described by  $(10\bar{1}0)$ ,  $(01\bar{1}0)$  and  $(1\bar{1}00)$  in the hexagonal crystal. Note, the Miller-Bravais indices must not be confused with Weber symbols  $[qrst]$  that denote directions in four-fold indexing. Directions in four-fold  $[qrst]$  and three-fold  $[uvw]$  labeling can be converted into each other by using  $u\vec{a}_1 + v\vec{a}_2 + w\vec{c} = q\vec{a}_1 + r\vec{a}_2 + s\vec{a}_3 + t\vec{c}$  and inserting  $\vec{a}_3 = -(\vec{a}_1 + \vec{a}_2)$  and  $s = -(q + r)$ .[88]  $\vec{a}_1$ ,  $\vec{a}_2$  and  $\vec{c}$  are the lattice vectors that define the unit cell, as indicated in Fig.2.7(a). This yields the relations [83, 88]

$$q = \frac{1}{3}(2u - v), \quad r = \frac{1}{3}(2v - u), \quad s = -\frac{1}{3}(u + v), \quad t = w. \quad (2.45)$$

The advantage of using four-fold indices is that the directional vector  $[qrst]$  is perpendicular to the lattice plane  $(qrst)$ . Generally in the hexagonal crystal this does not apply for three-fold notation.[85, 87] Besides the directional vectors  $\vec{a}_1$ ,  $\vec{a}_2$ ,  $\vec{a}_3$ , and  $\vec{c}$ , two lattice planes are shown in Fig 2.7(a). An  $m$ -plane  $(10\bar{1}0)$  is illustrated in light blue and an  $a$ -plane  $(\bar{2}110)$  is colored in purple. The unit cell is highlighted by thick black lines.

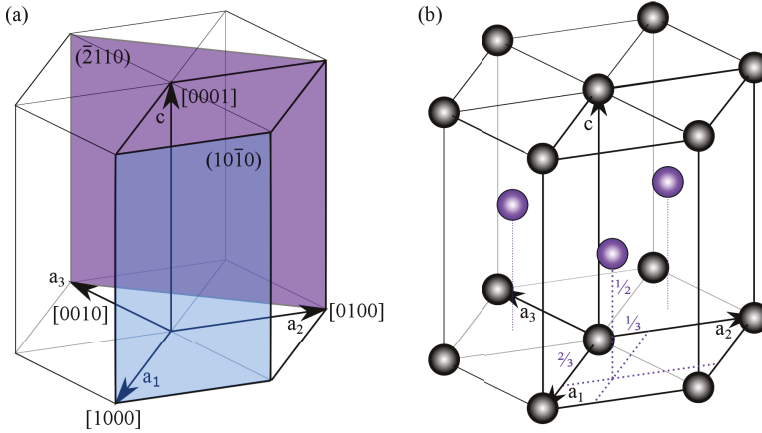


**Figure 2.7:** Hexagonal crystal system. (a) The limits of the primitive hexagonal unit cell are marked by thick black lines. The directions are given as four-fold indexes. Two lattice planes, an  $m$ -plane  $(10\bar{1}0)$  and an  $a$ -plane  $(\bar{2}110)$  are highlighted. (b) Positions of atoms in the hexagonal closed packed (hcp) structure. Compared to the primitive hexagonal structure (black spheres) one atom per unit cell is added at the position  $(2/3, 1/3, 1/2)$  (purple spheres) in the hcp structure.

Materials like GaN and  $\text{Al}_{1-x}\text{In}_x\text{N}$  crystallize in the *hexagonal close packed* (hcp) structure shown in Fig 2.7(b). Compared to the primitive hexagonal cell, the hcp unit cell contains an additional atom at the position  $(2/3, 1/3, 1/2)$ . In Fig 2.7(b) atoms of the primitive hexagonal structure are depicted as black spheres while the additional atoms of the hcp structure are colored in purple. The additional atoms in the closed packed structure change the interplanar spacing. Hence, a correction factor  $P_{hkl}$ , that includes the position of the additional atom in the unit cell, has to be considered for the calculation of the lattice-plane distances. This yields for the lattice-plane distance  $d'_{hkl}$  of the hcp structure [83, 89]

$$d'_{hkl} = d_{hkl} \cdot P_{hkl}, \quad P_{hkl} = \frac{2}{3}h + \frac{1}{3}k + \frac{1}{2}l. \quad (2.46)$$

Thus, the smallest lattice-plane distance in  $\bar{c}$  direction changes to  $d'_{001} = 1/2 \cdot d_{001} = 1/2 \cdot c$ , while the distance between nearest  $a$  planes  $d'_{110} = 1 \cdot d_{110} = 1/2 \cdot a$  does not change. The corrected distance between  $m$ -planes yields  $d'_{100} = 2/3 \cdot d_{100}$  and  $d'_{010} = 1/3 \cdot d_{010}$ , with  $d_{100}$  and  $d_{010}$  being  $\sqrt{3}/2 \cdot a$ .

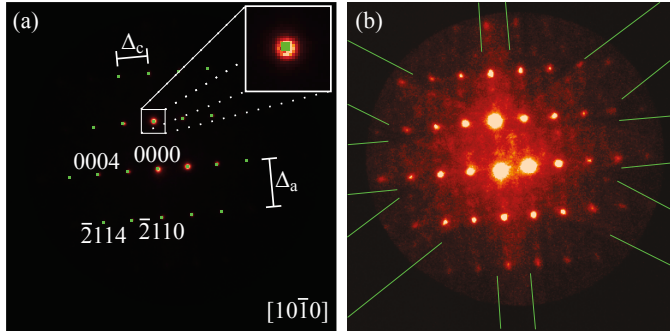


**Figure 2.8:** (a) TEM diffraction pattern of  $\text{Al}_{0.81}\text{In}_{0.19}\text{N}$ , along the  $[10\bar{1}0]$  ( $[210]$ ) zone axis, indexed according to Ref. [87]. The inset shows a magnification of the diffraction spot framed by the white square. The green squares symbolize the geometric centre of the detected diffraction points. (b) Same diffraction pattern with enhanced contrast. Kikuchi lines and weak additional diffraction spots appear. The Kikuchi lines are marked by the green lines. Their symmetry centre does not completely coincide with the central diffraction peak (0000).

Returning to the determination of lattice constants from SAED, an example of a diffraction pattern of a wurtzite structure  $\text{Al}_{1-x}\text{In}_x\text{N}$  sample is shown in Fig 2.8(a). The diffraction pattern was measured along the  $[10\bar{1}0]$  zone axis, revealing diffraction spots of  $c$ - and  $a$ -planes. Due to the selection rules of the hcp structure, the reflections where  $l$  is odd and  $h + 2k$  is a multiple of three, are missing.[87] Note, because of the negligible atomic scattering amplitude of nitrogen, the rules for the hcp structure can be applied.[90,91] The same diagram with an enhanced contrast is shown in Fig 2.8(b). First, weak Kikuchi lines (marked by green lines) are visible,[92] which arise from multiple, and thus incoherently scattered electrons.[87] The Kikuchi lines match the lines presented in Ref. [93] and Ref. [94]. Since the symmetry center of the Kikuchi lines does not completely coincide with the central diffraction peak (0000), it can be assumed that the sample was slightly tilted against the intended zone axis.[83, 87] A tilting leads to sets of weak diffraction spots shifted relative to the primary diffraction spots in Fig 2.8(b). The additional diffraction spots become visible if the Bragg condition is nearly fulfilled by a second set of lattice planes.[83] From such diffraction patterns the lattice constants  $c$  and  $a$  can be determined by measuring the distance between adjacent major spots in  $\langle 0001 \rangle$  and  $\langle \bar{2}110 \rangle$  reciprocal directions. Then, according to Eq. 2.46,  $c^{-1}$  equals

$2 \cdot \Delta_c$  while  $a^{-1}$  is given by  $2 \cdot \Delta_a$  (cf. Fig 2.8(a)).

### 2.3.2 Algorithm for the identification of peak positions in SAED images

In order to determine the distance between adjacent spots in diffraction patterns, the center of each diffraction spot has to be identified. To begin with, the diffraction pattern or image  $f(x, y)$  is smoothed by computing the convolution of the image with a Gaussian kernel  $g(x, y; t)$  to reduce the image noise.

$$\begin{aligned} L(x, y; t) &= g(x, y; t) * f(x, y) \\ &= \sum_{m=-M}^M \sum_{n=-N}^N g(m, n; t) f(x - m, y - n) \quad (t > 0), \\ g(m, n; t) &= \frac{1}{2\pi t^2} \exp\left(-\frac{m^2 + n^2}{2t^2}\right), \end{aligned} \quad (2.47)$$

with  $M$  and  $N$  being the width and the height of the image in pixel (px).  $t$  is the width of the Gaussian distribution. For the later analysis  $t = 8$  px was chosen, which is much smaller than the spot size and hence ensures, that the shape and in particular the center of the spots remains rather unchanged, while spikes are removed.

In a second step, the background caused by inelastic scattering, has to be subtracted.[83] Figure 2.8(b) illustrates the distribution of the background in the image. In the center the background is much higher than closer to the edges and even higher than the diffraction peaks at the edge of the pattern. Therefore the subtraction of a constant background would remove most of the diffraction spots as well. Instead a spatially modulated background  $\mu(x, y)$  has to be calculated for each pixel  $(x, y)$ .  $\mu(x, y)$  is derived in analogy to Eq. 2.47, but with a broader Gaussian kernel ( $t = 20$  px) and an area of  $40 \times 40$  pixels. The broader Gaussian kernel and the large area reduce the impact of diffraction peaks on the background determination. Afterwards a root-mean square of the background subtracted diffraction pattern

for the whole image is calculated by

$$\sigma_{\mu} = \sqrt{\frac{1}{M \cdot N} \sum_{x=1}^M \sum_{y=1}^N (L(x, y) - \mu(x, y))^2}. \quad (2.48)$$

All background subtracted image points  $L(x, y) - \mu(x, y)$  whose values are below  $\sigma_{\mu}$  are considered as noise.

From the remaining pixels of  $L(x, y)$  the diffraction points are isolated according to the rules of blob detection.[95] In the case of SAED images for simplicity a blob can be defined as an area that is significantly brighter than its neighborhood. First of all, the image is scanned for local maxima, defined as those pixels  $(x, y)$  where the  $z$  value of all eight adjacent pixels is lower. These local maxima are the seeds of a blob each. Then all other pixels are assigned to the blobs by the following three rules: (1) If a pixel has one or more higher neighbors that all belong to the same blob, the pixel also is part of that blob. (2) If the pixel has more than one higher neighbor and those neighbors belong to different blobs, the pixel is considered as background. (3) If a pixel has at least one higher neighbor which is part of the background, the pixel also has to be part of the background.[95]

When the blobs, respectively the diffraction spots, are isolated, the geometric centre of each blob is calculated according to [96]

$$x_s = \frac{\sum_i (x_{s,i} \cdot m_i)}{\sum_i m_i}, \quad y_s = \frac{\sum_i (y_{s,i} \cdot m_i)}{\sum_i m_i}, \quad (2.49)$$

where  $x_{s,i}$  and  $y_{s,i}$  are the  $x$  and  $y$  positions of the  $i$ -th pixel of a blob. Here the masses  $m_i$  equal 1 for all pixels. In Fig 2.8(a) the detected geometrical centers are marked by the green squares. Finally the averaged distances between the geometric centers reveal the half lattice constants  $a$  and  $c$ , as described in Sec. 2.3.1.

## 2.4 Scanning near-field optical microscopy

The scanning near-field optical microscope (SNOM) is an optical microscope that can resolve structures beyond the Abbe diffraction limit (cf. Eq. 2.38) by utilizing

the fact that reflected light exhibits two components. Instead of the propagating component that is known as far-field, the evanescent component which is related to the near-field is probed.[97] The information about the evanescent component can be collected by bringing a small aperture with an optical fibre close to the surface. The distance between optical fibre and surface, as well as the diameter of the fibre, needs to be smaller than the wavelength of the reflected light.[97] With this method the resolution is limited by the geometry of the aperture instead of the wavelength of the illuminating light.

SNOM images in this thesis were obtained with a scattering-type SNOM instead of an aperture-SNOM. The scattering-type SNOM is based on an atomic-force microscope (AFM), which is operated in tapping mode. The frequency is adjusted so that the cantilever is excited to a sine wave oscillation just below its resonance frequency [97, 98]

$$\omega_r = \sqrt{\frac{K - \frac{\delta F}{\delta z}}{m}}, \quad (2.50)$$

where  $K$  denotes the spring constant of the cantilever,  $\delta z$  its displacement and  $m$  its mass.  $F$  is the force experienced by the cantilever. When scanning over the surface the resonance of the cantilever changes depending on the interaction between its apex and the sample. Cantilever and sample are attracted by the long range van der Waals' forces and capillary actions, while they are repulsed by the short range coulomb force. The resulting force between two atoms (one at the cantilever apex and one at the sample's surface),[97]

$$F \approx \frac{A}{d^{12}} - \frac{B}{d^6}, \quad (2.51)$$

depends on the distance  $d$  between cantilever apex and sample.  $A$  and  $B$  are constants. The deflection of the cantilever is recorded using a laser beam reflected at its backside.[68] In order to keep the oscillation amplitude of the cantilever constant, a feedback circuit adjusts the distance between cantilever apex and sample, changing the interaction force.[68] This way the topography at a constant force gradient is imaged.[68]

In order to obtain optical information about the surface, the AFM is extended by an additional laser beam which is focussed on the surface below the cantilever

apex. The tapping mode of the AFM leads to a modulation of the laser beam with the tapping frequency.[98] The guiding of the laser beam inside the microscope is constructed as a Michelson interferometer. The incoming laser beam is separated into two equal beams by a ZnSe window. One beam is focussed on the sample and is scattered there. The backscattered beam is interfered with the other beam, which in the meantime passes a reference beam path. The interfered beam is guided to a liquid nitrogen cooled MCT (Mercury-Cadmium-Telluride) detector and demodulated by a lock-in amplifier.[98] The linear component of the signal corresponds to the far-field. The optical near-field signal exhibits a non-linear dependence and is obtained from the components of higher harmonic order ( $n \geq 2$ ).[98]

The near-field signal obtained in this manner primarily shows a material contrast [99–102] determined by the dielectric constant.[103] In addition, the near-field signal is sensitive to strain.[98, 104, 105] Overall, with this kind of microscope, the topographic information (with AFM) and the optical near-field image (with SNOM) of a surface are obtained simultaneously.

## 2.5 Stress and strain

Heterostructures, such as those investigated here, contain non-lattice matched layers. This induces deformations of the lattice. Deformations of a material are expressed by strain, while stress describes internal forces in a material. Stress is defined as force per area and thus has the dimension of pressure. Stress can induce strain and vice versa. Within the elastic framework, this effect is described by Hooke's law, which in Voigt notation is given by

$$\underline{\tau} = \underline{\underline{C}} \cdot \underline{\varepsilon}, \quad (2.52)$$

with  $\underline{\tau}$  being the stress tensor,  $\underline{\underline{C}}$  the elastic stiffness tensor, and  $\underline{\varepsilon}$  the strain tensor.[106] The strain coefficients  $\varepsilon_{xx}$ ,  $\varepsilon_{yy}$  and  $\varepsilon_{zz}$  describe distortions along the respective axes, while  $\varepsilon_{xy}$ ,  $\varepsilon_{yz}$  and  $\varepsilon_{zx}$  specify changes of the angles between the basis vectors (shear strains).[106] In the wurtzite structure the  $x$  and  $y$  axes are associated with an  $a$  and the perpendicular  $m$  direction, respectively. With the

$z$  axis oriented parallel to the  $c$  direction, the elastic stiffness tensor has only five independent components and is reduced to [107]

$$\underline{\underline{C}} = \begin{pmatrix} C_{11} & C_{12} & C_{13} & 0 & 0 & 0 \\ C_{12} & C_{11} & C_{13} & 0 & 0 & 0 \\ C_{13} & C_{13} & C_{33} & 0 & 0 & 0 \\ 0 & 0 & 0 & C_{44} & 0 & 0 \\ 0 & 0 & 0 & 0 & C_{44} & 0 \\ 0 & 0 & 0 & 0 & 0 & \frac{C_{11}-C_{12}}{2} \end{pmatrix}. \quad (2.53)$$

The elastic constants of wurtzite structure GaN, AlN and InN are summarized in Tab. 9.1. The values of GaN were measured by Polian *et al.* [108] using Brillouin scattering, while the elastic constants of AlN and InN were derived by Wright [109] using density-functional-theory calculations. The elastic constants of  $\text{Al}_{0.81}\text{In}_{0.19}\text{N}$  are calculated by linear interpolation between the values of AlN and InN. Thus, the elastic stiffness tensor for GaN is

$$\underline{\underline{C}}_{\text{GaN}} = \begin{pmatrix} 390 & 145 & 106 & 0 & 0 & 0 \\ 145 & 390 & 106 & 0 & 0 & 0 \\ 106 & 106 & 398 & 0 & 0 & 0 \\ 0 & 0 & 0 & 105 & 0 & 0 \\ 0 & 0 & 0 & 0 & 105 & 0 \\ 0 & 0 & 0 & 0 & 0 & 122.5 \end{pmatrix} \text{GPa}. \quad (2.54)$$

The respective elastic stiffness tensor for  $\text{Al}_{0.81}\text{In}_{0.19}\text{N}$  is

$$\underline{\underline{C}}_{\text{Al}_{0.81}\text{In}_{0.19}\text{N}} = \begin{pmatrix} 363 & 133 & 105 & 0 & 0 & 0 \\ 133 & 363 & 105 & 0 & 0 & 0 \\ 105 & 105 & 355 & 0 & 0 & 0 \\ 0 & 0 & 0 & 103 & 0 & 0 \\ 0 & 0 & 0 & 0 & 103 & 0 \\ 0 & 0 & 0 & 0 & 0 & 115 \end{pmatrix} \text{GPa}. \quad (2.55)$$

In an orthotropic material the components of the inverse elastic stiffness tensor,  $\underline{\underline{S}}$ , are associated with the Young's moduli  $E_i$  along axis  $i$ , the shear moduli  $G_{ij}$  in direction  $j$  on a plane with normal direction  $i$ , and Poisson's ratios  $\nu_{ij}$  by the

	GaN	AlInN		GaN	AlInN		GaN	AlInN
$E_1$ (GPa)	324.08	300.30	$G_{12}$ (GPa)	122.50	103.09	$\nu_{12}$	0.323	0.303
$E_2$ (GPa)	324.08	300.30	$G_{13}$ (GPa)	105.00	103.09	$\nu_{13}$	0.180	0.210
$E_3$ (GPa)	356.00	300.30	$G_{23}$ (GPa)	105.00	115.21	$\nu_{23}$	0.180	0.210

**Table 2.1:** Young's moduli  $E_i$  along axis  $i$ , shear moduli  $G_{ij}$  in direction  $j$  on a plane with normal direction  $i$ , and Poisson's ratios  $\nu_{ij}$  for GaN and  $\text{Al}_{0.81}\text{In}_{0.19}\text{N}$  calculated from the inverse stiffness tensors.

relation

$$\underline{\underline{S}} = \begin{pmatrix} \frac{1}{E_1} & -\frac{\nu_{21}}{E_2} & -\frac{\nu_{31}}{E_3} & 0 & 0 & 0 \\ -\frac{\nu_{12}}{E_1} & \frac{1}{E_2} & -\frac{\nu_{32}}{E_3} & 0 & 0 & 0 \\ -\frac{\nu_{13}}{E_1} & -\frac{\nu_{23}}{E_2} & \frac{1}{E_3} & 0 & 0 & 0 \\ 0 & 0 & 0 & \frac{1}{G_{23}} & 0 & 0 \\ 0 & 0 & 0 & 0 & \frac{1}{G_{31}} & 0 \\ 0 & 0 & 0 & 0 & 0 & \frac{1}{G_{12}} \end{pmatrix}. \quad (2.56)$$

Thus, in order to derive these constants, the elastic stiffness tensors of GaN and  $\text{Al}_{0.81}\text{In}_{0.19}\text{N}$  are inverted and Young's moduli, shear moduli and Poisson's ratios are calculated for both materials, respectively. The derived values are presented in Tab. 2.1.

The strain coefficients  $\varepsilon_j$ , with  $j = xx, yy, zz, xy, yz, zx$ , of the  $\text{Al}_{1-x}\text{In}_x\text{N}/\text{GaN}$  heterostructures are obtained as outlined in the following: In heterostructures stress develops at the interfaces between different materials if the lattice constants do not match. In the general case of  $\text{Al}_{1-x}\text{In}_x\text{N}$ , with  $x$  being the In content, grown on  $c$ -plane GaN, stress in  $a$  and  $m$  direction occurs if the  $a$  lattice constant of GaN and  $\text{Al}_{1-x}\text{In}_x\text{N}$  differs by  $\Delta a$ . Since the distance between lattice planes in  $m$  direction linearly depends on the  $a$  lattice constant ( $d = \sqrt{3}/2 \cdot a$ ), the strain coefficients  $\varepsilon_{xx}$  and  $\varepsilon_{yy}$  in  $a$  and  $m$  direction are equal:

$$\varepsilon_{yy} = \frac{\Delta d}{d} = \frac{\sqrt{3}/2 \cdot \Delta a}{\sqrt{3}/2 \cdot a} = \frac{\Delta a}{a} = \varepsilon_{xx}. \quad (2.57)$$

Thus, they are defined as

$$\varepsilon_{xx} = \varepsilon_{yy} = \frac{a_{\text{Al}_{1-(x \pm \Delta x)}\text{In}_{x \pm \Delta x}\text{N}} - a_{\text{GaN}}}{a_{\text{GaN}}}. \quad (2.58)$$

In contrast, in  $c$  direction stress only develops if the  $c$  lattice constant of  $\text{Al}_{1-x}\text{In}_x\text{N}$  changes within an  $\text{Al}_{1-x}\text{In}_x\text{N}$  layer, for example due to variations  $\Delta x$  of the composition. Then the strain coefficient  $\varepsilon_{zz}$  in  $c$  direction is calculated by

$$\varepsilon_{zz} = \frac{C_{\text{Al}_{1-(x\pm\Delta x)}\text{In}_{x\pm\Delta x}\text{N}} - C_{\text{Al}_{1-x}\text{In}_x\text{N}}}{C_{\text{Al}_{1-x}\text{In}_x\text{N}}}. \quad (2.59)$$

For homogenous layers ( $\Delta x = 0$ ) this component is zero. It is assumed that no shear stress exists. Thus the strain coefficients  $\varepsilon_{xy}$ ,  $\varepsilon_{yz}$  and  $\varepsilon_{zx}$  are zero.

With this information the stress for each orthogonal-anisotropic spatial direction is calculated by substituting  $\underline{C}_{\text{Al}_{0.81}\text{In}_{0.19}\text{N}}$  (Eq. 2.55) and the components  $\varepsilon_j$  (Eqs. 2.58 and 2.59) into Eq. 2.52.

## 2.6 Polarization

The total macroscopic polarization  $\underline{P}$  of a solid is composed of a spontaneous polarization  $\underline{P}_{\text{sp}}$  of the equilibrium structure and a strain-induced piezoelectric polarization  $\underline{P}_{\text{pz}}$  [107]

$$\underline{P} = \underline{P}_{\text{sp}} + \underline{P}_{\text{pz}}. \quad (2.60)$$

Wurtzite structure nitride semiconductors, exhibit a spontaneous polarization along the [0001] direction, only. They thus exhibit one single polar axis.[107] Despite the presence of the spontaneous polarization, the electric field in the bulk of the semiconductor remains zero [110]

$$\underline{E}_{\text{bulk}} = \frac{\underline{D} - \underline{P}}{\varepsilon_r \varepsilon_0} = 0. \quad (2.61)$$

This is due to the dielectric displacement field  $\underline{D}$ , with  $\nabla \cdot \underline{D} = e \cdot (p - n)$ , where  $e$  is the elementary charge and  $p$  and  $n$  are the hole and electron densities, which compensate the spontaneous polarization. Thus, in the bulk the electrical displacement field counteracts the spontaneous polarization ( $\underline{D} = \underline{P}_{\text{sp}}$ ). At the surface of the semiconductor the discontinuity of the displacement field ( $\underline{D}_{\text{vac}} = 0$ ) induces an electrical field and thus a space charge region near the surface.[110] The electric field in the region of this two-dimensional electron gas depends on the material

parameters as well as on the surface conditions, i.e. the type of atomic plane (anion or cation plane) and the presence of surface states.[110,111]

The strain-induced piezoelectric polarization in Voigt notation is given by

$$\underline{P}_{\text{pz}} = \underline{e} \cdot \underline{\varepsilon} \quad (2.62)$$

and depends on the strain coefficients  $\varepsilon_j$ , whose derivation has already been discussed in Sec. 2.5.  $\underline{e}$  symbolizes the piezoelectric tensor.[106] In wurtzite structure semiconductors the tensor exhibits three non-vanishing components  $e_{13}$ ,  $e_{33}$ , and  $e_{15}$ :[106, 107]

$$\underline{e} = \begin{pmatrix} 0 & 0 & 0 & 0 & e_{15} & 0 \\ 0 & 0 & 0 & e_{15} & 0 & 0 \\ e_{31} & e_{31} & e_{33} & 0 & 0 & 0 \end{pmatrix}. \quad (2.63)$$

The strain-induced, piezoelectric polarization can thus be calculated according to Eq. 2.64.

$$\underline{P}_{\text{pz}} = \begin{pmatrix} e_{15}\varepsilon_{xz} \\ e_{15}\varepsilon_{yz} \\ e_{31}(\varepsilon_{xx} + \varepsilon_{yy}) + e_{33}\varepsilon_{zz} \end{pmatrix} \quad (2.64)$$

The piezoelectric coefficients  $e_{15}$ ,  $e_{31}$ , and  $e_{33}$  for wurtzite structure GaN, AlN and InN are presented in Tab. 9.1. The coefficients for different compositions of  $\text{Al}_{1-x}\text{In}_x\text{N}$  may be derived by linear interpolation between AlN and InN.

## 2.7 Concepts of roughness analysis

### 2.7.1 Power-Spectral Density

The power-spectral density function displays the spatial frequency spectrum of the roughness of a profile. Ideally it shows the complete frequency spectrum although in reality it is *band-limited*, meaning that it is limited by the spacing of the profile's discrete data points. Nevertheless, the derivation of the PSD is the most reliable way to determine the roughness of a surface.[112]

A height profile can be interpreted as the superposition of an infinite number of sine functions with different amplitudes and frequencies. A non-infinite profile therefore can be described by a finite Fourier series. The PSD is defined as the square of the Fourier coefficients of the height profile  $z$  or of the auto-covariance function:[112]

$$P_N(m) = \left( \frac{\tau_0}{N} \right) \left| \sum_{n=0}^{N-1} z_n e^{-2\pi i m n / N} \right|^2 K(m), \quad -N/2 \leq m \leq N/2, \quad (2.65)$$

where  $P_N(m)$  is the  $m$ -th term of the PSD,  $N$  is the number of the profile's data points  $z_n$ , and  $\tau_0$  is the distance between them. The factor  $K(m)$  equals  $1/2$  at the ends ( $m = \pm N/2$ ) of the PSD and is 1 everywhere else.

The PSD spectrum is used to obtain the profile's roughness  $R$  and correlation length  $c_L$ . In frequency domain, the PSD spectra obtained in this thesis, can be described by an exponential decay

$$\tilde{G}(f) = (\pi a / b) \cdot \exp(-bk), \quad k = 2\pi f, \quad (2.66)$$

with a Lorentzian function real-space equivalent,[113] which can be written as [114]

$$G(x) = \frac{a}{x^2 + b^2}. \quad (2.67)$$

$b$  is the half width at half maximum and  $a/b^2$  the maximum of the Lorentzian function. The correlation length  $c_L$  is a measure of the extent of surface features and hence can be defined as the half width at half maximum  $b$  of the Lorentzian function. The roughness  $R$  is a measure of the intensity of a certain feature and can be derived from the amplitude of the Lorentzian function ( $\sqrt{a/b^2}$ ).

In order to derive  $R$  and  $c_L$ , the PSD spectrum in frequency domain is plotted in logarithmic scale and selected regions of the spectrum are approximated by straight lines with slope  $m$  and  $y$ -axis intercept  $y_0$ . Following Eq. 2.66,  $m$  and  $y_0$  are defined as:

$$\ln(\tilde{G}(f)) = \underbrace{\ln\left(\frac{\pi a}{b}\right)}_{y_0} + \underbrace{(-2\pi b)}_m f. \quad (2.68)$$

Thus,  $c_L$  and  $R$  can be calculated from the slope  $m$  and the  $y$ -axis intercept  $y_0$  of

the fitted linear functions:

$$\begin{aligned} c_L = b &= -\frac{m}{2\pi}, \\ R^2 = \frac{a}{b^2} &= \frac{1}{\pi b} e^{y_0}. \end{aligned} \quad (2.69)$$

Error propagation yields

$$\begin{aligned} \Delta c_L &= -\frac{\Delta m}{2\pi}, \\ \Delta R &= \left( \frac{1}{m^2} \Delta m - \frac{1}{m} \Delta y_0 \right) \cdot \frac{1}{R} e^{y_0}. \end{aligned} \quad (2.70)$$

## 2.7.2 Auto-Covariance and Auto-Correlation Function

The *auto-covariance function* (ACF) is a measure of the correlation of the roughness of a surface. It is computed by the sum over the multiplication of all points  $z_i$  of the height profile with the points  $z_{i+l}$  that are shifted by the so called *lag length*  $l$ . At a certain lag length the mirror symmetrical auto-covariance function  $G(l)$  is defined as:[112]

$$G(l) = \frac{1}{N} \sum_{i=1}^{N-l} z_i \cdot z_{i+l}, \quad l = -N + 1, \dots, -1, 0, 1, \dots, N - 1, \quad (2.71)$$

where  $N$  is the number of data points. Since the sum over  $i$  only adds up to  $N - l$  the number of summands decreases with increasing  $l$ . Nevertheless every term is divided by  $N$  which decreases the values of  $G(l)$  linearly from  $G(0)$  to  $G(\pm N \mp 1)$ . The normalized auto-covariance function  $G(l)/G(0)$  is called the *auto-correlation function*.

Positive values of the ACF indicate a correlation. Anti-correlation leads to negative values of  $G(l)$ .

The value  $\sqrt{G(0)}$  equals the definition of the rms-roughness  $R$  as the root-mean-square deviation of the values  $z_i$  from the mean height of the profile

$$R = \sqrt{\frac{1}{N} \sum_{i=1}^N z_i^2}. \quad (2.72)$$

The correlation length  $c_L$  of the ACF is defined as the value where the function  $G(l)$  drops to  $1/e$  of its value  $G(0)$  for the first time, with  $e$  being Euler's number.

### 2.7.3 Cross-Covariance and Cross-Correlation Function

The *cross-covariance function* (CCF) shows the correlation between two different profiles a and b of the same length. Contrary to the auto-covariance function the cross-covariance function is not mirror symmetrical. The CCF  $G_{ab}(l)$  for a certain lag length is defined as:

$$G_{ab}(l) = \frac{1}{N} \sum_{i=1}^{N-l} z_{a_i} \cdot z_{b_{i+l}}, \quad l = -N + 1, \dots, -1, 0, 1, \dots, N - 1, \quad (2.73)$$

where  $z_{a_i}$  and  $z_{b_i}$  are the  $i$ -th height values of the two profiles a and b.  $N$  is the number of data points of the profiles. A peak in the CCF at a lag length  $l$  is caused by a structural correlation of the profiles a and b in that distance.



# Chapter 3

## Experimental details

### 3.1 Cross-sectional scanning tunneling microscopy

All scanning tunneling microscopy (STM) measurements in this thesis were performed with an Omicron VT system at a pressure of  $\sim 2 \times 10^{-10}$  mbar. The microscope was operated in the constant-current and in the point spectroscopy mode.

#### 3.1.1 Sample preparation and cleavage

For cross-sectional STM investigations samples are cut from a wafer into rectangular shaped pieces of  $\sim 2 \times 4 \text{ mm}^2$  and thinned to 100-150  $\mu\text{m}$  by grinding and subsequent polishing. Afterwards Au contacts are sputtered onto one half of the sample from both sides. By discharging a capacitor at several points across the Au layer, Au is merged with the underlying semiconductor. This provides ohmic contacts. The sample is glued to a small cube of stainless steel with an electrically conducting two-component adhesive. In this geometry the sample can be installed in a sample holder (cf. Fig. 3.1(a)) and is electrically contacted from both sides. After preparation the sample holder with the sample is directly installed into the load lock attached to the vacuum chamber of the scanning tunneling microscope, in order to minimize contaminations.

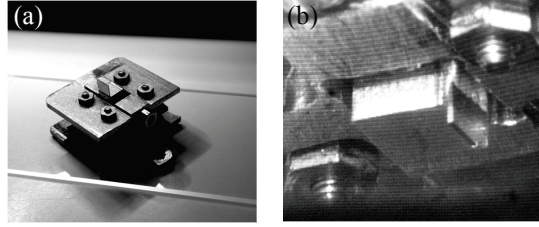


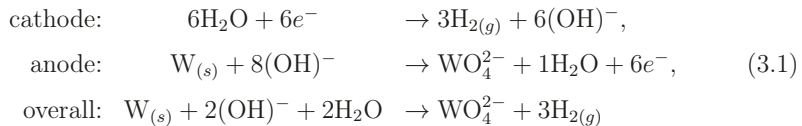
**Figure 3.1:** (a) The thinned and Au-contacted sample is glued to a cube of stainless steel and installed in a sample holder. (b) Cleaved sample in the analysis chamber of the scanning tunneling microscope.

The cleavage of samples in ultrahigh vacuum ( $p < 10^{-8}$  Pa) yield clean ( $10\bar{1}0$ ) surfaces. For cleavage the upper part of the sample is pushed against a cleavage tool which applies uniform pressure to the sample. Ideally the cleavage plane is atomically flat and located slightly above the cube of steel. The freshly cleaved surfaces are investigated by STM without interruption of the vacuum.

### 3.1.2 Tip preparation

For all STM investigations in this thesis tungsten tips are used. The tips are manufactured by electrochemical etching with sodium hydroxide solution (NaOH): A tungsten wire with a diameter of 0.25 nm is placed in a holder and is thread through a platinum loop holding a thin film of diluted NaOH solution. A small piece of wire of about 3-4 mm protrudes below the ring. The top of this lower section of the tungsten wire is used as tip.

In order to perform a controlled etching process, a voltage is applied between the tungsten wire and the platinum loop. With the tungsten wire as the anode, W is oxidized to  $\text{WO}_4^{2-}$  (cf. Eq. 3.1).[115]



Short pulses of reversed voltage are applied in order to dissolve the oxide in the liquid, and thereby preventing it from depositing onto the tungsten wire.[116]

Once the diameter of the wire is etched thin enough, the wire tears and the bottom section with the etched tip drops down. It is absorbed by shaving cream filled into a beaker glass in order to avoid damaging the tip. The tip is cleaned from shaving cream and residues from etching in warm distilled water and ethanol. Afterwards the tip is installed in a tip holder and directly transferred into the vacuum chamber of the scanning tunneling microscope in order to minimize contamination and oxidation.

The shape of the tip is strongly influenced by the thickness and concentration of the NaOH film inside the platinum loop. For example etching the tip with a film that exhibits only a low concentration of NaOH results in a slow etching process. If the NaOH concentration of the film is too high, large bubbles form that may lead to a non-uniform shape of the tip. The best results were achieved for a 2 molar NaOH solution and a NaOH film of less than 0.7 nm thickness. Tungsten tips etched with this setup typically exhibit a radius of curvature at their apex of about 10 nm.[117,118]

## **3.2 Cross-sectional atom force microscopy and scanning near-field optical microscopy**

For cross-sectional atomic force microscopy (AFM) and scanning near-field optical microscopy (SNOM) investigations, a scattering-type SNOM (NeaSNOM from Neaspec) at the Fraunhofer Institute for Laser Technology (ILT) is used.[98] For probing the optical signal an IR broadband laser developed at Fraunhofer ILT is used.[119] It is tunable between 9  $\mu\text{m}$  and 16  $\mu\text{m}$  wavelength at several mW.

The cleaved samples already measured by STM are investigated cross-sectionally. The measurements were performed on air.

### 3.3 Cross-sectional scanning transmission electron microscopy

For cross-sectional STEM measurements samples are prepared by ion beam milling. A final cleaning is performed with low energy  $\text{Ar}^+$  ion bombardment (0.5 eV) at liquid  $\text{N}_2$  temperature using a Fischione Nanomill system. Structural investigations were performed using a FEI Titan STEM equipped with a spherical aberration corrector at the condenser plane.[P2]

### 3.4 Sample specifications

All three investigated  $\text{Al}_{1-x}\text{In}_x\text{N}/\text{GaN}$  heterostructures were grown by MOVPE on an AIXTRON 200/4 RF-S system at École Polytechnique Fédérale de Lausanne (EPFL) in the Advanced Semiconductors for Photonics and Electronics Lab (LASPE). The layer thicknesses and the In contents were determined by high resolution X-ray diffraction (HRXRD). In all samples In contents between 17.9% and 20% were found. At this In content the  $\text{Al}_{1-x}\text{In}_x\text{N}$  layers are almost lattice-matched to GaN along the  $a$  direction.[19] Each  $\text{Al}_{1-x}\text{In}_x\text{N}$  layer is unintentionally  $n$ -doped with a carrier concentration of presumably  $\sim 10^{19} \text{ cm}^{-3}$ . The three investigated samples include two  $\text{Al}_{1-x}\text{In}_x\text{N}/\text{GaN}$  distributed Bragg reflector (DBR) structures and one  $\text{Al}_{1-x}\text{In}_x\text{N}/\text{GaN}$  heterostructure with five  $\text{Al}_{1-x}\text{In}_x\text{N}$  layers.

#### 3.4.1 A2314

The  $\text{Al}_{0.80}\text{In}_{0.20}\text{N}/\text{GaN}$  distributed Bragg reflector structure consists of 42 pairs of 48.6 nm  $\text{Al}_{0.80}\text{In}_{0.20}\text{N}$  followed by 36.5 nm GaN, deposited onto a 1  $\mu\text{m}$  thick GaN [Si:  $3 \times 10^{18} \text{ cm}^{-3}$ ] buffer layer. The heterostructure was grown on a  $c$ -plane GaN Lumilog substrate with a carrier concentration of  $\sim 3 \times 10^{18} \text{ cm}^{-3}$ . The GaN interlayers are unintentionally doped ( $< 10^{15} \text{ cm}^{-3}$ ). HRXRD measurements suggest an In content  $x$  of  $20 \pm 0.5\%$ , which is slightly reduced at the  $\text{Al}_{1-x}\text{In}_x\text{N}$ -to-GaN interface. At the interfaces between GaN and the deposited  $\text{Al}_{0.80}\text{In}_{0.20}\text{N}$ , a two-dimensional electron gas (2DEG) is expected to occur with a density of

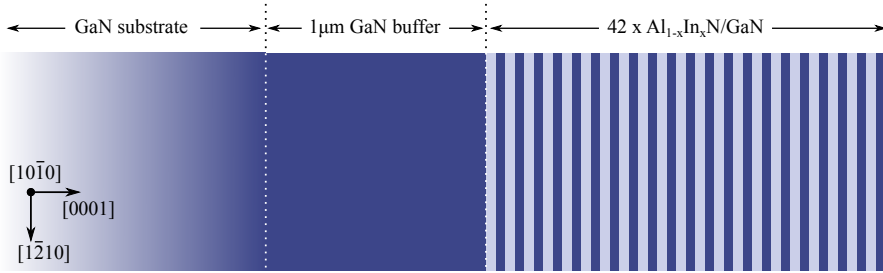


**Figure 3.2:**  $\text{Al}_{1-x}\text{In}_x\text{N}/\text{GaN}$  DBR heterostructure. In sample A2314 42 pairs of 48.6 nm  $\text{Al}_{1-x}\text{In}_x\text{N}$  followed by 36.5 nm GaN are deposited on a 1  $\mu\text{m}$  thick GaN buffer layer grown on  $c$ -plane FS-GaN. In A2688 the  $\text{Al}_{1-x}\text{In}_x\text{N}$  layers exhibit a thickness of 45 nm while the GaN layers are 41.5 nm thick.  $\text{Al}_{1-x}\text{In}_x\text{N}$  is depicted in gray, while GaN is illustrated in blue.

$\sim 2.5 \times 10^{13} \text{ cm}^{-2}$ . The structure is illustrated in Fig. 3.2, where  $\text{Al}_{1-x}\text{In}_x\text{N}$  is depicted in gray, while GaN is illustrated in blue.

### 3.4.2 A2688

The second distributed Bragg reflector structure was grown on a double side-polished Sumitomo  $c$ -plane free-standing GaN [ $\text{Si}: > 10^{18} \text{ cm}^{-3}$ ] substrate. 42 pairs of 45 nm  $\text{Al}_{1-x}\text{In}_x\text{N}$  followed by 41.5 nm GaN were deposited onto a 1  $\mu\text{m}$  thick GaN buffer layer (cf. Fig. 3.2). Again the GaN interlayers are unintentionally doped. In analogy to sample A2314, a 2DEG is expected to develop at one interface. HRXRD measurements reveal that the In content in  $\text{Al}_{1-x}\text{In}_x\text{N}$  fluctuates from period to period and/or within an  $\text{Al}_{1-x}\text{In}_x\text{N}$  layer between 20.5% and 17.9%.

### 3.4.3 A3162

The  $\text{Al}_{0.81}\text{In}_{0.19}\text{N}/\text{GaN}$  heterostructure consists of five repetitions of 31 nm thick  $\text{Al}_{0.81}\text{In}_{0.19}\text{N}$  layers separated by 105 nm thick GaN [ $\text{Si}: 8 \times 10^{17} \text{ cm}^{-3}$ ] layers as is shown in Fig. 3.3. The sample was grown by MOVPE at a temperature of 740  $^\circ\text{C}$ . The heterostructure was deposited on a 500 nm thick GaN [ $\text{Si}: 3 \times 10^{18} \text{ cm}^{-3}$ ] buffer

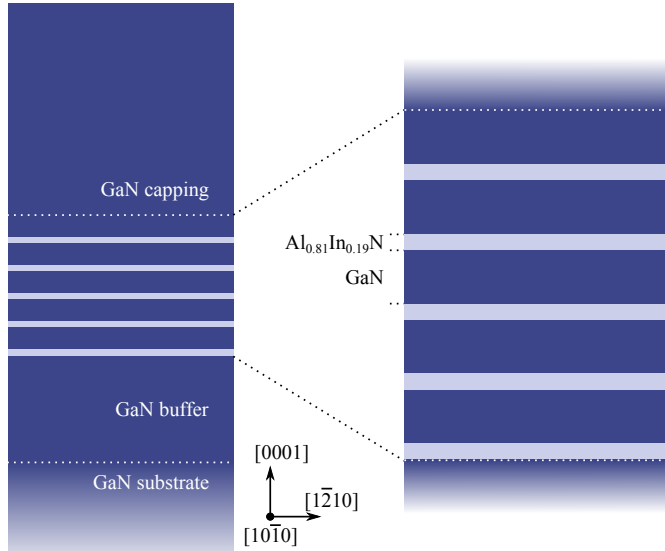


**Figure 3.3:** GaN/Al<sub>0.81</sub>In<sub>0.19</sub>N heterostructure. Five repetitions of of 31 nm Al<sub>0.81</sub>In<sub>0.19</sub>N separated by 105 nm GaN are deposited on a 500 nm thick GaN buffer layer grown on *c*-plane FS-GaN and capped by a 1  $\mu\text{m}$  GaN layer.

layer grown on a *c*-plane free standing (FS) GaN Sumitomo substrate and capped by a 1  $\mu\text{m}$  GaN [Si:  $5 \times 10^{18} \text{ cm}^{-3}$ ] layer. In the HRXRD measurement no indication of indium loss at interfaces or intermixing was found. An In content of  $19.15 \pm 0.5\%$  was determined.

# Chapter 4

## Electronic properties of the $\text{Al}_{1-x}\text{In}_x\text{N}(10\bar{1}0)$ surface

*Text and images in this Chapter are adapted from [P1] (cf. list of own publications, p. 137).*

The increasing interest in growth on non-polar planes, driven by the absence of out of plane electric fields, caused by piezoelectric and spontaneous polarization mismatch, raises the question of the electronic properties of  $m$ -plane surfaces. It is known that the presence of surface states and the Fermi level position at the growth surface critically affect atomic processes during growth, such as the incorporation of dopants and impurities.[54, 55] However, current knowledge about the electronic structure of non-polar surfaces is limited to GaN and InN, only.[120–124] Hence, the lack of knowledge of the electronic structure of  $\text{Al}_{1-x}\text{In}_x\text{N}$  non-polar surfaces is detrimental for achieving controlled growth conditions along non-polar directions. Here, the electronic structure of  $\text{Al}_{1-x}\text{In}_x\text{N}(10\bar{1}0)$  cleavage surfaces is investigated by cross-sectional scanning tunneling microscopy (STM) and spectroscopy (STS) combined with density functional theory (DFT) calculations.

### 4.1 Experimental results

A cross-sectional view of a cleavage surface of sample A2314 is shown in Fig. 4.1 in which from left to right the GaN buffer layer and the first six  $\text{Al}_{0.80}\text{In}_{0.20}\text{N}/\text{GaN}$

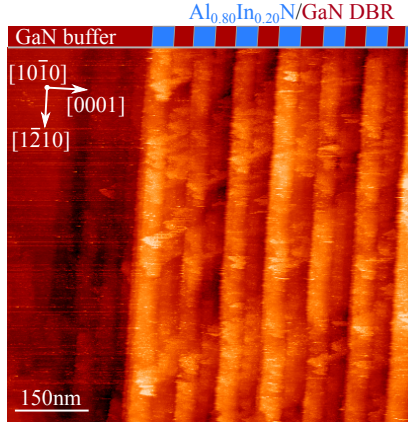


**Figure 4.1:** Cross-sectional STM overview image of the  $\text{Al}_{0.80}\text{In}_{0.20}\text{N}/\text{GaN}$  distributed Bragg reflector heterostructure A2314 measured at  $+3.8\text{ V}$  and  $100\text{ pA}$ . In the STM image the  $\text{Al}_{0.80}\text{In}_{0.20}\text{N}$  layers appear brighter than the surrounding GaN. On the left hand side part of the GaN buffer is visible. The image is adapted from [P1].

pairs of the DBR heterostructure can be identified. The  $\text{Al}_{0.80}\text{In}_{0.20}\text{N}$  layers appear brighter than the surrounding GaN. Scanning tunneling spectra were measured at the  $\text{Al}_{1-x}\text{In}_x\text{N}$  layers of this surface and various cleavage surfaces of samples A2314, A2688, and A3162. The black dots in Fig. 4.2 show an example of an  $I(V)$  tunnel spectrum that was obtained on A3162. All measured spectra show a typical semiconducting behavior, with a tunnel current at positive and negative voltages, separated by an asymmetric  $\sim 3\text{ V}$  wide voltage range, where no tunnel current is detected. This is the signature of the band gap of the semiconductor.[71] Here, the onset voltages of the tunnel current are at  $+2\text{ V}$  and  $-1\text{ V}$ , respectively.

In order to interpret the measured tunnel spectra, simulations of the tunnel current with a 3D finite difference calculation are performed. The electrostatic potential is computed for a tip-vacuum-semiconductor system by solving the Poisson equation and additionally the continuity equations for electrons and holes following the methodology in Refs. [69, 78] as is described in Chap. 2.2. The simulated tunnel currents are shown in Fig. 4.2 as lines for both unpinned and pinned  $\text{Al}_{1-x}\text{In}_x\text{N}(10\bar{1}0)$  surfaces.

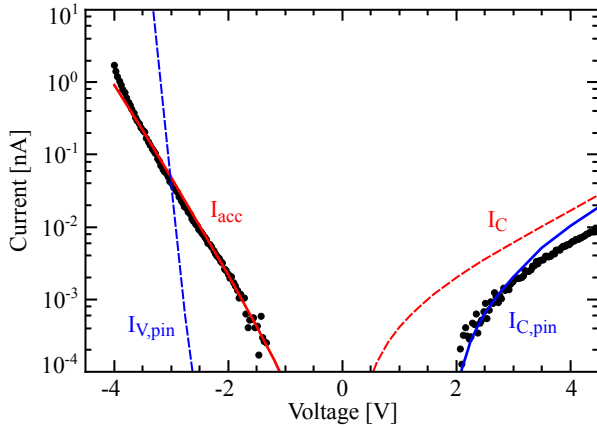


**Figure 4.2:** Scanning tunneling spectroscopy measured on the  $\text{Al}_{0.81}\text{In}_{0.19}\text{N}(10\bar{1}0)$  surface in sample A3162. The experimental data is represented by the black dots measured at a tip-sample separation fixed by a set voltage of  $-3.6\text{ V}$  and a set current of  $150\text{ pA}$ . The lines illustrate calculations of the tunnel current assuming no intrinsic surface state within the band gap (red) and an empty surface state at  $E_C - 1.8\text{ eV}$ , which pins the Fermi energy (blue). All simulations are performed for the same tip-sample separation. The image is adapted from [P1].

The unpinned case, where no surface state is included in the calculation, is represented by the red solid and dashed lines. Without pinning, the electric field between tip and semiconductor penetrates into the semiconductor and induces a band bending. At negative voltages the tip-induced downward band bending drags the conduction band edge  $E_C$  below the Fermi energy ( $E_F$ ), inducing an electron accumulation in the conduction band. The electrons in this accumulation zone can tunnel into the tip at negative voltages corresponding to energies within the band gap (cf. Chap. 2.2.3, Fig. 2.5(d)). Hence, a tunnel current flows at small negative voltages already. This calculated accumulation tunnel current ( $I_{\text{acc}}$ ) fits well to the measured data. Note, the tip-sample separation and the electron affinity were used as fit parameters to adjust the tunnel current at negative voltages. At positive voltages electrons are expected to tunnel from the tip into the empty conduction band. However, because of the  $n$ -type doping the calculation without pinning yields a too high tunnel current  $I_C$  and an onset voltage too close to zero (cf. Chap. 2.2.3, Fig. 2.5(a) and (b)). Hence, it does not describe the measured onset around  $+2\text{ V}$ .

For calculating the pinned case an intrinsic empty surface state was added 1.8 eV below the conduction band edge with a FWHM of 0.2 eV and a density of  $7 \times 10^{13} \text{ cm}^{-2}$ . This concentration value corresponds to the concentration of In atoms in the surface layer, where the dangling bond state is localized (see below). For the calculation of the pinned surface the same tip-sample separation is used as for the unpinned surface. The simulated tunnel spectra of the pinned surface are illustrated by the blue solid and dashed lines in Fig. 4.2. The pinning removes the tip-induced band bending and thus at negative voltages no accumulation of electrons in the conduction band occurs. Thus the current is solely given by tunneling from the valence band into the tip ( $I_{V,\text{pin}}$ ), which is however too small (cf. Chap. 2.2.3, Fig. 2.6(a)). At positive voltages the midgap pinning shifts the onset of electrons tunneling from the tip into the conduction band ( $I_{C,\text{pin}}$ ) to higher voltages. This model provides a good description of the tunnel current at positive voltages for a surface state 1.8 eV below the conduction band edge. Thus, the best fit is obtained for an unpinned surface at negative voltages (solid red line in Fig. 4.2) and a surface pinned by a surface state at positive voltages (solid blue line in Fig. 4.2). This suggests a polarity-dependent pinning by the empty intrinsic surface state, in analogy to GaN(10 $\bar{1}$ 0) surfaces.[124]

## 4.2 DFT calculations of the $\text{Al}_{1-x}\text{In}_x\text{N}(10\bar{1}0)$ surface

In order to identify the origin of the midgap surface state, first principles calculations within DFT were performed using the local density approximation (LDA) and the projector augmented wave approach (PAW).[125, 126] In a first step the  $c$ -lattice constant (along  $\langle 0001 \rangle$ ) has been optimized for a 32 atom bulk supercell, which is biaxially strained in the basal plane to GaN and where the group-III sublattice is occupied with 3 In (and 13 Al) atoms, reflecting the In composition. Then the  $m$ -plane surfaces are modeled using slabs of 16-monolayers AlN with the aforementioned lattice constant. A plane-wave energy cutoff of 450 eV was used and the position of the atoms in the 8 topmost monolayers (MLs) was fully relaxed. The In semicore  $d$  states are treated explicitly as valence electrons, and the triply

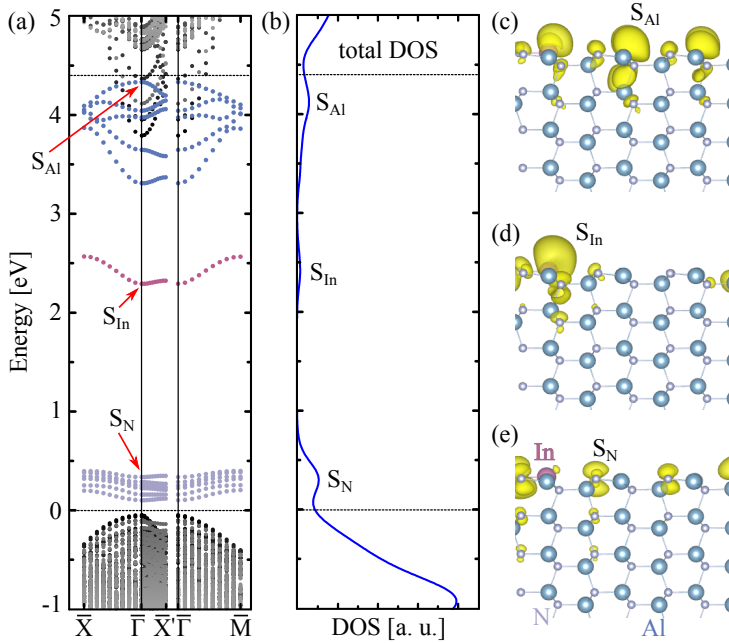


**Figure 4.3:** (a) Band structure of the  $Al_{0.83}In_{0.17}N(10\bar{1}0)$  surface.  $S_N$  denotes the occupied N-derived surface states,  $S_{In}$  the In-derived unoccupied surface state, and  $S_{Al}$  the unoccupied Al-derived surface states. Gray dots denote the projected band bulk structure of AlN at the lattice constant of  $Al_{0.83}In_{0.17}N$ . The upper and lower dashed horizontal lines at 4.4 eV and 0 eV mark the bulk CBM and VBM of AlN at its optimum lattice constant, respectively. The absolute position of the corresponding band structures has been obtained by aligning the bulk ionization potentials to the vacuum level. (b) Total density of states (DOS). (c), (d), (e) show the charge density of the  $S_{Al}$ ,  $S_{In}$ , and  $S_N$  states, respectively. Al, In, and N atoms are shown as medium-sized blue, large-sized purple, and small gray dots, respectively. The image is adapted from [P1].

coordinated lowermost Al and N atoms were passivated with pseudohydrogen atoms of partial charge 1.25 and 0.75, respectively. In the top layer one Al is replaced by an In atom. By modifying the lateral size of the supercell (i.e.,  $n \times m$ ,  $n$  and  $m$  denote the repetition along  $\langle 11\bar{2}0 \rangle$  and  $\langle 0001 \rangle$ , respectively) the surface In composition is effectively changed within the whole range between pure AlN and pure InN.

Figures 4.3(a) and (b) show the calculated band structure and density of states

(DOS), respectively, for the example of a  $2 \times 3$  surface unit cell with one In atom replacing a surface Al atom (corresponding to an In composition of 16.7% in the surface layer). In the band structure various states can be identified: Within the band gap a band of states (labeled  $S_N$ ) occurs at energies between 0 and 0.5 eV. The charge density of these states shown in Fig. 4.3(e) reveals that this band of states corresponds to the filled nitrogen dangling bonds with  $p$  orbital character. The next state in the band gap ( $S_{In}$ ) 2.4 eV above  $E_V$  corresponds to the empty dangling bond above the In atom as visible in Fig. 4.3(d). Finally, several surface states appear near the conduction band edge (labeled  $S_{Al}$ ). Figure 4.3(c) shows the charge density of the highest one. These states correspond to the empty Al dangling bonds. Both, the empty In and Al dangling bond states have a mixed  $s$  and  $p$  orbital character.

The blue dots in Fig. 4.4 illustrate the calculated energy minima of the lowermost empty In/Al-derived surface state  $S_{In}$  as a function of the In composition  $x$  of  $\text{Al}_{1-x}\text{In}_x\text{N}$ . The energies of the surface state minima are given relative to the valence band edge of pure AlN. The valence and conduction band edges shown as black and gray curves, respectively, were derived using composition-dependent bowing parameters calculated using a tight-binding (TB) model for the compositions marked by crosses.[127] The blue symbols illustrate that the lowermost empty dangling bond state is within the fundamental band gap for In compositions  $x \lesssim 0.6$ . For pure InN the empty surface state is within the conduction band in agreement with previous calculations and experiments.[54, 122] For pure AlN the surface state is located at midgap, consistent with previous calculations.[128]

### 4.3 Analysis of tunnel spectra obtained on the $\text{Al}_{1-x}\text{In}_x\text{N}(10\bar{1}0)$ surface

In order to compare the calculated results with the experiments, a large number of spectra, acquired on different cleavage surfaces of all three heterostructures with different W tips, was analyzed. All spectra exhibit similar onset voltages. In order to extract the energetic position  $E_{SS}$  of the lowermost empty surface state, each spectrum was simulated using the energy position  $E_{SS}$ , the electron affinity, and

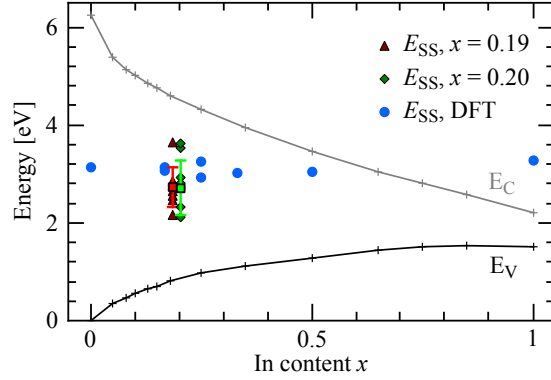


**Figure 4.4:** Energy position of the lowest empty cation derived surface state on  $\text{Al}_{1-x}\text{In}_x\text{N}(10\bar{1}0)$  surfaces as a function of the In composition  $x$ . The conduction ( $E_C$ , gray) and valence band ( $E_V$ , black) edges were taken from Ref. [127]. Blue dots show the calculated energy position of the empty cation-derived surface state. This state is the In-derived dangling bond (Al-derived surface states are significantly higher in energy), except for pure AlN where it is the Al-derived dangling bond. The green diamonds and red triangles show the energy of the surface state  $E_{SS}$  extracted from scanning tunneling spectra with the help of tunnel current simulations for  $\text{Al}_{0.80}\text{In}_{0.20}\text{N}$  and  $\text{Al}_{0.81}\text{In}_{0.19}\text{N}$  layers in heterostructure A2314, A2688, and A3162. The dark framed symbols with error bars show the respective average values. The image is adapted from [P1].

the tip-sample separation as fit parameters (cf. Chap. 5). This procedure is done in analogy to that discussed above for the spectrum shown in Fig. 4.2. The best fit of the onset voltage of the tunnel current at positive voltages is used as criterion to extract the energy of the lowest midgap surface state. The green diamonds and red triangles show the obtained surface state energy for the  $\text{Al}_{0.80}\text{In}_{0.20}\text{N}$  layers in A2314 and A2688 and for the  $\text{Al}_{0.81}\text{In}_{0.19}\text{N}$  layers in A3162, respectively. The respective average values are  $E_C - 1.80 \pm 0.56$  eV and  $E_C - 1.82 \pm 0.41$  eV. They are shown as dark framed symbols with error bars. The energy values of the surface state are measured *relative to the conduction band edge*  $E_C$ . In contrast, the calculated surface state energies are most accurate *relative to the valence band edge*  $E_V$ . Thus, if the experimental band gaps are larger than the calculated ones in Fig. 4.4, the experimental values of the surface state energy shift 1:1 upward relative to the calculated ones. Indeed, there are indications from experiments that the real band gap of  $\text{Al}_{0.81}\text{In}_{0.19}\text{N}$  is 4.2 eV, [129] i.e. 0.5 eV larger than the calculated one. Hence,

our experimental data points may need to be shifted up to 0.5 eV upward relative to the calculated ones. Independent of this uncertainty, the experimental results agree well with the calculated energy minima of the lowest empty surface state.

At this stage the origin of pinning is addressed. Although cleavage steps on the surface were frequently observed, the concentration of step states (assuming one state per lattice constant) is one order of magnitude lower than the surface density of In dangling bonds ( $S_{In}$ ). Hence, the steps cannot induce an extrinsic pinning. The polarity dependent Fermi level pinning is only due to the intrinsic In surface dangling bond state.

## 4.4 Conclusion

The electronic structure of  $Al_{1-x}In_xN(10\bar{1}0)$  surfaces was investigated by cross-sectional scanning tunneling spectroscopy and density functional theory calculations. The calculations yield empty Al and/or In-derived dangling bonds states within the band gap for In compositions smaller than 60%. The energy of the lowest empty In-derived surface state was extracted from tunnel spectra acquired on lattice matched  $Al_{1-x}In_xN$  layers with In compositions of  $x = 0.19$  and  $x = 0.20$  to be  $E_C - 1.82 \pm 0.41$  eV and  $E_C - 1.80 \pm 0.56$  eV, respectively, in good agreement with the calculated energies. Based on these results it can be concluded, that under growth conditions the Fermi level is pinned by the In-derived dangling bond state for In compositions smaller than about 60%. For larger In concentrations no Fermi level pinning is present.

# Chapter 5

## About the electron affinity

Scanning tunneling spectroscopy of the  $\text{Al}_{1-x}\text{In}_x\text{N}$  layers was performed on numerous cleavage surfaces of the samples A2314, A2688, and A3162, as was described in Chap. 4. The tunnel current depends on various parameters of the probe tip (e.g. the geometry and work function) and the investigated semiconductor (e.g. the carrier concentration and surface states) as well as on the tip-sample separation. Besides all of these, the electron affinity is a crucial parameter, since it affects the onset and slope of the tunnel current. In order to fit simulations to the experimentally obtained tunnel spectra of  $\text{Al}_{1-x}\text{In}_x\text{N}$ , an accurate knowledge of this parameter is required. However, a literature survey reveals that even for well-known materials such as GaN a broad range of experimentally and theoretically obtained values were reported for the electron affinity and a commonly accepted value is not established yet despite the importance for semiconductor interfaces in general. An overview of the numerous values of  $\chi$  is given in Tab. 5.1 for *n*-type GaN, AlN, and InN. For GaN the literature values range from 2.1 to 4.26 eV, for AlN from  $< 0$  to 2.16 eV, and the values of InN fluctuate between 4.6 and 5.8 eV. Thus, deviations of more than 50% can be found. Therefore a general definition of the electron affinity is provided in the first part of this chapter, followed by a detailed survey and critical analysis of the methodologies used to derive the different electron affinity values of GaN, AlN, and InN presented in Tab. 5.1. Finally the influence of the electron affinity on the tunnel current is discussed in detail. Based on this, an estimation of the electron affinity is derived from fits of the simulated tunnel current to the measured  $I(V)$  spectra of  $\text{Al}_{1-x}\text{In}_x\text{N}$ .

$\chi_{\text{GaN}}$ [eV]	$\chi_{\text{AlN}}$ [eV]	$\chi_{\text{InN}}$ [eV]
2.1 – 4.1[130] <sup>a</sup>	< 0[131] <sup>a</sup>	5.7[132] <sup>d</sup>
4.16 – 4.26[133] <sup>b</sup>	0.6 ± 0.3[134] <sup>a</sup>	5.8[135] <sup>d</sup>
2.7 ± 0.3[134] <sup>a</sup>	2.16 ± 0.3[136] <sup>a</sup>	5.5[137] <sup>e</sup>
4.02 – 4.10[138] <sup>b</sup>	1.9 ± 0.2[139] <sup>a</sup>	≤ 4.7[140] <sup>f</sup>
3.2 ± 0.2[141] <sup>a</sup>	~ 1.9[142] <sup>a</sup>	4.7 (4.6)[143] <sup>a</sup>
3.5 ± 0.1[144, 145] <sup>a</sup>	0.25 ± 0.3[146] <sup>a</sup>	
3.1 ± 0.2[146] <sup>a</sup>		
3.4 ± 0.1[147] <sup>c</sup>		
2.8 ± 0.1[148] <sup>a</sup>		
3.8 (3.3)[143] <sup>a</sup>		
3.18[149] <sup>g</sup>	1.01[149] <sup>g</sup>	

<sup>a</sup>UV-photoemission spectroscopy (UPS)

<sup>b</sup>*C-V* and *I-V* measurements on GaN Schottky barrier diodes

<sup>c</sup>deep-level optical spectroscopy (DLOS) + vacuum referred binding energy (VRBE)

<sup>d</sup>via Fermi level stabilization energy,  $E_{\text{FS}}$

<sup>e</sup>scanning photoelectron spectroscopy (PES)

<sup>f</sup>conductive AFM *I-V* characteristics

<sup>g</sup>DFT calculation

**Table 5.1:** Compilation of values for the electron affinity  $\chi$  in eV for *n*-type GaN, AlN, and InN found in recent literature. Experimental values (*a-f*) were obtained by various methods as indicated in the footnotes. Theoretical values (*g*), obtained by DFT calculations, are listed in the last row.

## 5.1 Definition of the electron affinity

The electron affinity  $\chi$  of a semiconductor is defined as the energy difference between the conduction band minimum and the vacuum energy at the surface  $\chi = E_{\text{vac}} - E_{\text{C}}$ , [150] or physically speaking, it is defined as the energy required to move an electron from the bottom of the conduction band at the surface of the semiconductor to the vacuum right outside the semiconductor. [151] The electron affinity is considered to be a material constant which, in contrast to the work function, does not depend on the doping of the semiconductor. However,  $\chi$  needs to be measured at the surface and is thus critically affected by surface conditions. It

depends on the exact atomic structure as well as on impurities and contaminations on the surface. Hence, it rather could be considered as a property of the surface.

## 5.2 Electron affinity of GaN

The first values of the electron affinity of GaN,  $\chi_{\text{GaN}}$ , were measured by Pankove *et al.* [130] in 1974 on degenerate *n*-type and semi-insulating GaN. Photoemission measurements on these GaN surfaces of unknown orientation, heat-cleaned by electron bombardment, revealed a lower and upper limit ( $4.1 > \chi_{\text{GaN}} > 2.1$  eV) for the electron affinity. In 1996 Bermudez *et al.* [134] investigated GaN(0001) – (1 × 1) surfaces, cleaned in UHV by Ga deposition and subsequent annealing. The electron affinity was derived from photoemission spectroscopy (UPS) measurements to be  $\chi_{\text{GaN}} = 2.7 \pm 0.3$  eV by evaluating the equation

$$\chi = h\nu - W - E_g, \quad (5.1)$$

with  $E_g$  being the band gap of the semiconductor,  $h\nu$  being the photon energy and  $W$  being the energy difference between the energy onset of photoemission and the valence band maximum (VBM). Later in the same year, this value was revised to  $\chi_{\text{GaN}} = 3.2 \pm 0.2$  eV after surface states near the band edges, formed by the Ga adlayer on GaN(0001) surfaces cleaned by N sputtering and annealing, were removed by O absorption.[141] In the UPS spectrum, the oxygen adsorption shifts the measured VBM to higher binding energies. Thus,  $W$  is reduced in Eq. 5.1.

A similar value of  $\chi_{\text{GaN}} = 3.5 \pm 0.1$  eV was found by Wu *et al.* [144, 145] in 1998 using UPS, also on reconstructed GaN(0001) – (1 × 1) surfaces, cleaned by nitrogen sputtering and annealing in UHV. With the same method Grabowski *et al.* [146] found a slightly lower value of  $\chi_{\text{GaN}} = 3.1 \pm 0.2$  eV on cleaned (0001) surfaces in 2001. Two years later, in 2003, again a lower value of  $\chi_{\text{GaN}} = 2.8 \pm 0.2$  eV was determined by Tracy *et al.* [148] with UPS on GaN(0001) surfaces. Their samples were cleaned by chemical vapor cleaning (CVC), which involved annealing in ammonia. Afterwards indication for a stoichiometric surface was found in x-ray photoelectron spectroscopy (XPS) measurements. Nevertheless, an absorption of the polar ammonia molecules, leading to a surface dipole layer, was considered as

an explanation for the low value of  $\chi$ . In 2012 Lin *et al.* [143] found electron affinities of 3.8 eV and 3.3 eV with UPS on annealed, unreconstructed and stoichiometric GaN(0001) (Ga-polar) and GaN(000 $\bar{1}$ ) (N-polar) surfaces, respectively. To remove the Ga adlayer, the (000 $\bar{1}$ ) surface was treated with HCl beforehand. Due to the small (unintentional) doping of the investigated samples, the low carrier concentration may be too small to completely screen spontaneous polarization fields at the surface. The large difference in the electron affinity measured for the two surfaces, was related to the different polarization at the opposite polar surfaces.

Another method to determine the electron affinity of GaN, is to investigate GaN diodes with Au, Cr, or Ni as Schottky barrier contact and Al as ohmic contact by current-voltage and capacitance measurements. Then  $\chi_{\text{GaN}}$  can be calculated as the difference between the work function of the metal (Au, Cr, Ni) and the barrier height obtained from  $I$ - $V$  and  $C$ - $V$  measurements. If surface state-induced charges at the junction, metal induced gap states, and chemical reactions at the interface are neglected,[133] values of  $\chi_{\text{GaN}} = 4.26$  eV and  $4.06 - 4.07$  eV were obtained by this method from  $I$ - $V$  measurements by Hacke *et al.* [133] in 1993 and Kalinina *et al.* [138] in 1996, respectively.  $C$ - $V$  measurements yielded  $\chi_{\text{GaN}} = 4.16$  eV and  $4.02 - 4.10$  eV, respectively, if the barrier height is assumed to be independent of the electric field in the junction.[133] Hacke *et al.* used Au contacts, while Kalinina *et al.* obtained similar results by investigating diodes with Au, Cr, and Ni contacts as Schottky barrier.

The electron affinity of  $n$ -type GaN [Mn:  $2 \times 10^{16} \text{ cm}^{-3}$ ] was obtained by Korotkov *et al.* [147] using the vacuum referred binding energy (VRBE) model. First the Mn acceptor level  $E_A$  with respect to the valence band edge was determined with absorption measurements in combination with deep-level optical spectroscopy (DLOS). Afterwards the electron affinity was derived to be 3.4 eV by using the relation  $\chi_{\text{GaN}} = E_{\text{VRBE}} + E_A - E_g$ , with  $E_{\text{VRBE}}$  being the theoretically derived vacuum referred binding energy.

Another purely theoretical value of the electron affinity of GaN was given by Moses *et al.* in 2011.[149] For non-polar, relaxed surfaces they obtained  $\chi_{\text{GaN}} = 3.18$  eV using density functional theory (DFT) with the Heyd-Scuseria-Ernzerhof XC functional.

### 5.3 Electron affinity of AlN

The electron affinity of AlN,  $\chi_{\text{AlN}}$ , was solely determined on reconstructed AlN(0001)  $-(1 \times 1)$  surfaces. In 1996 Bermudez *et al.* [134] investigated thin AlN films grown on GaN(0001)  $-(1 \times 1)$  surfaces by UPS using Eq. 5.1. An electron affinity of  $\chi_{\text{AlN}} = 0.6 \pm 0.3 \text{ eV}$  was found, questioning prior suggestions of a negative electron affinity (NEA) being an intrinsic property of AlN.[131] In 1998, with the same technique, Wu *et al.* [136] found a significantly higher value of  $\chi_{\text{AlN}} = 2.16 \pm 0.3 \text{ eV}$  on the AlN(0001)  $-(1 \times 1)$  surface. Later, in 1999, under consideration of an Al termination of the AlN(0001)  $-(1 \times 1)$  surface, the same group determined  $\chi_{\text{AlN}}$  to be  $1.9 \pm 0.2 \text{ eV}$ .[139] In analogy to GaN [141] it was assumed that the Al dangling bonds induce surface states near the valence band, altering the determination of the VBM. Here, bulk sensitive UPS (higher photon energies) was used instead of O deposition on the surface in combination with surface sensitive UPS. However, adsorption of O lead to the same result for  $\chi_{\text{AlN}}$ . On this account, in 2001, Bermudez revised his result of  $\chi_{\text{AlN}} = 0.6 \pm 0.3 \text{ eV}$  and, together with Wu and Kahn, published a recommendation to use  $1.9 \pm 0.2 \text{ eV}$  as a reliable value for  $\chi_{\text{AlN}}$ .[142] Grabowski *et al.* [146] found a much lower value of  $\chi_{\text{AlN}} = 0.25 \pm 0.3 \text{ eV}$  in 2001, also measured with UPS. As reason for the discrepancy to earlier values, Grabowski suggested that the lower  $\chi_{\text{AlN}}$  is due to the cleaner surface without O contamination. However, such surfaces typically exhibit Al adlayers, whose surface states alter the UPS spectrum and lower the measured electron affinity.

Moses *et al.* derived a theoretical value of the electron affinity in 2011 in analogy to GaN. With DFT calculations of non-polar, relaxed surfaces they obtained  $\chi_{\text{AlN}} = 1.01 \text{ eV}$ .[149]

### 5.4 Electron affinity of InN

In order to determine the electron affinity of InN different techniques were applied. Wu *et al.* [132, 152] and Li *et al.* [135] both reported an electron affinity of InN determined via the Fermi level stabilization energy ( $E_{\text{FS}}$ ), arising from irradiation induced defects. In semiconductors  $E_{\text{FS}}$  "defines the average dangling bond energy

with respect to band edges".[152] It was assumed to be located at a constant energy of 4.9 eV below the vacuum level for all III-V semiconductors, which was determined by applying the amphoteric defect model.[153, 154] Using the band offsets between InN and GaN,[155] the band edges of InN were determined relative to  $E_{\text{FS}}$  and thus to the vacuum level, yielding  $\chi_{\text{InN}} \sim 5.7$  eV.

In 2008 a value of  $\chi_{\text{InN}} = 5.5$  eV was estimated from cross-sectional scanning photoelectron microscopy and spectroscopy (SPEM/S) on the  $(\bar{1}\bar{1}20)$  surface of InN by Wu *et al.*[137] An undoped InN/GaN/AlN heterostructure was cleaved in situ to obtain a clean non-polar  $a$ -plane. PES was measured on GaN and InN and the valence-band maxima were identified. The valence band offset between the materials was determined, followed by the calculation of the conduction band offset  $\Delta E_{\text{C}}$  under consideration of the band gaps. Afterwards the electron affinity of InN was estimated by  $\chi_{\text{InN}} = \chi_{\text{GaN}} + \Delta E_{\text{C}}$ , assuming  $\chi_{\text{GaN}} = 3.5$  eV.

In 2011 Spyropoulos-Antonakakis *et al.* [140] proposed an upper limit for the electron affinity of  $c$ -plane InN of  $\chi_{\text{InN}} < 4.7$  eV. InN nanocrystals were investigated with conductive AFM using a Pt/Ir coated tip in contact mode. Assuming the formation of a Schottky barrier between InN and the Pt/Ir tip,  $I$ - $V$  characteristics were used to calculate the Schottky barrier height (SBH). Then, the SBH as a function of metal, semiconductor, and metal-semiconductor interface characteristics suggests an electron affinity below 4.7 eV.

Finally, the electron affinity of polar InN(0001) (In-polar) and InN(000 $\bar{1}$ ) (N-polar) was measured in 2012 with UPS by Lin *et al.* [143] to be  $\chi_{\text{InN}} = 4.7$  eV and 4.6 eV, respectively. Beforehand the samples were cleaned by *ex-situ* HCl and KOH wet etching and subsequent *in-situ* annealing, leading to unreconstructed and stoichiometric surfaces.[156] In contrast to GaN the difference between both values for  $\chi_{\text{InN}}$  measured on the (0001) and on the (000 $\bar{1}$ ) surface is low. This was explained by the high electron concentration in unintentionally doped samples, effectively screening spontaneous polarization fields at the polar surface.

## 5.5 Discussion

The variety of experimentally obtained values for the electron affinity has different reasons: Since  $\chi$  can be measured at the surface of a semiconductor, only, the results are particularly sensitive to surface conditions. First, cleaning the samples from contamination is difficult. Additionally not all measurements were performed in UHV making any cleaning meaningless after a short time.[140] Usually even in UHV the surfaces are not stoichiometric, because of annealing, decomposition, or adsorption. Only cleaved  $m$  or  $a$  surfaces are stoichiometric, while the (0001) and (000 $\bar{1}$ ) surface require an elaborate cleaning process to become nearly stoichiometric.[143, 145, 148, 156]

Most values were obtained on reconstructed (0001) – (1 × 1) surfaces where Ga, Al, or In adlayers were observed on the surfaces.[157] Calculations confirmed the stability of those adatoms reconstructions.[54, 158] They induce electronic states extending into the band gap.[54, 128, 158, 159] It was demonstrated that these surface states can influence surface sensitive measurement techniques that rely on the determination of band edges [134, 139, 142] and thus, alter the obtained electron affinity. Native contamination by oxides or carbon can lead to similar effects.[144, 160] On uncleaned AlN surfaces impurity atoms even can lead to the measurement of a negative electron affinity.[131] It was shown that a lowering of  $\chi$ , in the case of AlN down to negative electron affinities, can be deliberately induced by Cs deposition onto the surface.[130, 161]

Second, (0001) and (000 $\bar{1}$ ) surfaces, where most values were obtained, are polar surfaces that exhibit spontaneous polarization fields. Both surfaces present significant differences.[162] Depending on the carrier concentration the polarization fields are screened at the surface, leading to different degrees of influence on the electron affinity. It was shown that values obtained on (0001) and (000 $\bar{1}$ ) surfaces can deviate up to 0.5 eV. Only one value of  $\chi$  was measured on a non-polar InN( $\bar{1}\bar{1}20$ ) cleavage plane.[137] However, the stated  $\chi_{\text{InN}}$  was derived relative to  $\chi_{\text{GaN}}$ , yet obtained on the polar  $c$ -plane.

The theoretically derived electron affinities,[149] are similar to the measured values. However, a comparison can only be drawn with reservations, since the majority

of measurements was carried out on polar surfaces while only non-polar, relaxed surfaces are computed. According to DFT calculations the difference in the electron affinity between the  $m$ - and  $a$ -plane is less than 0.1 eV. However, no specification was given about the difference in  $\chi$  between non-polar ( $m$ - and  $a$ -planes) and the polar ( $c$ -plane) surfaces. Furthermore it is well known that theory provides rather strongly shifted empty states. Hence, the theoretically obtained  $\chi$  values need to be taken with caution.

The difficulties of the measurement of the electron affinity on  $c$ -planes are profound and include contaminated and/or reconstructed non-stoichiometric surfaces with surface states inside the gap as well as polarization fields at the surface. In combination with the lack of measurements on clean, non-polar stoichiometric surfaces, where no surface states or only the empty ones are present within the band gap, it becomes evident that a bulk-like  $\chi$  is hardly identifiable. In view of this situation the electron affinity of group III-nitride semiconductors needs to be reassessed.

## 5.6 Influence of the electron affinity on the tunnel current

In order to understand the influence of  $\chi$  on the tunnel current, the equations needed for the calculation of the electrostatic potential and the tunnel current in Chap. 2.2 are recalled. According to these equations,  $\chi$  critically affects both, electrostatic and tunnel current calculations. On the one hand,  $\chi$  influences the contact potential  $\Delta\phi = E_F - E_C - \chi + \Phi_t$  needed for the calculation of the electrostatic potential (cf. Eq. 2.32). On the other hand, when calculating the tunnel current,  $\chi$  determines the height of the vacuum barrier and hence influences the transmission coefficient (cf. Eq. 2.36).

In order to quantify the influence of  $\chi$  on the tunnel spectra, tunnel current simulations of  $n$ -type GaN are performed using a lower and upper limit of  $\chi = 2.1$  eV and 4.1 eV, respectively, according to the values obtained by Pankove *et al.* [130]. The resulting spectra are shown in Fig. 5.1(a) as black ( $\chi = 2.1$  eV) and blue ( $\chi = 4.1$  eV)

curves. Both spectra were simulated using a tip work function of  $\Phi_t = 4.0 \text{ eV}$ . Although the electron affinity is the only difference between the two simulated tunnel spectra, they differ tremendously. The onset voltages at both, positive and negative voltages, move to smaller voltages with increasing  $\chi$ . At higher voltages the two spectra intersect. From that point on the tunnel current is significantly larger for a smaller  $\chi$ .

Without an external voltage and for  $\chi = 2.1 \text{ eV}$ , the contact potential  $\Delta\phi$  is approximately  $1.9 \text{ eV}$ . Thus, the tip induces a large upward band bending. In contrast, for  $\chi = 4.1 \text{ eV}$ , the contact potential is approximately  $-0.1 \text{ eV}$  and thus, a small downward band bending is present. At negative sample voltages ( $V < 0$ ) an accumulation current occurs if the conduction band bends below the Fermi energy (cf. Chap. 2.2.3). For the case of  $\chi = 2.1 \text{ eV}$  the larger contact potential results in an onset voltage of the accumulation current at larger negative voltages. At positive voltages ( $V > 0$ ) the band bending and thus the onset voltage is mainly determined by the surface state of GaN.[124] Thus, in the special case of GaN, the onset voltage of the conduction band current  $I_C$  (cf. Chap. 4) is nearly independent of the electron affinity.

The height of the tunnel barrier decreases with a smaller electron affinity. This is exemplarily illustrated in Fig. 5.1(b) and (c), where the band diagrams and tunnel barriers for  $\chi = 4.1 \text{ eV}$  and  $\chi = 2.1 \text{ eV}$  are shown for a sample voltage of  $-3.0 \text{ V}$ . As a result of the smaller tunnel barrier, the slope of the tunnel spectra in Fig. 5.1(a) is steeper for  $\chi = 2.1 \text{ eV}$  than for  $4.1 \text{ eV}$ .

For the contact potential and the shape of the tunnel barrier the work function of the tip is as important as the electron affinity. Figure 5.1(d) shows the band diagram for an electron affinity of  $\chi = 2.1 \text{ eV}$  and a tip work function of  $\Phi_t = 2.0 \text{ eV}$ . The corresponding tunnel spectrum is shown in red in Fig. 5.1(a). The contact potential in this case is identical to the one in Fig. 5.1(b). The onset voltages of both tunnel spectra are thus equal. However, since the height of the tunnel barrier is lower than in Fig. 5.1(b) and even lower than in Fig. 5.1(c), the slope of the corresponding tunnel spectrum is considerably larger and the tunnel current increases by several orders of magnitude.

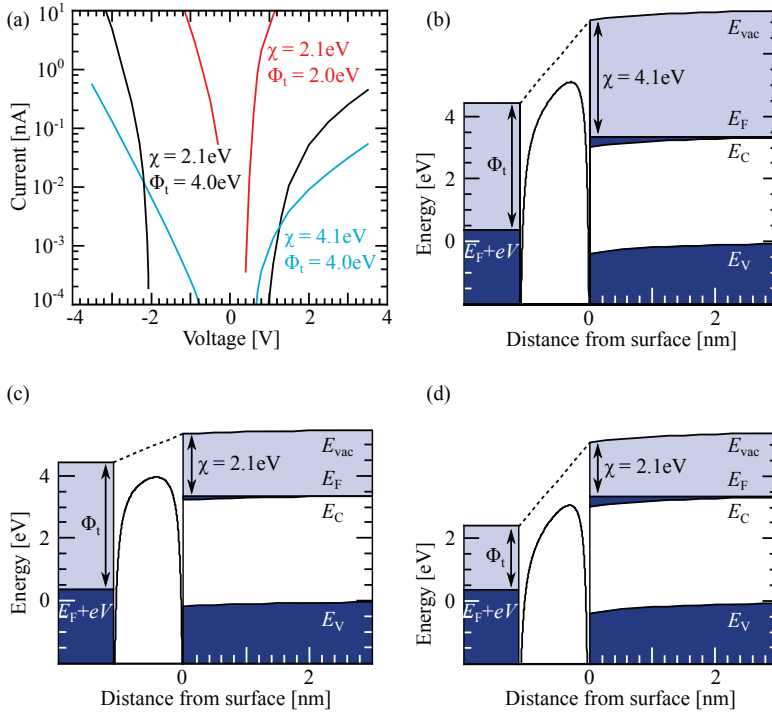


**Figure 5.1:** (a) Simulation of the tunnel current of GaN. The spectra were simulated with the lower and upper limit of the electron affinity given by Pankove *et al.*[130]: 2.1 eV (black and red) and 4.1 eV (blue), respectively. The red curve shows the tunnel current if in addition the tip workfunction is lowered from 4.0 to 2.0 eV. All other parameters remain constant. (b)-(c) Band diagrams at  $-3.0 \text{ V}$  for (b)  $\chi = 4.1 \text{ eV}$ ,  $\Phi_t = 4.0 \text{ eV}$ , (c)  $\chi = 2.1 \text{ eV}$ ,  $\Phi_t = 4.0 \text{ eV}$ , and (d)  $\chi = 2.1 \text{ eV}$ ,  $\Phi_t = 2.0 \text{ eV}$ . With a negative voltage applied, the bands are dragged down and an accumulation current occurs if the conduction band bends below the Fermi energy (cf. Chap. 2.2.3). Since in (c), because of the large contact potential, first the tip-induced upward band bending has to be compensated, the tunnel current has a much higher onset than in (b). However, because of the lower tunneling barrier in (c), the tunnel probability of electrons tunneling from the accumulation zone into the tip is higher. The contact potential in (d) is identical to the one in (b). Since the height of the tunneling barrier is clearly lower than in (b) and even lower than in (c), the slope of the corresponding tunnel spectrum is considerably larger.

## 5.7 Estimation of the electron affinity of $\text{Al}_{0.81}\text{In}_{0.19}\text{N}$ using STS

Since nothing is known about the composition dependence of the electron affinity of  $\text{Al}_{1-x}\text{In}_x\text{N}$ , in a first approximation a linear change between the electron affinities of AlN and InN is assumed. However, the large range of values of the electron affinity of AlN and InN, listed in Tab. 5.1, impede the derivation of the electron affinity  $\chi_{\text{AlInN}}$  of  $\text{Al}_{1-x}\text{In}_x\text{N}$ . For instance, a linear interpolation of  $\chi_{\text{AlInN}}$  with an In content of 19%, leads to values between 1.08 eV and 2.85 eV.

In order to fit the simulated to the experimentally obtained tunnel spectra, measured on the  $\text{Al}_{1-x}\text{In}_x\text{N}$  layers of samples A2314, A2688, and A3162, even larger values of  $\chi_{\text{AlInN}}$  ranging from 3.3 eV to 4.1 eV were required, assuming a work function of the W tip of 4.0 eV. Two simulated spectra fitted to the experimentally obtained ones are exemplarily shown in Fig. 5.2. The experimentally obtained spectra represented by black and red symbols were measured on samples A3162 (set point:  $V = -3.6$  V,  $A = 150$  pA) and A2688 ( $V = -3.0$  V,  $A = 100$  pA), respectively. The simulated tunnel currents for electron affinities of 4.1 eV and 3.3 eV are shown as green and blue lines, respectively. Note, besides the electron affinity, the In-derived surface state was used as additional fit parameter (cf. Chap. 4) as well as the tip-sample separation, due to the different set points during acquisition of the spectra. All other parameters, including the work function of the tip were kept constant.

Simulated spectra were fitted to every experimentally obtained tunnel spectrum in the same manner. The average value of the electron affinity needed for the best fits is  $\chi_{\text{AlInN}} = 3.5 \pm 0.1$  eV.

The electron affinity determined in this experiment does not match the values obtained by linear interpolation of the previously reported electron affinities of AlN and InN (cf. Tab. 5.1). This discrepancy suggests that the electron affinity without deviations from stoichiometry, metallic adlayers, or detrimental surface states in the band gap, is larger than the previously found values on polar surfaces. A clear conclusion requires, however, a critical reassessment of the electron affinity. In particular the determination of its composition dependence is necessary, since a linear dependence may be inaccurate.

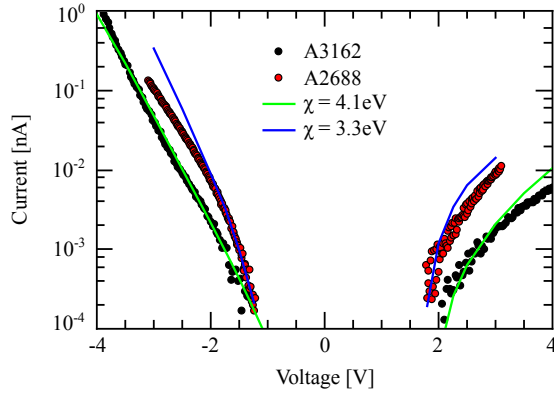


**Figure 5.2:** Examples of fitted spectra for the highest and lowest value of  $\chi_{\text{AlInN}}$ . The spectra represented by black and red symbols are measured on samples A3162 (measured at  $V = -3.6$  V and  $A = 150$  pA) and A2688 (measured at  $V = -3.0$  V and  $A = 100$  pA), respectively. The curves were fitted with electron affinities of 4.1 eV and 3.3 eV, depicted by green and blue lines, respectively. The tip-sample separation of the fitted spectra is different.

## 5.8 Conclusion

For the simulation of tunnel spectra of  $\text{Al}_{1-x}\text{In}_x\text{N}$  an accurate knowledge of its electron affinity is required. The composition dependent electron affinity  $\chi$  of ternary compound semiconductors usually is obtained by linear interpolation between the binaries. However, a literature survey reveals that for  $\chi_{\text{AlN}}$  and  $\chi_{\text{InN}}$  a broad range of values was reported. These values were mostly obtained experimentally on contaminated and/or non-stoichiometric polar surfaces, and hence are difficult to assess.

In order to fit simulated tunnel spectra to experimentally obtained ones (acquired on non-polar  $(10\bar{1}0)$  surfaces), an average value of  $\chi_{\text{AlInN}} = 3.5 \pm 0.1$  eV was needed. This value of the electron affinity is larger than the value obtained by linear interpolation of the binary electron affinities reported in literature. On the one hand this discrepancy indicates that the electron affinity on contamination free and stoichiometric surfaces may be larger than on polar surfaces. On the other hand the assumption of a linear dependence of the electron affinity on the composition may be inaccurate. However, in order to validate these assumptions, a determination of the composition dependence of the electron affinities is necessary.

# Chapter 6

## Strain and compositional fluctuations in $\text{Al}_{0.81}\text{In}_{0.19}\text{N}/\text{GaN}$ heterostructures

*Text and images in this Chapter are partially adapted from [P2] (cf. list of own publications, p. 137).*

In this chapter strain and compositional fluctuations of nominally lattice-matched  $\text{Al}_{0.81}\text{In}_{0.19}\text{N}/\text{GaN}$  heterostructures are investigated by cross-sectional scanning tunneling microscopy (STM) and selected area electron diffraction (SAED) measurements using scanning transmission electron microscopy (STEM). To begin with, in Sec. 6.1 (10 $\bar{1}$ 0) cleavage surfaces are investigated by STM. The roughness of the surface of a lattice-matched sample is investigated by calculating the power-spectral density (PSD), the auto-covariance (ACF), and the cross-covariance (CCF) functions. The presence of strain induces height modulations governed by three roughness components at the cleavage surface. A subsequent analysis of SAED patterns in Sec. 6.2 indicates changes in the  $c$  and  $a$  lattice constants and hence strain is present in  $a$  and  $c$  direction. The surface height modulations are compatible with a relaxation of alternatingly compressive and tensile strained domains, indicating compositional fluctuations. Changes of the  $a$  lattice constant are traced to interface misfit edge dislocations. The misfit dislocations induce steps increasing the roughness within the  $\text{Al}_{0.81}\text{In}_{0.19}\text{N}$  layers.

## 6.1 Investigation of $\text{Al}_{0.81}\text{In}_{0.19}\text{N}$ layers by STM

### 6.1.1 Cleavage surfaces of $\text{GaN}/\text{Al}_{0.81}\text{In}_{0.19}\text{N}$ heterostructures

Cleaving the samples in ultrahigh vacuum as described in Chap. 3.1.1 exposes clean  $(10\bar{1}0)$  surfaces, providing a cross-sectional view of the complete heterostructure. However, flat cleavage surfaces were obtained only for samples with  $\text{Al}_{1-x}\text{In}_x\text{N}$  layers grown nearly lattice-matched to GaN, i.e. for samples with an In content around 19%. For lower In contents ( $\sim 15\%$ ) the surfaces were found to be extremely rough with elevations of several hundred nm. Those surface presented a high step density and a large convex curvature in the region of the  $\text{Al}_{0.85}\text{In}_{0.15}\text{N}$  layers. In consequence, the  $\text{Al}_{0.85}\text{In}_{0.15}\text{N}$  layers could not be observed in STM measurements.

Nearly lattice-matched samples on the other hand exhibit flat cleavage surfaces with a low step density. An example is presented in Fig. 6.1(a), where a large scale STM image of the  $(10\bar{1}0)$  cleavage surface of sample A3162 is shown. The scan area has a size of  $(2.5 \times 15.7) \mu\text{m}^2$  and includes, from left to right, the GaN substrate, the GaN buffer layer, the five pairs of  $\text{Al}_{0.81}\text{In}_{0.19}\text{N}/\text{GaN}$  layers, and the GaN capping layer. The interfaces are indicated by dashed lines in the magnification shown in Fig. 6.1(b). The  $\text{Al}_{0.81}\text{In}_{0.19}\text{N}$  layers appear brighter than the surrounding GaN. This contrast is further discussed in Chap. 8. On the otherwise flat surface broad height modulations are present, giving rise to dark and bright stripes extending diagonally through the complete heterostructure (indicated by the white arrows in Fig. 6.1(a)). At larger magnifications additional contrast fluctuations on a smaller length scale are discernable in the  $\text{Al}_{0.81}\text{In}_{0.19}\text{N}$  layers.

### 6.1.2 Height profiles of $\text{GaN}/\text{Al}_{0.81}\text{In}_{0.19}\text{N}$ heterostructures

In order to quantify the different contributions to the contrast fluctuations, first the STM images were rectified according to Ref. [163], to remove the non-linear distortions present especially at large scan ranges. Second height profiles with a length of  $14 \mu\text{m}$  are measured parallel to the  $\text{Al}_{0.81}\text{In}_{0.19}\text{N}$  layers along the  $[1\bar{2}10]$  direction

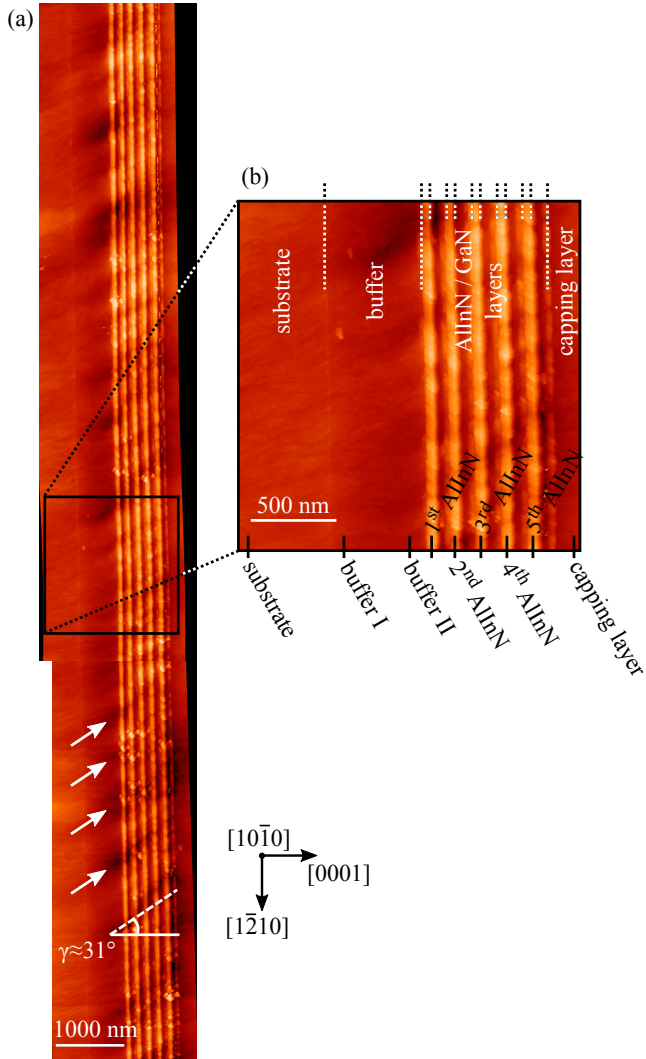


**Figure 6.1:** (a) Cross-sectional STM overview image of the  $\text{Al}_{0.81}\text{In}_{0.19}\text{N}/\text{GaN}$  heterostructure measured at  $-4.0$  V and  $100$  pA. The  $\text{Al}_{0.81}\text{In}_{0.19}\text{N}$  layers appear brighter than the surrounding GaN. Note the presence of long range contrast fluctuations indicated by the white arrows and additional fluctuations at smaller scale within the  $\text{Al}_{0.81}\text{In}_{0.19}\text{N}$  layers. (b) Magnification of the area in the rectangle in (a). The complete epitaxial structure can be recognized from left to right: GaN substrate, GaN buffer layer,  $5 \times$  ( $31$  nm  $\text{Al}_{0.81}\text{In}_{0.19}\text{N}$  /  $105$  nm GaN), and GaN capping layer. The interfaces are indicated by dashed lines. The black dashes at the bottom indicate the spatial positions along the growth direction where a roughness analysis was performed. The image is adapted from [P2].

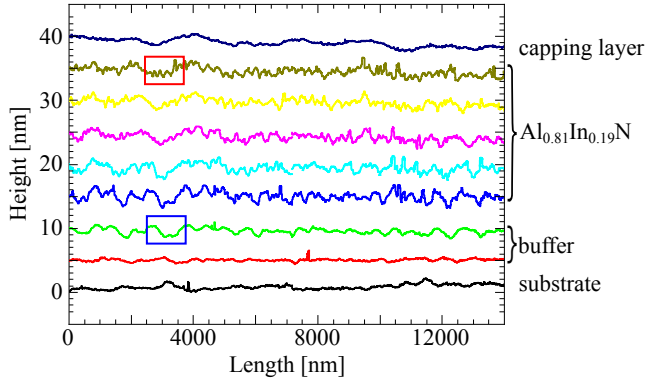


**Figure 6.2:** Height profiles measured along the  $[1\bar{2}10]$  direction within each layer. The profiles are offset for clarity. Two roughness features are visible in the profiles of the  $\text{Al}_{0.81}\text{In}_{0.19}\text{N}$  layers, small spikes (red box) and a broad modulation, that also appears in the buffer layer (blue box).

within each layer. The height profiles are extracted on the substrate, the buffer layer near the substrate (buffer I position), the buffer layer near the first  $\text{Al}_{0.81}\text{In}_{0.19}\text{N}$  layer (buffer II position), all five  $\text{Al}_{0.81}\text{In}_{0.19}\text{N}$  layers, and on the capping layer at the spatial positions marked by black dashes at the bottom of Fig. 6.1(b). The profiles are presented in Fig. 6.2 (offset against each other for clarity). The substrate (black) and the buffer layer near the substrate (red) are almost flat and exhibit few and irregularly distributed elevations, only, with root mean square (rms) roughnesses of  $R = 0.36 \pm 0.05$  nm and  $0.20 \pm 0.01$  nm, respectively. However, in the buffer layer close to the first  $\text{Al}_{0.81}\text{In}_{0.19}\text{N}$  layer (green,  $R = 0.43 \pm 0.07$  nm), a broad height modulation (marked by the blue rectangle in Fig. 6.2) appears. It corresponds to the broad dark and bright stripes highlighted by white arrows in Fig. 6.1(a). The profiles extracted on the five  $\text{Al}_{0.81}\text{In}_{0.19}\text{N}$  layers exhibit an average roughness of  $0.56 \pm 0.05$  nm and show the same broad modulations, especially pronounced in the first  $\text{Al}_{0.81}\text{In}_{0.19}\text{N}$  layer (blue profile). Additionally smaller contrast fluctuations are superimposed on the broad height modulations in the  $\text{Al}_{0.81}\text{In}_{0.19}\text{N}$  layers, marked by the red rectangle in Fig. 6.2. In the capping layer (dark blue) only a broad modulation with a lower spatial frequency is detected, causing a roughness of  $\sim 0.49$  nm.

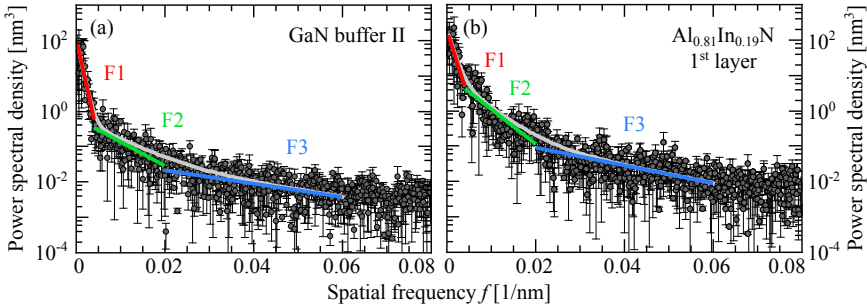


**Figure 6.3:** Power spectral density vs. spatial frequency  $f$  calculated from height profiles measured within (a) the buffer layer close to  $\text{Al}_{0.81}\text{In}_{0.19}\text{N}$  and (b) within the first  $\text{Al}_{0.81}\text{In}_{0.19}\text{N}$  layer. The gray curves are fits to the experimental data assuming three different exponential decays with different intensities and correlation lengths. The three exponential decays correspond in real space to three types of features discussed in the text. The red, green and blue colored lines show the individual decays and indicate the respective spatial frequency ranges. (b) is adapted from [P2].

### 6.1.3 Roughness analysis

In order to separate the different roughness contributions a detailed roughness analysis of the height profiles is performed for each layer.

#### Power-spectral density

First of all, the power-spectral density (PSD) of each profile is calculated as described in Sec. 2.7.1. From the PSD the correlation lengths  $c_L$  and the roughnesses  $R$  are derived.

Two examples of the PSD spectra, extracted from the height profiles at the buffer II position and the first  $\text{Al}_{0.81}\text{In}_{0.19}\text{N}$  layer, are presented in Fig. 6.3(a) and (b), respectively. The spectra are shown in logarithmic scale as a function of the spatial frequency  $f$ . No peaks are detected in the PSDs, thus, the roughness does not exhibit periodic features. The PSDs of all layers exhibit three regions with a roughly exponential decay (linear in logarithmic scale) with different slopes as is indicated by the colored lines: from  $0.0 \text{ nm}^{-1}$  to  $0.004 \text{ nm}^{-1}$  (red), from  $0.004 \text{ nm}^{-1}$

to  $0.02 \text{ nm}^{-1}$  (green), and from  $0.02 \text{ nm}^{-1}$  to  $0.06 \text{ nm}^{-1}$  (blue). At spatial frequencies larger than  $0.06 \text{ nm}^{-1}$  almost constant PSD values occur (white noise). Hence, each PSD can be best described by the sum of three exponential decays shown as gray line.

Each exponential decay corresponds in real space to a Lorentzian shaped roughness component, with its specific correlation length  $c_L$  and rms roughness  $R^2$ . It should be recalled that  $c_L$  is a measure of the extend of surface features and  $R$  describes their intensity.  $c_L$  and  $R$  are given by the half width at half maximum and by the maximum of the Lorentzian function, respectively. Hence, by fitting the sum of three exponential decays to the PSD of every layer, the roughness  $R$  and correlation length  $c_L$  are derived for the three frequency ranges with the equations defined in Sec. 2.7.1. The resulting values are presented in Fig. 6.4 using the same line colors as in Fig. 6.3.

The central result is that the rms roughnesses of all three roughness components are significantly larger within the  $\text{Al}_{0.81}\text{In}_{0.19}\text{N}$  layers compared to the surrounding GaN. The feature labeled F1 has the largest correlation length. This component extends also into the buffer and the capping layer, indicated by a significantly higher roughness at the buffer II position and in the capping layer compared to the substrate and the buffer I position. The correlation lengths  $c_{L,F1}$  are  $133 \pm 11 \text{ nm}$  in the  $\text{Al}_{0.81}\text{In}_{0.19}\text{N}$  layers and between 100 and 250 nm in the surrounding GaN. This component is directly visible in the STM images as broad height modulations marked by white arrows in Fig. 6.1(a). Note, the large correlation length with only small rms roughness measured on the substrate is indicative of the typical cleavage surface of unstrained GaN. This effect is not connected to the  $\text{Al}_{0.81}\text{In}_{0.19}\text{N}$  layers.

The other two components labeled F2 and F3 are again more intense on the  $\text{Al}_{0.81}\text{In}_{0.19}\text{N}$  layers. The average correlation lengths of the  $\text{Al}_{0.81}\text{In}_{0.19}\text{N}$  layers are  $c_{L,F2} = 39.2 \pm 3.2 \text{ nm}$  and  $c_{L,F3} = 10 \pm 1.1 \text{ nm}$ , respectively. They can be discerned in the STM images as the small contrast features in each  $\text{Al}_{0.81}\text{In}_{0.19}\text{N}$  layer.

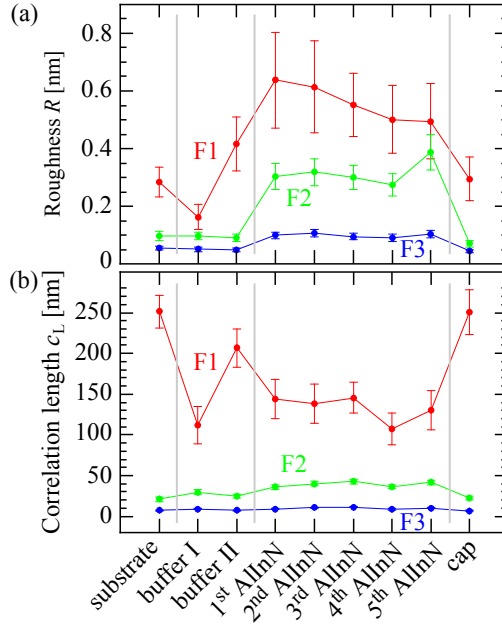


**Figure 6.4:** (a) Roughness  $R$  and (b) correlation length  $c_L$  extracted from the power spectral densities of the different layers shown according to the growth sequence (horizontal axis) within the  $\text{GaN}/\text{Al}_{0.81}\text{In}_{0.19}\text{N}$  heterostructure. The three different components of the roughness are labeled F1 (red), F2 (green), and F3 (blue). The image is adapted from [P2].

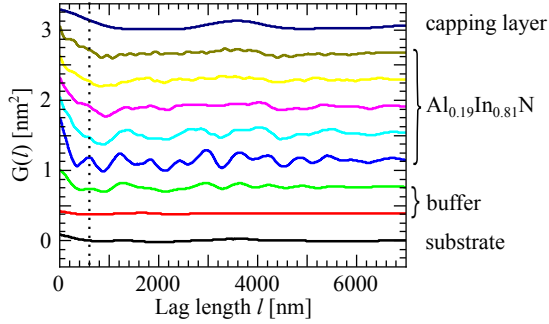


**Figure 6.5:** Auto-covariance functions of each height profile. The curves are offset for clarity. In the  $\text{Al}_{0.81}\text{In}_{0.19}\text{N}$  layers a correlation peak with a periodicity of approximately 600 nm (F1) is found (cf. dashed line). A weaker correlation peak appears repeatedly with a distance of approximately 225 nm (F2).

### Auto-correlation analysis

In order to quantify the average distance between the features the auto-covariance function (ACF) is derived from the height profiles according to the definition in Chap. 2.7.2. The resulting ACFs  $G(l)$  are presented in Fig. 6.5 as a function of the lag length  $l$  with the respective line colors of the height profiles (Fig. 6.2). For a better visibility, the curves are offset by  $0.4 \text{ nm}^2$ .

The ACFs of the substrate and the buffer I position are almost flat, indicating no relevant spatial correlation of the roughness. The capping layer shows one distinct correlation peak at a lag length of approximately 3750 nm, only.

The ACF of the  $\text{Al}_{0.81}\text{In}_{0.19}\text{N}$  layers and at the buffer II position exhibit several broad elevations. The first elevation is indicated by the dashed line in Fig. 6.5. This feature has a spatial periodicity of approximately 600 nm and can be associated with the F1 component of the roughness.

In the ACFs of the  $\text{Al}_{0.81}\text{In}_{0.19}\text{N}$  layers a second feature with a much smaller spatial frequency is present. It is visible particularly well in the fifth  $\text{Al}_{0.81}\text{In}_{0.19}\text{N}$  layer and exhibits a peak-to-peak distance of approximately 225 nm. This feature can be attributed to the F2 component. No information about the F3 component is visible in this analysis.

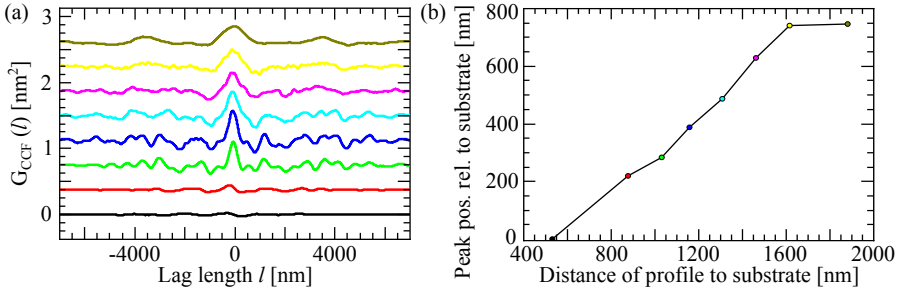


**Figure 6.6:** (a) Cross-covariance functions between line profiles of adjacent layers. The curves are offset for clarity. (b) Shift of the central peak of the CCF plotted against the distance of the measured profiles relative to the substrate. Black: substrate - buffer I, red: buffer I - buffer II, green: buffer II - 1st  $\text{Al}_{0.81}\text{In}_{0.19}\text{N}$ , blue: 1st  $\text{Al}_{0.81}\text{In}_{0.19}\text{N}$  - 2nd  $\text{Al}_{0.81}\text{In}_{0.19}\text{N}$ , light blue: 2nd  $\text{Al}_{0.81}\text{In}_{0.19}\text{N}$  - 3rd  $\text{Al}_{0.81}\text{In}_{0.19}\text{N}$ , magenta: 3rd  $\text{Al}_{0.81}\text{In}_{0.19}\text{N}$  - 4th  $\text{Al}_{0.81}\text{In}_{0.19}\text{N}$ , yellow: 4th  $\text{Al}_{0.81}\text{In}_{0.19}\text{N}$  - 5th  $\text{Al}_{0.81}\text{In}_{0.19}\text{N}$ , ochre: 5th  $\text{Al}_{0.81}\text{In}_{0.19}\text{N}$  - capping layer

### Cross-correlation analysis

In order to investigate the correlation of structural features between the layers, the cross-covariance functions (CCF) between height profiles of adjacent layers are derived according to the definition in Sec. 2.7.3. The CCFs are calculated between the profiles of substrate and buffer I position, buffer I and buffer II position, buffer II position and the first  $\text{Al}_{0.81}\text{In}_{0.19}\text{N}$  layer, as well as between all five  $\text{Al}_{0.81}\text{In}_{0.19}\text{N}$  layers and between the fifth  $\text{Al}_{0.81}\text{In}_{0.19}\text{N}$  layer and the capping layer. In this manner eight cross-correlation functions are obtained from the nine profiles. The resulting CCFs are presented in Fig. 6.6(a) as a function of the lag length  $l$ . The curves are offset for clarity.

Almost no correlation is visible between the substrate and the buffer (black). Within the buffer layer (red) a weak correlation is detectable. All other CCFs show a distinctive peak at negative lag lengths. The peak shifts from larger negative lag lengths of  $l \approx -220$  nm in the CCF between the buffer I and II position towards a lag length of almost zero for the correlation between the fifth  $\text{Al}_{0.81}\text{In}_{0.19}\text{N}$  and the capping layer. The shift of the central correlation peak can be attributed to the diagonal orientation of the broad height modulation through the entire heterostructure. In order to quantify the angle, the summed shift of the peak position

is plotted in Fig. 6.6(b) against the lateral distance of the respective profile relative to the substrate. A linear regression reveals a slope of  $0.61 \pm 0.05$  and hence an angle of  $(31.38 \pm 0.04)^\circ$ . For comparison the average angle between the dark stripes and the  $[0001]$  direction in Fig. 6.1 is found to be  $(31 \pm 4)^\circ$ . Furthermore this corroborated the attribution of the main feature in the correlation functions to the F1 roughness component.

The angle of  $\sim 31^\circ$  suggests, that the F1 feature is orientated along a semi-polar plane in the wurtzite structure. In the STM image of the  $(10\bar{1}0)$  surface only the projection of the semi-polar plane is visible, thus the exact plane cannot be determined.

A thorough inspection of the CCFs shows that smaller characteristics cannot be observed. Thus, the expansion of F2 and F3 in  $[0001]$  direction is restricted to one  $\text{Al}_{0.81}\text{In}_{0.19}\text{N}$  layer and does not extend through the intermediate GaN into adjacent  $\text{Al}_{0.81}\text{In}_{0.19}\text{N}$  layers.

## 6.2 Investigation of $\text{Al}_{0.81}\text{In}_{0.19}\text{N}$ by STEM and SAED

In order to obtain a deeper insight into the origin of the different roughness components, the  $\text{GaN}/\text{Al}_{0.81}\text{In}_{0.19}\text{N}$  heterostructure (A3162) is investigated by scanning transmission electron microscopy (STEM) using selected area electron diffraction (SAED). From SAED measurements the  $a$  and  $c$  lattice constants of  $\text{Al}_{0.81}\text{In}_{0.19}\text{N}$  and GaN is spatially resolved.

A cross-sectional STEM image of the  $\text{GaN}/\text{Al}_{0.81}\text{In}_{0.19}\text{N}$  heterostructure is shown in Fig. 6.7. The  $\text{Al}_{0.81}\text{In}_{0.19}\text{N}$  layers appear as dark horizontal lines that are straight and even. The upper half of the image shows the GaN capping layer, while the lower half shows the GaN buffer layer and the substrate. The dark dots below the first  $\text{Al}_{0.81}\text{In}_{0.19}\text{N}$  layer were caused by the electron beam and originally were not present in the sample.

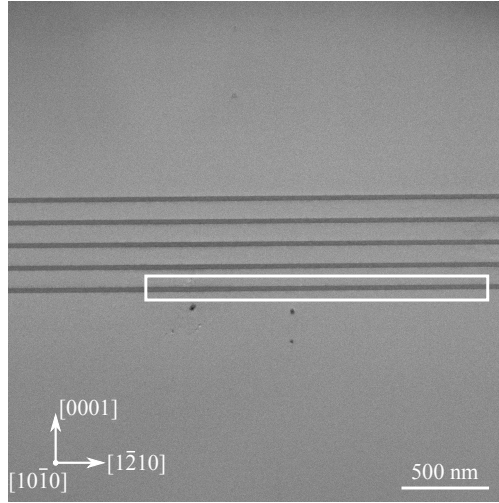


**Figure 6.7:** STEM image of the GaN/ $\text{Al}_{0.81}\text{In}_{0.19}\text{N}$  heterostructure. From bottom to top the image shows the GaN substrate and buffer layer, the five  $\text{Al}_{0.81}\text{In}_{0.19}\text{N}$  layers with the GaN interlayers and the GaN capping layer. The  $\text{Al}_{0.81}\text{In}_{0.19}\text{N}$  layers appear as dark horizontal lines.  $200 \times 15$  SAED patterns were measured in the area framed by a white rectangle.

In order to probe the spatial distribution of the lattice parameters in the GaN/ $\text{Al}_{0.81}\text{In}_{0.19}\text{N}$  heterostructure,  $200 \times 15$  SAED patterns are obtained in the area marked by the white box in Fig. 6.7. The diameter of the electron beam was set to approximately 10 nm.

Figure 6.8(a) and (b) illustrate two examples of such obtained electron diffraction patterns for GaN and  $\text{Al}_{0.81}\text{In}_{0.19}\text{N}$ , respectively. The diffraction patterns show the typical reflections of wurtzite structure along the  $[10\bar{1}0]$  zone axis. The peak separations along the reciprocal space direction  $[0002]$  and  $[1\bar{2}10]$ ,  $\Delta_c$  and  $\Delta_a$ , yield the inverse of the  $c$  and  $a$  lattice constants, respectively, as is described in Chap. 2.3.1. The well-known GaN  $c$  (518.6 pm) and  $a$  (518.6 pm) lattice constants,[164] are used to obtain a calibration factor for the conversion of  $\Delta_c$  and  $\Delta_a$  from pixels into lattice constant values.

Figure 6.9 presents the spatial distribution of the obtained local  $c$  and  $a$  lattice constants in the area covering the GaN buffer (bottom), the first  $\text{Al}_{0.81}\text{In}_{0.19}\text{N}$  layer

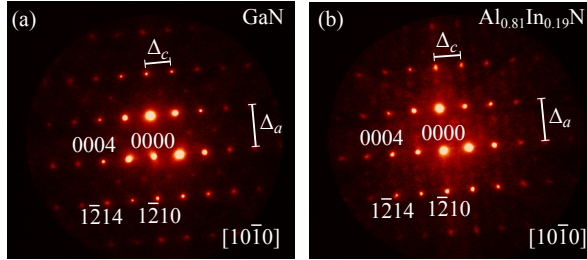


**Figure 6.8:** Examples of electron diffraction patterns along the  $[10\bar{1}0]$  zone axis acquired (a) on the first GaN interlayer and (b) on the first  $\text{Al}_{0.81}\text{In}_{0.19}\text{N}$  layer. The electron beam had a diameter of 10 nm. The peak separations along the reciprocal space direction  $[0002]$  and  $[1\bar{2}10]$ ,  $\Delta_c$  and  $\Delta_a$ , yield the inverse of the  $c$  and  $a$  lattice constants, respectively. (b) is adapted from [P2].

and the following GaN interlayer (top). Although the  $\text{Al}_{0.81}\text{In}_{0.19}\text{N}$  layers are nominally lattice-matched to GaN in  $a$  direction, Fig. 6.9 shows a clear contrast, i.e. differences in lattice constants. The  $a$  and  $c$  lattice constants of the  $\text{Al}_{0.81}\text{In}_{0.19}\text{N}$  layer deviate from those of GaN by +2 pm and  $-4$  pm, respectively. Thus, the  $c$  and  $a$  lattice constants appear to be 0.75% smaller and 0.59% larger in  $\text{Al}_{0.81}\text{In}_{0.19}\text{N}$  than in GaN, respectively.

Furthermore, a spatial modulation of both lattice constants is discernable, particularly well in the GaN layers. This modulation is investigated by a roughness analysis similar to the one described in the previous section. However, because of the low resolution of the images in Fig. 6.9, at small spatial frequencies the PSD consists of insufficient data points to provide meaningful information. Therefore the respective autocorrelation functions ( $G(l)/G(0)$ ) are computed and shown in Fig. 6.10 for the  $c$  (black) and  $a$  (red) lattice constants. For better visibility the ACF of the  $c$  lattice constant is offset by +1. The modulation is clearly visible with peak to peak distances of 350 nm and 125 nm for the  $c$  and  $a$  lattice constants, respectively.

The wave lengths  $2w$  of these modulations is extracted by fitting sine waves to the autocorrelation functions.  $w$  is the separation between adjacent points of inflection. Since the roughness analysis of the STM measurements was done on the basis of Lorentzian functions,  $w$  is converted into the half width at half maximum of the Lorentzian function. This is done by equalizing the separation of the points of

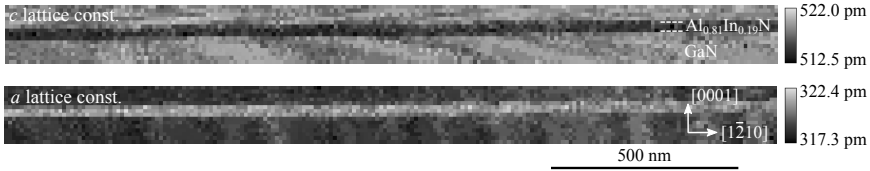


**Figure 6.9:** Spatial distribution of the  $c$  (upper frame) and  $a$  (lower frame) lattice constants of the first  $\text{Al}_{0.81}\text{In}_{0.19}\text{N}$  layer and the surrounding GaN determined from selected area electron diffraction patterns measured by STEM in cross-sectional geometry. The  $\text{Al}_{0.81}\text{In}_{0.19}\text{N}$  layer exhibits a clear contrast with a lower  $c$  and higher  $a$  lattice constant with respect to GaN. In addition a spatial modulation of both lattice constants is visible. The image is adapted from [P2].

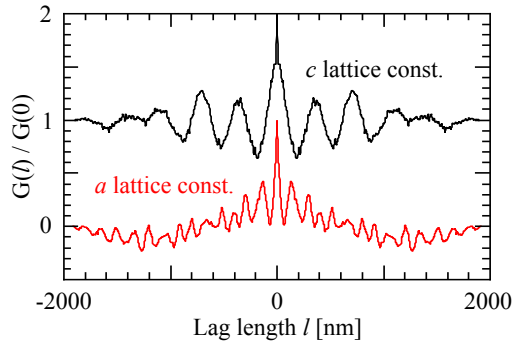


**Figure 6.10:** Normalized autocorrelation functions  $G(l)/G(0)$  of the spatial distribution of the  $a$  (red) and  $c$  (black, offset by +1) lattice constants along the  $[1\bar{2}10]$  direction within the GaN buffer layer. The image is adapted from [P2].

inflection of the sine and Lorentzian functions. Hence the correlation length of the Lorentzian is given as  $c_L = \frac{\sqrt{3}}{2}w$ . For the  $c$  and  $a$  lattice constants  $c_L$  values of  $147 \pm 13$  nm and  $49 \pm 4$  nm are obtained, respectively. This suggests that the F1 and F2 roughness components can be associated with fluctuations of the  $c$  and  $a$  lattice constants, respectively.

## 6.3 Discussion

### 6.3.1 Stress relaxation at the surface

First the roughness component F1 appearing as broad height modulation in the STM images is addressed. It resembles the modulation observed by Chen *et al.* in InGaAsP/InGaP superlattices.[165] This modulation was explained by elastic relaxation of the surface caused by strain due to compositional fluctuations and thickness variations of the superlattice layers. In analogy, here the broad height modulations are assigned to strain relaxation.

The surface of a homogeneously strained sample would relax in the shape of one large convex curvature in contradiction to the observations. Alternating domains of compressive and tensile strain, however, exhibit a wavy inward and outward relaxation as is observed here. Those domains can be caused by compositional fluctuations in the  $\text{Al}_{0.81}\text{In}_{0.19}\text{N}$  layers. Because of the different lattice parameters of AlN ( $c = 498.2$  pm,  $a = 311.2$  pm [166]) and InN ( $c = 569.3$  pm,  $a = 353.3$  pm [167]), a compositional fluctuation in  $\text{Al}_{1-x}\text{In}_x\text{N}$  leads to a fluctuation of its  $a$  and  $c$  lattice constants. In this case, lattice-matching between  $\text{Al}_{0.81}\text{In}_{0.19}\text{N}$  and GaN ( $c = 518.6$  pm,  $a = 318.9$  pm [164]) can no longer be presumed. Locally the  $a$  lattice constant of  $\text{Al}_{1-x}\text{In}_x\text{N}$  is larger (smaller) than  $a_{\text{GaN}}$  where the In content is higher (lower) than 19%. In  $c$  direction lattice-matching between  $\text{Al}_{1-x}\text{In}_x\text{N}$  and GaN is not relevant. However, if the composition of  $\text{Al}_{1-x}\text{In}_x\text{N}$  changes locally, the  $c$  lattice constant within an  $\text{Al}_{0.81}\text{In}_{0.19}\text{N}$  layer changes accordingly. Thus, a compositional fluctuation leads to stress in both crystal directions, that may relax at the cleavage surface. Indeed, compositional fluctuations were found in connection with threading dislocations in similarly grown  $\text{Al}_{1-x}\text{In}_x\text{N}/\text{GaN}$  heterostructures. It was observed that those threading dislocations not only exhibit In rich pit centers, but show a stress related wide zone of In segregation around them.[46] In a distance of approximately 100 nm from the dislocation core a variation of the In content of 5% was still measured. A density of the threading dislocations of  $\sim 4 \times 10^7 \text{ cm}^{-2}$  was given,[19] which is in line with the spatial frequency of the dark and bright stripes of the broad height modulations. Thus, a similar compositional fluctuation is assumed here.

In order to corroborate this interpretation of strain relaxation at the cleavage surface due to compositional fluctuations, calculations are performed with Autodesk Simulation Mechanical 2016, based on ALGOR, by finite element modeling. A  $2.4 \times 2.4 \times 10 \mu\text{m}^3$  GaN sample is modeled with five 30 nm thick layers of  $\text{Al}_{1-x}\text{In}_x\text{N}$  separated by 100 nm thick GaN interlayers. A GaN capping layer of 1  $\mu\text{m}$  thickness is added. The  $\text{Al}_{1-x}\text{In}_x\text{N}$  layers consist of cuboid domains of  $300 \times 300 \times 30 \text{nm}^3$  with alternately less and more In than in the lattice-matched case. This leads to alternating tensile and compressed domains, respectively. The size of the domains was chosen in accordance with the experimentally observed distance of 600 nm between adjacent modulation minima (cf. Fig. 6.1(a)). In the calculation only the cleavage surface is set to relax freely. All other surfaces are fixed.

In order to calculate the strain due to compositional fluctuations, stress tensors of  $\text{Al}_{0.81-\Delta x}\text{In}_{0.19+\Delta x}\text{N}$  and  $\text{Al}_{0.81+\Delta x}\text{In}_{0.19-\Delta x}\text{N}$ , with  $0 < \Delta x < 0.19$  are assigned to the alternating cuboid domains, respectively, giving each  $\text{Al}_{1-x}\text{In}_x\text{N}$  layer the look of a chessboard, as is shown in Fig. 6.11. The figure illustrates the modeled sample without the capping layer for providing a clear view. In the  $\text{Al}_{0.81\pm\Delta x}\text{In}_{0.19\mp\Delta x}\text{N}$  layers, cuboids with In contents of  $0.19 + \Delta x$  and  $0.19 - \Delta x$  are marked in blue and red, respectively. GaN is depicted in green. The total amount of In and Al within the sample is kept constant, since the deviations  $+\Delta x$  and  $-\Delta x$  from the nominal In content occur equally.

The stress tensors are calculated using Hooke's law (Eq. 2.52) as is described in Chap. 2.5. In order to calculate the required strain coefficients,  $\varepsilon_{xx}$ ,  $\varepsilon_{yy}$ , and  $\varepsilon_{zz}$ , first the lattice constants  $a$  and  $c$  are obtained for the different compositions of  $\text{Al}_{0.81\pm\Delta x}\text{In}_{0.19\mp\Delta x}\text{N}$  by linear interpolation between the lattice constants of AlN and InN. Then stress in  $c$  direction for  $\text{Al}_{0.81\pm\Delta x}\text{In}_{0.19\mp\Delta x}\text{N}$  is derived relative to the lattice-matched composition  $\text{Al}_{0.81}\text{In}_{0.19}\text{N}$ , respectively. For a compositional fluctuation of  $\Delta x = 0.05$  the strain coefficients in  $c$  direction are

$$\begin{aligned} \varepsilon_{zz,14\%\text{In}} &= \frac{c_{\text{Al}_{0.86}\text{In}_{0.14}\text{N}} - c_{\text{Al}_{0.81}\text{In}_{0.19}\text{N}}}{c_{\text{Al}_{0.81}\text{In}_{0.19}\text{N}}} = \frac{507.04 - 511.47}{511.47} = -0.0070, \\ \varepsilon_{zz,24\%\text{In}} &= \frac{c_{\text{Al}_{0.76}\text{In}_{0.24}\text{N}} - c_{\text{Al}_{0.81}\text{In}_{0.19}\text{N}}}{c_{\text{Al}_{0.81}\text{In}_{0.19}\text{N}}} = \frac{515.04 - 511.47}{511.47} = +0.0070. \end{aligned} \quad (6.1)$$

Negatively and positively signed strain coefficients represent tensile and compress-

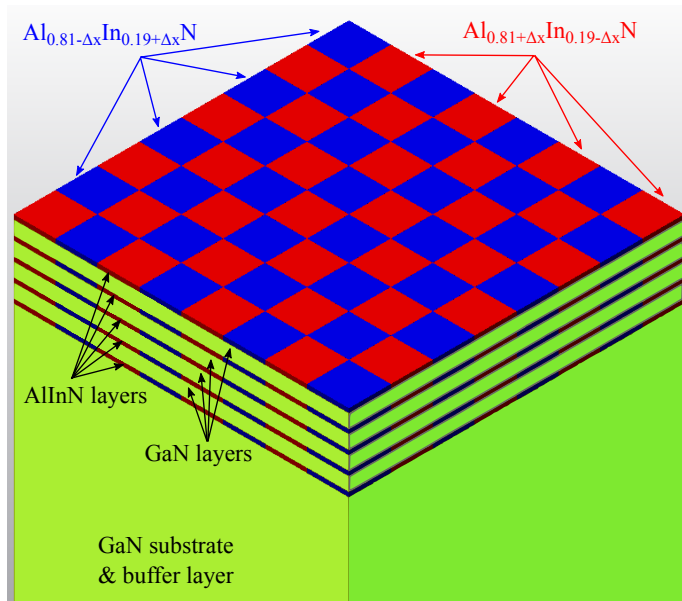


**Figure 6.11:** Modeled sample, shown without capping layer. Areas colored in green symbolize GaN (substrate, buffer and the intermediate layers).  $\text{Al}_{1-(x\pm\Delta x)}\text{In}_{x\pm\Delta x}\text{N}$  layers consist of equally distributed cuboids with different In contents  $x \pm \Delta x$ ,  $0 < \Delta x < 0.19$ . Blue and red cuboids represent In contents of  $0.19 + \Delta x$  and  $0.19 - \Delta x$ , respectively.

sive strain in  $\text{Al}_{0.81 \pm \Delta x} \text{In}_{0.19 \mp \Delta x} \text{N}$ , respectively. The strain coefficients in  $a$  and  $m$  direction are derived by calculating the mismatch of the  $a$  lattice constant between GaN and  $\text{Al}_{0.81 \pm \Delta x} \text{In}_{0.19 \mp \Delta x} \text{N}$  for each composition. A variation of the In content of  $\Delta x = 0.05$  leads to strain coefficients of

$$\begin{aligned} \varepsilon_{xx,14\% \text{In}} &= \frac{a_{\text{Al}_{0.86} \text{In}_{0.14} \text{N}} - a_{\text{GaN}}}{a_{\text{GaN}}} = \frac{317.01 - 318.9}{318.9} = -0.0058, \\ \varepsilon_{xx,24\% \text{In}} &= \frac{a_{\text{Al}_{0.76} \text{In}_{0.24} \text{N}} - a_{\text{GaN}}}{a_{\text{GaN}}} = \frac{321.26 - 318.9}{318.9} = +0.0074. \end{aligned} \quad (6.2)$$

These strain coefficients are inserted into Eq. 2.52, and the resulting stress tensors

$$\underline{\tau}_{14\% \text{In}} = \begin{pmatrix} -3.612 \\ -3.612 \\ -3.709 \\ \dots \end{pmatrix}, \quad \underline{\tau}_{24\% \text{In}} = \begin{pmatrix} 4.405 \\ 4.405 \\ 4.039 \\ \dots \end{pmatrix}, \quad (6.3)$$

are applied to the respective cuboid domains shown in Fig. 6.11.

The out of plane component of the resulting displacement for  $\Delta x = 0.05$ , which corresponds to the relaxation observed on the  $m$  plane ( $10\bar{1}0$ ) in the STM image, is illustrated in Fig. 6.12(a). Blue (red) indicates areas where the sample surface relaxes inward (outward), corresponding to the tensile (compressed) domains. The resulting peak to valley amplitudes and rms roughnesses  $R$  of the relaxed surface are shown in Fig. 6.12(b) for a varying In content from  $\Delta x = 0$  to 0.19. The amplitudes and roughnesses increase linearly with increasing compositional fluctuation, reaching for reasonably expectable In fluctuations of  $\Delta x = 0.05$  roughnesses of 0.24 nm. This roughness value is, however, somewhat too low to explain the observed roughnesses of  $R = 0.56 \pm 0.05$  nm. This suggests additional effects.

It was proposed that the compressive and tensile strained domains contain more and less atomic layers than the average  $\text{Al}_{0.81} \text{In}_{0.19} \text{N}$  layer, respectively.[165] Such additional layers can be introduced by, e.g. threading dislocations (TD). As was mentioned above, in similar grown samples a TD density of  $\sim 4 \times 10^7 \text{ cm}^{-2}$  was reported.[19] Thus, in addition to a fluctuation of the In content, also a thickness variation of the  $\text{Al}_{0.81 \pm \Delta x} \text{In}_{0.19 \mp \Delta x} \text{N}$  layers is considered. For a compositional fluctuation of  $\Delta x = 0.05$  additional unit cells are assumed in  $\text{Al}_{0.81-0.05} \text{In}_{0.19+0.05} \text{N}$

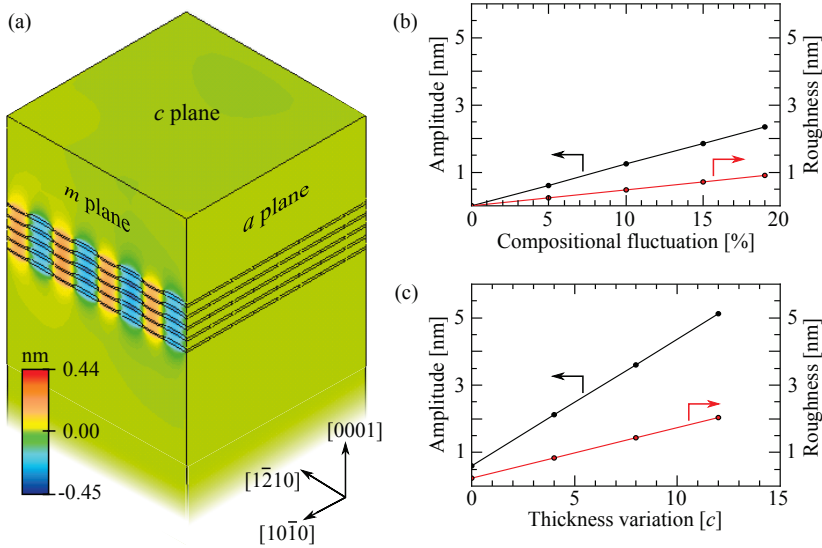


**Figure 6.12:** (a) Color-coded image of the calculated out of plane relaxation at the  $(10\bar{1}0)$  cleavage surface for five  $Al_{1-x}In_xN/GaN(0001)$  pairs embedded in GaN, where each  $Al_{1-x}In_xN$  layer consists of alternating cuboids with an In content of 14% and 24%. The relaxation of the surface, represented by the black lines, is magnified by a factor of 50. (b) Peak to valley amplitude and roughness of the relaxed surface of the  $Al_{0.81\pm\Delta x}In_{0.19\mp\Delta x}N$  layers as a function of the compositional deviation  $\Delta x$  from the nominal In content of 19%. (c) Same, but now for  $Al_{0.81\pm 0.05}In_{0.19\mp 0.05}N$  with in addition different increased or reduced numbers of atomic layers in the compressed and tensile domains, respectively. Adapted from [P2].

domains. The same number of unit cells is subtracted in domains with the composition  $\text{Al}_{0.81+0.05}\text{In}_{0.19-0.05}\text{N}$ . The height of 30 nm of each  $\text{Al}_{0.81\pm 0.05}\text{In}_{0.19\mp 0.05}\text{N}$  cuboid remains unchanged. This assumption alters the stress coefficients in  $c$  direction, only, which are calculated by

$$\varepsilon'_{zz} = \frac{30 \cdot (1 + \varepsilon_{zz}) \pm n \cdot c_{\text{Al}_{0.81\mp 0.05}\text{In}_{0.19\pm 0.05}\text{N}} - 30}{30}, \quad (6.4)$$

where  $n$  gives the number of deviating unit cells in  $c$  direction from the ideal composition of  $\text{Al}_{0.81}\text{In}_{0.19}\text{N}$ . Since  $\varepsilon_{xx}$  and  $\varepsilon_{yy}$  only depend on the differences of the  $a$  lattice constant between GaN and  $\text{Al}_{0.81\pm\Delta x}\text{In}_{0.19\mp\Delta x}\text{N}$ , they are not altered by additional or less atomic layers in  $c$  direction. Figure 6.12(c) illustrates the resulting peak to valley amplitudes and roughnesses of the relaxed surface as a function of the thickness variation. This effect leads to height modulations in agreement with the experimentally observed roughness component F1. This suggests that the contrast of the F1 component is primarily given by strain relaxation of alternating domains with compositional fluctuations and thickness variations. Note, the calculated strain relaxation extends into the surrounding GaN layers, although they have no compositional fluctuations. This is in agreement with the observation.

These two effects directly influence the topography of the sample. However, compositional changes and strain also influence the local electrical properties of the sample. On the one hand, the tunnel current depends on those electrical properties and on the other hand strain induced piezoelectric fields may occur. These (electrical) effects are discussed in the following sections.

### 6.3.2 Strain induced piezoelectric polarization

Since GaN and  $\text{Al}_{1-x}\text{In}_x\text{N}$  crystallize in the wurtzite structure, they exhibit a single polar axis, resulting in a net spontaneous electrical polarization along [0001]. As was described in Sec. 2.6, those spontaneous polarization fields induce electrical fields at the interfaces, only. However, these fields are not visible in the experimentally obtained STM images due to the large height difference between GaN and  $\text{Al}_{0.81}\text{In}_{0.19}\text{N}$  (cf. Chap. 8). In contrast, on strained surfaces additionally a piezoelectric polarization is induced.

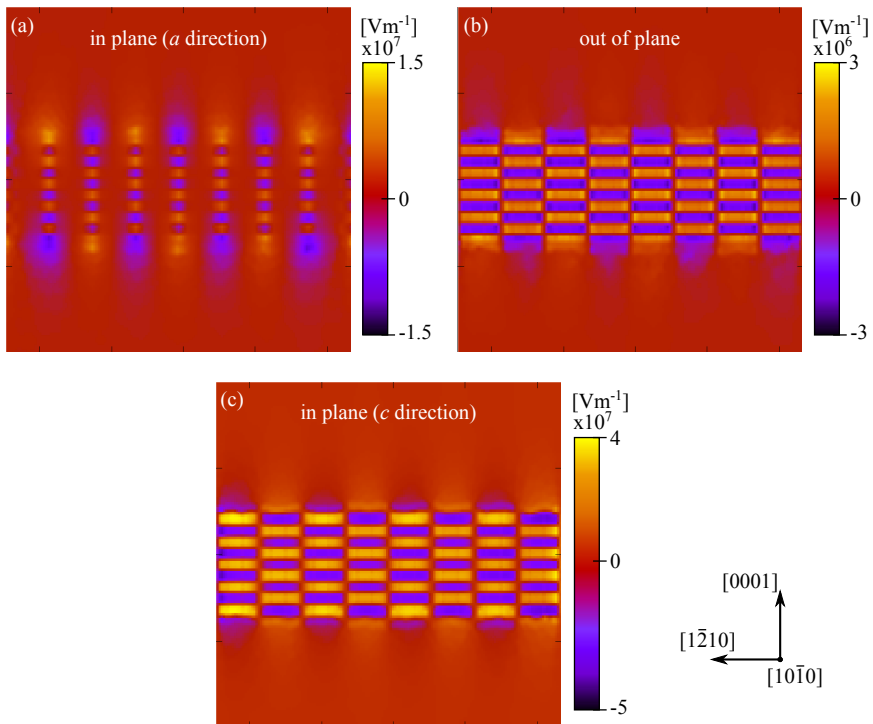


**Figure 6.13:** Color coded images of the three simulated components of the electric field on the  $(10\bar{1}0)$  cleavage surface ( $m$ -plane). The electric field was calculated from the strain-induced piezoelectric polarization based on the simulation of the strain relaxation for a compositional variation of  $\Delta x = 0.05$  described in Sec. 6.3.1. Note, only the  $y$ -component, which is one order of magnitude weaker than the two other components, is measurable with the STM.

In order to calculate those piezoelectric polarization fields, all six  $m$ -plane strain components ( $\varepsilon_{xx}, \varepsilon_{yy}, \varepsilon_{zz}, \varepsilon_{xz}, \varepsilon_{yz}, \varepsilon_{xy}$ ) are extracted from the Autodesk simulation of the strain relaxation (with  $\Delta x = 0.05$ ). Thus, six matrixes are obtained, each consisting of  $i \times j$  strain values describing the  $(10\bar{1}0)$  surface. Then the strain-induced piezoelectric component  $P_{pz}$  of the polarization is calculated following Eq. 2.64 for each point  $(i, j)$ . The resulting electric field is assumed to be parallel and proportional to the piezoelectric polarization

$$\underline{E} = \frac{1}{\varepsilon_0 \chi_e} \cdot \underline{P}_{pz}, \quad (6.5)$$

with  $\varepsilon_0$  being the electric permittivity in vacuum and  $\chi_e$  being the electric susceptibility.  $\chi_e$  is related to the relative permittivity  $\varepsilon_r$  by  $\chi_e = \varepsilon_r - 1$ , which is material-specific. The three resulting components of the electric field at the relaxed  $m$ -plane surface are shown in Fig. 6.13. The in-plane components in  $[0001]$  and  $[\bar{1}210]$  directions exhibit fluctuation ranges of  $9.0 \times 10^7 \text{ Vm}^{-1}$  and  $3.0 \times 10^7 \text{ Vm}^{-1}$ , respectively. The out of plane component in  $[10\bar{1}0]$  direction shows a lower fluctuation of  $6.0 \times 10^6 \text{ Vm}^{-1}$  between areas with different In contents, only. Essentially only the out of plane component can influence the tunnel current in STM measurements. However, since the electric field between STM tip and semiconductor surface typically is in the order of  $10^9 \text{ Vm}^{-1}$ , the STM is insensitive to the weak strain induced piezoelectric polarization. Hence, this effect does not contribute to the modulation of the surface.

### 6.3.3 Changes of the tunnel current due to compositional fluctuations

Next, changes of the tunnel current due to compositional fluctuations in  $\text{Al}_{0.81}\text{In}_{0.19}\text{N}$  are addressed. Therefore the tunnel current is simulated (cf. Sec. 2.2) for different In contents. Since a compositional fluctuation of 5% is assumed, the tunnel current is calculated for  $\text{Al}_{0.81}\text{In}_{0.19}\text{N}$ ,  $\text{Al}_{0.86}\text{In}_{0.14}\text{N}$ , and  $\text{Al}_{0.76}\text{In}_{0.24}\text{N}$  compositions. The relevant material parameters were obtained by linear interpolation between the values of AlN and InN (cf. Tab. 9.1) and are summarized in Tab. 6.1. The band gaps were adapted from Schulz *et al.* [127] (cf. Fig. 4.4), derived with composition dependent

	$\text{Al}_{0.86}\text{In}_{0.14}\text{N}$	$\text{Al}_{0.81}\text{In}_{0.19}\text{N}$	$\text{Al}_{0.76}\text{In}_{0.24}\text{N}$
$E_g$ [eV]	4.12	3.72	3.40
$m_e/m_0$	0.291	0.278	0.265
$m_h/m_0$	4.901	4.716	4.530
$E_D$ [eV]	$E_g - 0.15$	$E_g - 0.15$	$E_g - 0.14$
$\varepsilon$	9.45	9.79	10.13
$\chi$ [eV]	2.4	2.6	2.8
$\mu_n$ [ $\text{cm}^2/\text{Vs}$ ]	426	471	516
$\mu_p$ [ $\text{cm}^2/\text{Vs}$ ]	25	28	32

**Table 6.1:** Material parameters for different compositions of  $\text{Al}_{1-x}\text{In}_x\text{N}$ . The values are obtained by linear interpolation between the material parameters of AlN and InN listed in Tab. 9.1. The band gaps are calculated by Schulz *et al.* [127] using composition dependent bowing parameters. For the calculation of the electron affinities values from Refs. [142] and [132] are used.

bowing parameters. For the electron affinities of AlN and InN values of 1.9 [142] and 5.7 eV [132] were chosen, respectively.

At this stage, the change of the tunnel current due to the influence of the compositional fluctuation on the different material parameters is addressed. The band gap of  $\text{Al}_{1-x}\text{In}_x\text{N}$  changes strongly with compositional fluctuation because of the large difference between the band gaps  $E_g$  of InN (0.7 eV) and AlN (6.2 eV). Because of the  $n$ -type doping, at negative voltages an accumulation current (cf. Chap. 2.2.3) arises that is orders of magnitude larger than the tunnel current related to tunneling out of the valence band. Thus, the tunnel current at negative and positive voltages is dominated by electrons tunneling out of or into the conduction band, respectively. The onset and magnitude of these tunnel currents depend rather on the position of the Fermi level relative to the conduction band edge than on the position of the valence band. Thus, the influence of the band gap on the tunnel current is negligible in this case.

A significant influence on the tunnel current is exerted by the electron affinity  $\chi$ . A locally smaller (larger) In content leads to a smaller (higher) value of  $\chi$ , which increases (decreases) the tunnel current at high voltages (cf. Chap. 5). However, as was discussed in Chap. 5 reasonable doubt about the accuracy of the chosen values of the electron affinities exist. In particular the electron affinity of AlN might be larger, which would decrease the difference between  $\chi_{\text{AlN}}$  and  $\chi_{\text{InN}}$ . Consequently

the difference of the tunnel current for different In contents would be smaller. Furthermore it is uncertain if the compositional dependence of the electron affinity is linear.

For a compositional fluctuation of 5% all other parameters have a minor influence on the tunnel current, only.

In order to obtain the height difference in the STM image due to the influence of different In contents on the tunnel current, the tip-sample separation was used as fit parameter. Figure 6.14 shows the resulting tunnel current at a set voltage of  $V_0 = -4.0$  V (cf. Fig. 6.1) as a function of the tip-sample separation for GaN (blue),  $\text{Al}_{0.86}\text{In}_{0.14}\text{N}$  (red),  $\text{Al}_{0.81}\text{In}_{0.19}\text{N}$  (black), and  $\text{Al}_{0.76}\text{In}_{0.24}\text{N}$  (green). The set current of 0.1 nA is marked by the gray horizontal line. According to this simulation the required tip-sample separations are 1.51 nm, 1.57 nm, and 1.62 nm for In contents of 24, 19, and 14%, respectively. Consequently a compositional fluctuation of 5% results in a change of the tip-sample separation of  $\Delta d \approx 0.05$  nm compared to a uniform composition. However, because of the uncertainty of reliable values of  $\chi_{\text{AlInN}}$ , the theoretically obtained change in the tip-sample separation of  $\Delta d \approx 0.05$  nm can be taken as an upper limit. Thus, in agreement with other works,[168, 169] electronic effects of the different In compositions result in height changes one order of magnitude smaller than changes due to the strain relaxation of the surface. Hence, electronic effects can be neglected. Note, with a higher (lower) In content, the tip-sample separation becomes smaller (larger), resulting in depression (elevation) in an STM image. This effect partly counteracts the height change in the STM images due to strain relaxation.

### 6.3.4 Dislocations

At this stage we turn to the roughness component F2. The SAED measurements shown in Fig. 6.9(a) illustrate that the  $a$  lattice constant is 0.59% larger in the  $\text{Al}_{0.81}\text{In}_{0.19}\text{N}$  layer than in GaN. Such a misfit strain is typically relieved by an interface dislocation network, with an average separation of edge dislocations with  $a$ -type Burgers vector of  $\sim 54$  nm. This value agrees well with the correlation length of the F2 component. Furthermore dislocations with  $a$ -type Burgers vector

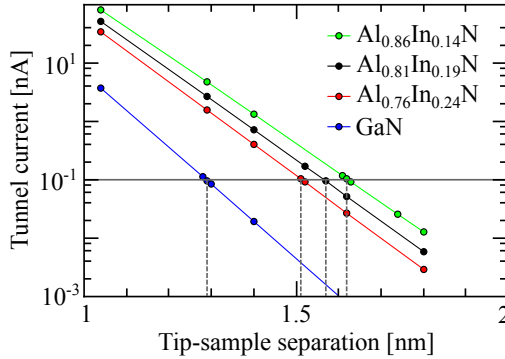


**Figure 6.14:** Simulated tunnel current as a function of the tip-sample separation at a set voltage of  $-4.0\text{ V}$  for GaN (blue),  $\text{Al}_{0.76}\text{In}_{0.24}\text{N}$  (red),  $\text{Al}_{0.81}\text{In}_{0.19}\text{N}$  (black), and  $\text{Al}_{0.86}\text{In}_{0.14}\text{N}$  (green). The curves comply with a set current of  $0.1\text{ nA}$  at tip-sample separations of  $1.29\text{ nm}$ ,  $1.51\text{ nm}$ ,  $1.57\text{ nm}$ , and  $1.62\text{ nm}$ , respectively. Thus, the difference in tip-sample separation due to a compositional variation of  $5\%$  amounts to  $\sim 0.05\text{ nm}$ .

will primarily affect the  $a$  lattice constant. Hence, we attribute the roughness component F2 to the presence of interface edge dislocations.

The presence of interface edge dislocations is corroborated by the increasing appearance of monoatomic steps within consecutive  $\text{Al}_{0.81}\text{In}_{0.19}\text{N}$  layers in analogy to interface edge dislocations at the  $\text{InN}/\text{GaN}$  interface.[81] The steps lead to an increased roughness within the  $\text{Al}_{0.81}\text{In}_{0.19}\text{N}$  layers compared to the surrounding GaN. Therefore, the roughness component F3 with  $\sim 10\text{ nm}$  correlation length can be associated with the atomic steps seen on the surface. The development of steps within consecutive  $\text{Al}_{0.81}\text{In}_{0.19}\text{N}$  layers will be further discussed in Chap. 7.

## 6.4 Conclusion

Strain and compositional fluctuations in a nominally lattice matched  $\text{Al}_{0.81}\text{In}_{0.19}\text{N}/\text{GaN}$  heterostructure were investigated by STM and SAED measurements. STM measurements of the cross-sectional  $(10\bar{1}0)$  cleavage surface revealed pronounced height modulations at the  $\text{Al}_{0.81}\text{In}_{0.19}\text{N}$  cleavage surface whereas the GaN substrate exhibited a flat, smooth surface. By calculating the PSD from STM height profiles,

the correlation lengths and rms-roughnesses of three different components (F1, F2, and F3) of the height modulation were identified (cf. Fig. 6.3). F1 appears on the buffer layer close to the  $\text{Al}_{0.81}\text{In}_{0.19}\text{N}$  layers and extends through all five  $\text{Al}_{0.81}\text{In}_{0.19}\text{N}$  layers and weakly into the capping layer. It gives rise to the broad height modulations showing up as diagonally running stripes. In the  $\text{Al}_{0.81}\text{In}_{0.19}\text{N}$  layers this component exhibits an average correlation length of  $133 \pm 10$  nm. The components F2 and F3 are mainly detectable in the  $\text{Al}_{0.81}\text{In}_{0.19}\text{N}$  layers with average correlation lengths of  $39 \pm 1$  nm and  $10 \pm 1$  nm, respectively.

Electron diffraction patterns revealed a contraction (dilatation) of the  $c$  ( $a$ ) lattice constant of  $\text{Al}_{0.81}\text{In}_{0.19}\text{N}$  relative to GaN by 0.75% (0.59%). In addition spatial fluctuations of the  $c$  and  $a$  lattice constant were found with correlation lengths of  $147 \pm 13$  nm and  $49 \pm 4$  nm, respectively. The fluctuations were associated with the F1 and F2 roughness component observed by STM, respectively. The third feature F3 did not appear in the STEM measurement.

It is demonstrated that strain due to compositional fluctuations induces the roughness and height modulations at the cleavage surface and local changes of the lattice constants. The strain relaxes at the cleavage surface leading to height modulations. The three roughness components can be attributed to (i) alternately compressive and tensile strained domains arising from compositional fluctuations, (ii) interface misfit edge dislocations, which strain primarily the  $a$  lattice constant, and (iii) surface steps.



# Chapter 7

## Defects in $\text{Al}_{1-x}\text{In}_x\text{N}$

The analysis of the roughness of the  $\text{Al}_{1-x}\text{In}_x\text{N}$  layers in Chap. 6 indicated the presence of defects at the  $\text{Al}_{1-x}\text{In}_x\text{N}/\text{GaN}$  interfaces. Therefore, this chapter addresses the types of defects and their spatial distribution detectable on cross-sectional cleavage surfaces.

### 7.1 Experimental results

On every cleavage surface of the investigated samples surface steps occur within the  $\text{Al}_{1-x}\text{In}_x\text{N}$  layers. As an example Fig. 7.1(a) presents a cross-sectional overview consisting of a mosaic of STM images acquired on a  $(10\bar{1}0)$  cleavage surface of the  $\text{Al}_{0.80}\text{In}_{0.20}\text{N}/\text{GaN}$  distributed Bragg reflector heterostructure A3214. In this image, the formation and termination of steps and terraces can be observed particularly well. From left to right the image shows the GaN substrate, the GaN buffer layer, and part of the  $\text{Al}_{0.80}\text{In}_{0.20}\text{N}/\text{GaN}$  DBR heterostructure. The interface between substrate and buffer layer appears as fine dark line. Several horizontally aligned steps are visible in the DBR structure. These steps are slightly inclined from the  $[0001]$  growth direction. In addition, large steps are present in the GaN substrate and the GaN buffer layer. These are commonly observed on  $(10\bar{1}0)$  cleavage surfaces of GaN pseudosubstrates.[170, 171] In order to highlight the edges of the steps, Fig. 7.1(b) shows the directional derivative of the STM image along the  $[1\bar{2}10]$  direction. In this image steps appear either as bright (downward steps seen from

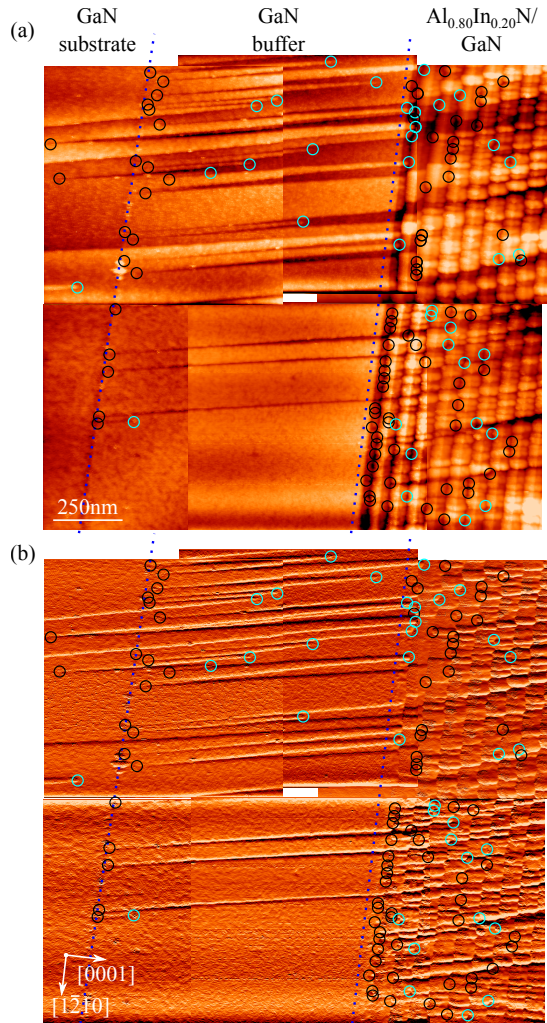


**Figure 7.1:** (a) Cross-sectional overview consisting of a mosaic of constant-current STM images of the  $Al_{0.80}In_{0.20}N/GaN$  distributed Bragg reflector heterostructure A3214 measured at  $-4.0$  V and  $5$  pA. From left to right, separated by dashed lines, the GaN substrate, the GaN buffer layer, and the first part of the 42 pairs of  $Al_{0.80}In_{0.20}N/GaN$  layers are shown. (b) Derivative of (a) along the  $[1210]$  direction used to highlight the steps. Positions where needle-shaped terraces and steps arise are marked by black circles, while light blue circles point to positions where steps and needle shaped terraces terminate in (a) and (b).

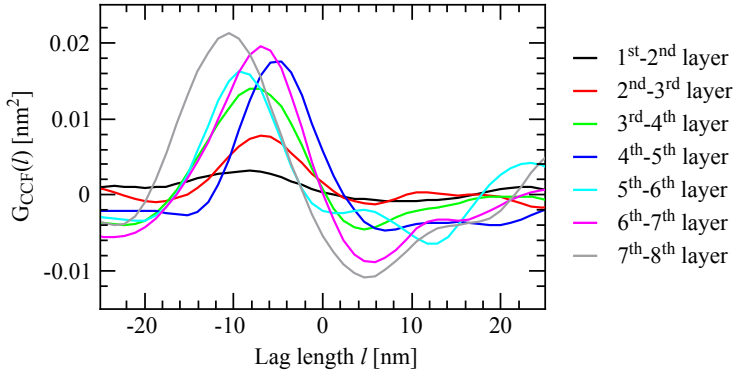


**Figure 7.2:** Averaged cross-covariance functions calculated from height profiles of the first eight  $\text{Al}_{0.80}\text{In}_{0.20}\text{N}$  layers obtained in the directional derivative image. The cross-covariance functions were obtained in the upper and lower part of Fig. 7.1(b) separately and averaged for each  $\text{Al}_{0.80}\text{In}_{0.20}\text{N}$  layer.

top to bottom) or as dark lines (upward steps). The origins of the steps and narrow terraces in  $[0001]$  growth direction are marked by black circles in Fig. 7.1(a) and (b), while light blue circles point to positions where they terminate.

In the area of the GaN pseudosubstrate only few steps are present. At the interface between substrate and GaN buffer layer however, a series of paired up and down steps appear, forming needle-shaped terraces. Some of the terraces already terminate within the buffer layer, but the majority continues into the  $\text{Al}_{0.80}\text{In}_{0.20}\text{N}/\text{GaN}$  DBR layers. Behind the buffer layer in the region of the first pair of  $\text{Al}_{0.80}\text{In}_{0.20}\text{N}/\text{GaN}$  layers, many additional steps appear. In the subsequent  $\text{Al}_{0.80}\text{In}_{0.20}\text{N}/\text{GaN}$  layers the number of newly formed steps apparently decreases. After three pairs of  $\text{Al}_{0.80}\text{In}_{0.20}\text{N}/\text{GaN}$  layers, a saturation of the step density is reached.

A particular feature of the step morphology is that the steps and needle-shaped terraces seem to be frequently offset at the  $\text{Al}_{0.80}\text{In}_{0.20}\text{N}/\text{GaN}$  interfaces. This leads to a stair-like shape of the steps. In order to unravel this step structure, height profiles of the directional derivative of the first eight  $\text{Al}_{0.80}\text{In}_{0.20}\text{N}$  layers are obtained in the upper and lower half of Fig. 7.1(b), respectively. From the eight height profiles the seven cross-covariance functions (CCF) of adjacent profiles are calculated as described in Chap. 2.7.3. The resulting CCFs for the upper and lower

half of the STM image are averaged for each  $Al_{0.80}In_{0.20}N$  layer and are shown in Fig. 7.2. All CCFs exhibit their largest peak at small negative lag lengths of  $-7.4 \pm 1.5$  nm. With a layer separation of 85 nm this indicates an average inclination of  $\sim 5.0^\circ$  with respect to the [0001] direction. In general the amplitude of the peak increases with layer number, reaching a saturation after about three layers. This reflects the increase and saturation of the step density described above.

A higher resolved STM image of the  $(10\bar{1}0)$  cleavage surface of the DBR sample A2688 is presented in Fig. 7.3(a). It shows a part of the  $Al_{1-x}In_xN/GaN$  DBR structure. Again, black circles mark examples of the origin of a step, while blue circles mark positions where steps terminate. The steps are emphasized by the derivative along the  $[1\bar{2}10]$  direction in (b). The image corroborates that within the DBR structure, about as many steps are formed as terminate. The height profile in Fig. 7.3(c) was obtained on an  $Al_{0.80}In_{0.20}N$  layer along the white box illustrated in (a). The step height covers a range from one ( $\frac{\sqrt{3}}{2}a \sim 0.28$  nm) to three monolayers (ML). Additionally a height shift of  $\frac{1}{3}ML$  is found that probably is caused by a stacking fault.

## 7.2 Discussion

The particular step structure is the result of the interaction of the crack tip propagation during the cleavage process, with the mechanical properties of the different layers, defects, and strain present in the material. In a first approximation, the elastic constants of GaN and  $Al_{0.80}In_{0.20}N$  can be assumed to be rather similar. Hence, the step structure is primarily governed by defects and strain.

For the further discussion one has to distinguish between the steps which are defining needle-shaped terraces and those in the  $Al_{0.80}In_{0.20}N/GaN$  layers. The needle-shaped terraces appear to form primarily at the GaN buffer/GaN pseudosubstrate interface. The dark contrast at the interface points toward a local carrier depletion. This suggests that at the GaN buffer/GaN pseudosubstrate interface impurities induce deep levels reducing the concentration of free electrons. These impurities disturb and locally strain the GaN. Strain is known to lead to irregularities in the crack propagation during cleavage and thereby to steps.[172–176]

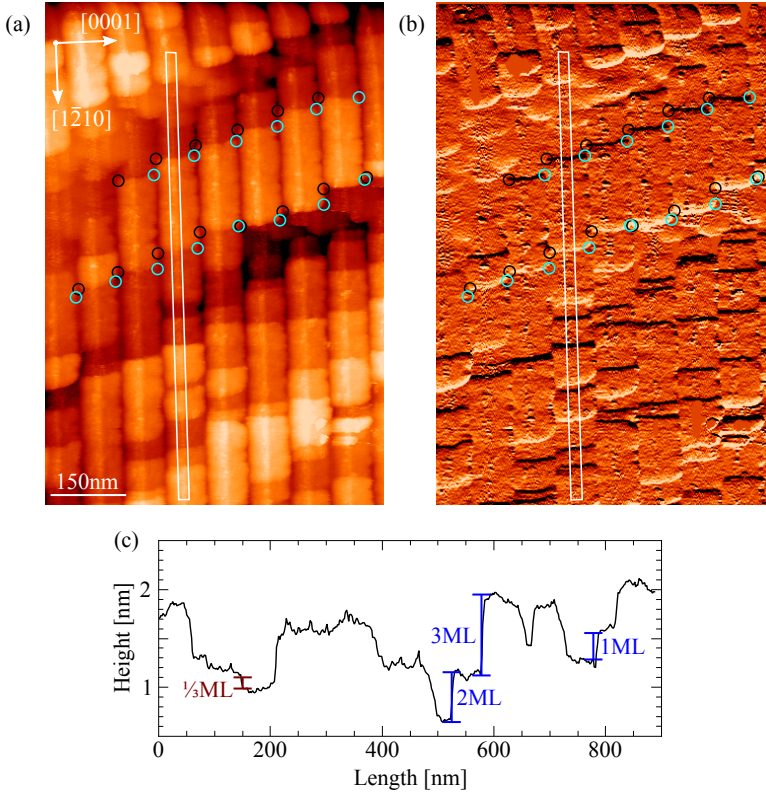


**Figure 7.3:** (a) Cross-sectional STM image of the  $\text{Al}_{1-x}\text{In}_x\text{N}/\text{GaN}$  distributed Bragg reflector heterostructure A2688 measured at  $-5.0\text{ V}$  and  $100\text{ pA}$  on the  $(10\bar{1}0)$  cleavage surface. Black circles mark some examples of the origin of a step, while blue circles mark positions where these steps terminate. The image corroborates, that within the DBR structure, about as many steps are formed as terminate. (b) Derivative of (a) along the  $[1\bar{2}10]$  direction used to highlight the steps. (c) Height profile obtained along the white box illustrated in (a). The step height covers a range from one ( $\frac{\sqrt{3}}{2}a \sim 0.28\text{ nm}$ ) to three monolayers (ML). The height shift of  $\frac{1}{3}\text{ML}$  probably is induced by a stacking fault.

In contrast the presence of the stair-like shaped steps within the  $Al_{0.80}In_{0.20}N/GaN$  layers point to a different physical origin. Figure 7.3 indicates that the stair-like shaped steps consist rather of individual steps formed at the  $Al_{0.80}In_{0.20}N/GaN$  interfaces and annihilating at the following  $GaN/Al_{0.80}In_{0.20}N$  interface. Similar steps at  $InN/GaN$  interfaces were connected to the presence of dislocations.[81] Dislocations usually form during growth at interfaces of non-lattice matched layers. This type of dislocations were found to induce 1ML high steps at  $InN/GaN$  interfaces and exhibit a Burgers vector of the type  $a/3 \langle 11\bar{2}0 \rangle$ . [171] The dislocations were attributed to the relaxation of strain induced by the lattice mismatch between  $GaN$  and  $InN$ . [81] Similar effects can be expected at  $Al_{0.80}In_{0.20}N/GaN$  interfaces. Although the  $Al_{0.80}In_{0.20}N$  layers are nominally lattice matched to  $GaN$ , the different thermal extension coefficients as well as fluctuations or deviations from the intended  $In$  concentration lead to somewhat strained layers.

Indeed the roughness analysis in Chap. 6 suggests the presence of an interface dislocation network giving rise to the roughness component F2. The correlation length of this roughness component suggests an average separation of the misfit dislocations of  $\sim 40$  nm. The average step density within the  $Al_{0.80}In_{0.20}N$  layers yield an average step separation of  $\sim 45$  nm. This agrees well with the estimation of the misfit dislocation separation.

### 7.3 Conclusion

Surface steps occurring on  $(10\bar{1}0)$  cleavage surfaces of  $Al_{0.80}In_{0.20}N/GaN$  DBR heterostructures were investigated by cross-sectional STM. The steps were found to be slightly inclined from the  $[0001]$  growth direction. Cross-covariance functions of adjacent  $Al_{0.80}In_{0.20}N$  layers indicate that the step density reaches a saturation after three pairs of  $Al_{0.80}In_{0.20}N/GaN$  layers. At the  $Al_{0.80}In_{0.20}N/GaN$  interfaces the steps appear to be frequently offset. However, highly resolved STM images suggest that these stair-like shaped steps actually consists of individual steps forming at the  $Al_{0.80}In_{0.20}N/GaN$  interfaces and annihilating at the following inverted ones. Those steps could be attributed to the presence of dislocations forming during growth at the interfaces due to strain.

# Chapter 8

## Contrast between GaN- and $\text{Al}_{x-1}\text{In}_x\text{N}$ -layers

The STM images of the  $\text{Al}_{1-x}\text{In}_x\text{N}/\text{GaN}$  heterostructures presented so far (Figs. 4.1 and 6.1) exhibit a strong contrast between the two materials. The  $\text{Al}_{1-x}\text{In}_x\text{N}$  layers appear brighter than the surrounding GaN. Thus the tip is retracted and the corresponding height values obtained in the constant-current mode on  $\text{Al}_{1-x}\text{In}_x\text{N}$  are larger than on GaN. The physical origin of this contrast is investigated in this chapter.

### 8.1 Experimental results

In order to identify the physical origin of the contrast between  $\text{Al}_{1-x}\text{In}_x\text{N}$  and GaN different experimental observations are summarized. First, attention is drawn to Fig. 6.1 presented in Chap. 6.1. The uppermost part of the image is reproduced in Fig. 8.1 with a height profile measured at the position marked by the horizontal white line. The height profile in Fig. 8.1(b) shows, from left to right in growth direction, part of the GaN substrate, the GaN buffer layer, the five  $\text{Al}_{0.81}\text{In}_{0.19}\text{N}/\text{GaN}$  layers, and part of the GaN capping layer. The interfaces between these sections are indicated by red dotted lines. Compared to the surrounding GaN, the average elevation of the  $\text{Al}_{0.81}\text{In}_{0.19}\text{N}$  layers amounts to approximately 3.5 nm, as indicated by the blue lines. Note, the interface between substrate and buffer layer appears as

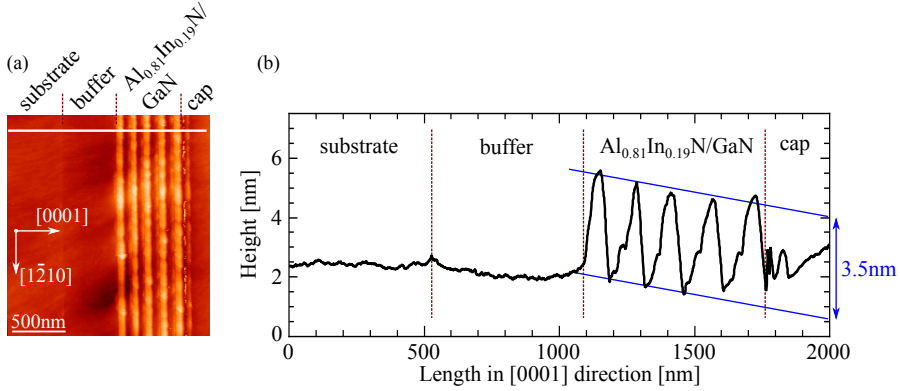


**Figure 8.1:** (a) Cross-sectional STM image of the  $Al_{0.81}In_{0.19}N/GaN$  heterostructure A3162, measured at  $-4.0V$  and  $100pA$ . (b) Height profile in  $[0001]$  direction measured at the position of the horizontal white line in (a). The image and the profile show from left to right a part of the GaN substrate, the GaN buffer layer, the five  $Al_{0.81}In_{0.19}N/GaN$  layers, and part of the GaN capping layer. The height difference between GaN and the  $Al_{0.81}In_{0.19}N$  layers amounts to approximately  $3.5nm$ .

a small bump, only and the small peaks after the last  $Al_{0.81}In_{0.19}N$  layer are caused by a weak double tip and thus are not of interest.

Furthermore, the same cleavage surface is examined with a scanning-near field optical microscope (SNOM) based on an atomic-force microscope (AFM). The principles of both microscopes are elucidated in Chap. 2.4. AFM primarily probes the topography of a surface without contributions of electrical properties. The optical signal, in contrast, is virtually independent of the topography. The AFM image in Fig. 8.2(a) shows three  $Al_{0.81}In_{0.19}N$  layers (on the leftmost side, in the middle, and on the rightmost side) and the intermediate GaN layers. Again, the  $Al_{0.81}In_{0.19}N$  layers appear brighter and are therefore higher than the surrounding GaN. In order to quantify the topography, a height profile perpendicular to the  $Al_{0.81}In_{0.19}N$  layers is averaged in the area marked by the white box in (a). The average height profile is shown in Fig. 8.2(b). The red dashed lines mark the approximate positions of the interfaces between  $Al_{0.81}In_{0.19}N$  and GaN. The interfaces were identified using the peak positions and the nominal thicknesses of the layers of  $30nm$   $Al_{0.81}In_{0.19}N$  and  $105nm$  GaN. As indicated by the blue lines, the height profile reveals again a

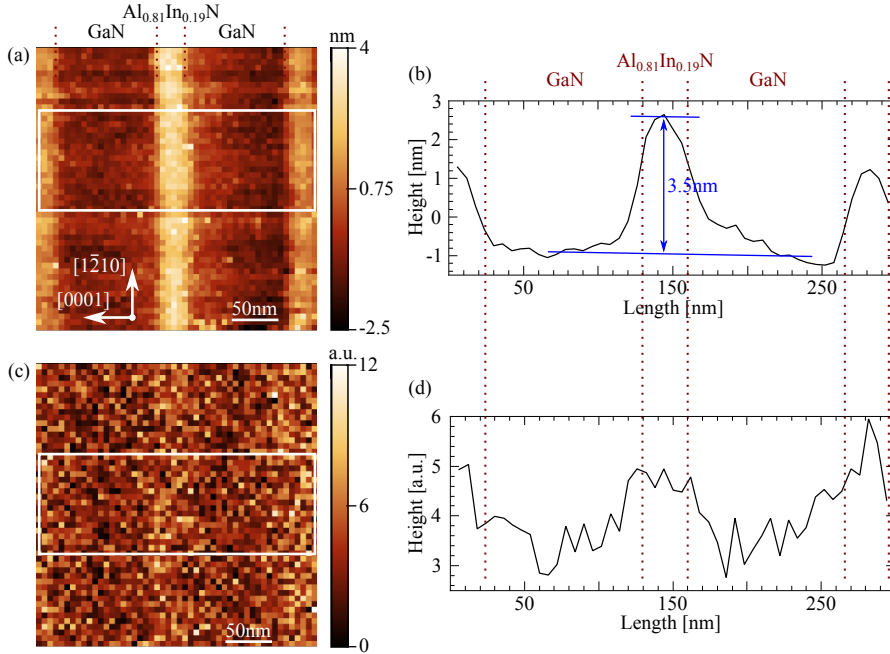


**Figure 8.2:** (a) Topography of three  $\text{Al}_{0.81}\text{In}_{0.19}\text{N}$  layers (on the leftmost side, in the middle, and on the rightmost side) and the intermediate GaN layers measured by AFM. (b) Height profile averaged in the area marked by the white box in (a). The dashed red lines mark the approximate positions of the interfaces between  $\text{Al}_{0.81}\text{In}_{0.19}\text{N}$  and GaN. The profile reveals a height difference of  $\sim 3.5$  nm between  $\text{Al}_{0.81}\text{In}_{0.19}\text{N}$  and GaN. (c) Optical near-field image (second harmonic amplitude) of the same section shown in (a). The scale is arbitrary. (d) Corresponding height profile. Only a weak difference in the intensity of the second harmonic amplitude between  $\text{Al}_{0.81}\text{In}_{0.19}\text{N}$  and GaN is detectable. The images were measured by F. Gaussmann at the Fraunhofer Institute for Laser Technology (ILT).

height difference of  $\sim 3.5$  nm between  $\text{Al}_{0.81}\text{In}_{0.19}\text{N}$  and GaN.

Simultaneously to the AFM image, an optical near-field image (second harmonic amplitude) was obtained. In the optical amplitude signal presented in Fig. 8.2(c) the  $\text{Al}_{0.81}\text{In}_{0.19}\text{N}$  layers can barely be distinguished from the surrounding GaN. The corresponding profile (Fig. 8.2(d)), shows only a weak intensity in the regions of the  $\text{Al}_{0.81}\text{In}_{0.19}\text{N}$  layers.

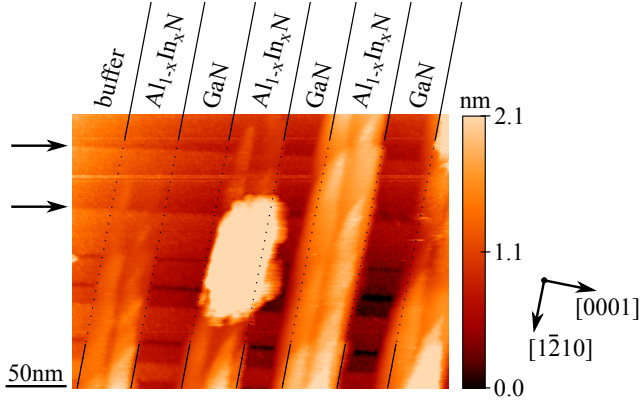


**Figure 8.3:** Cross-sectional STM image of the  $\text{Al}_{1-x}\text{In}_x\text{N}/\text{GaN}$  DBR structure A2688 measured at  $-4.0\text{ V}$  and  $100\text{ pA}$ . Black solid and dashed lines indicate the location of the first three  $\text{Al}_{1-x}\text{In}_x\text{N}$  and GaN layers. The buffer layer is visible on the far left side. The first  $\text{Al}_{1-x}\text{In}_x\text{N}$  layer is only partially visible. In the upper part steps from the buffer layer extend uninterrupted into the DBR structure. In parts the second layer is still translucent for the underlying steps, while from the third layer up the height of the  $\text{Al}_{1-x}\text{In}_x\text{N}$  dominates the contrast. The brightest dot in the center of the image is an impurity and hence not of interest.

Second, other cleavage surfaces exhibited a vanishing contrast. An example of a partial vanishing of the outward protrusion is presented in Fig. 8.3. The constant current STM image shows a section of sample A2688 measured at  $-4.0\text{ V}$  and  $100\text{ pA}$ . On the far left side a part of the GaN buffer layer is visible, followed by the beginning of the DBR structure with alternating layers of  $\text{Al}_{1-x}\text{In}_x\text{N}$  and GaN. Black lines indicate the location of  $\text{Al}_{1-x}\text{In}_x\text{N}$  and GaN layers. The first  $\text{Al}_{1-x}\text{In}_x\text{N}$  layer is only partially visible. In the upper part of the image no interface between GaN buffer layer and  $\text{Al}_{1-x}\text{In}_x\text{N}$  can be seen. Instead steps from the buffer layer extend uninterrupted into the DBR structure (see arrows, the other perfectly horizontal lines are due to tip instabilities). In parts the underlying steps still can be observed in the second  $\text{Al}_{1-x}\text{In}_x\text{N}$  layer. From the third layer on the topographic height of the  $\text{Al}_{1-x}\text{In}_x\text{N}$  layers dominates the contrast. The bright white area in the centre of the image is an impurity (dust) on the surface and is not of interest.

Third, an inversion of the contrast between  $\text{Al}_{1-x}\text{In}_x\text{N}$  and GaN is shown in Fig. 8.4(a). The STM image was measured on a different cleavage surface of the  $\text{Al}_{0.81}\text{In}_{0.19}\text{N}/\text{GaN}$

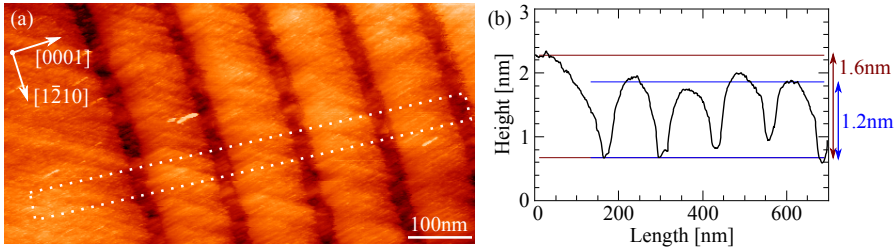


**Figure 8.4:** (a) Cross-sectional STM image of the  $\text{Al}_{0.81}\text{In}_{0.19}\text{N}/\text{GaN}$  heterostructure A3162 measured at  $-4.0$  V and  $100$  pA.  $\text{Al}_{0.81}\text{In}_{0.19}\text{N}$  layers are depressed. (b) The height profile, obtained in the area marked by the white dashed box in (a) reveals a height difference of  $\sim 1.2$  nm between  $\text{Al}_{0.81}\text{In}_{0.19}\text{N}$  and the GaN interlayers. The first  $\text{Al}_{0.81}\text{In}_{0.19}\text{N}$  layer lies  $\sim 1.6$  nm deeper than the buffer layer.

heterostructure A3162 at  $-4.0$  V and  $100$  pA. In this image the  $\text{Al}_{0.81}\text{In}_{0.19}\text{N}$  layers exhibit lower height values than the surrounding GaN. The height profile in Fig. 8.4(b) was obtained in the area marked by the white dashed box in (a). It reveals a height difference of  $\sim 1.2$  nm between  $\text{Al}_{0.81}\text{In}_{0.19}\text{N}$  and the GaN interlayers. Compared to the GaN buffer layer, the first  $\text{Al}_{0.81}\text{In}_{0.19}\text{N}$  layer lies deeper, with a height difference of  $\sim 1.6$  nm.

## 8.2 Discussion

Although all STM images shown above were acquired under identical conditions ( $-4.0$  V,  $100$  pA), the contrast between  $\text{Al}_{1-x}\text{In}_x\text{N}$  and GaN occurs in various forms. In most cases  $\text{Al}_{1-x}\text{In}_x\text{N}$  protrudes outward. However, the magnitude of the protrusion can change dramatically. A maximum height difference of  $\sim 3.5$  nm between  $\text{Al}_{0.81}\text{In}_{0.19}\text{N}$  and GaN was found whereas lower and even vanishing protrusion were observed on other cleavage surfaces. Additionally it was found that the height contrast can be reversed.

The contrast between the  $\text{Al}_{1-x}\text{In}_x\text{N}$  and GaN layers can be caused by electric and/or mechanical properties of the materials. In order to determine the physical origin of the contrast, first of all the influence of the different material properties on the tunnel current is investigated. Therefore the simulation of the tunnel cur-

rent for GaN and  $Al_{1-x}In_xN$  presented in Chap. 6.3.3 is recalled. This simulation revealed that in order to maintain a set-point of  $-4.0$  V and  $100$  pA for GaN and  $Al_{0.81}In_{0.19}N$ , the tip-sample separation changes by  $0.28$  nm at most. Thus, the impact of the different electrical properties of  $Al_{1-x}In_xN$  and GaN on the tunnel current is too small to account for the contrast observed experimentally. A pure electronic origin would also be in conflict with the contrast reversal at identical tunnel conditions. This is corroborated by the SNOM measurement. In the optical signal the difference between  $Al_{0.81}In_{0.19}N$  and GaN is weak, indicating the dominance of the topographic structure on the STM image contrast. In addition the height difference between  $Al_{1-x}In_xN$  and GaN observed in the AFM image matches the value obtained from the STM image of the same sample almost exactly. Consequently, the contrast between  $Al_{1-x}In_xN$  and GaN is dominated by mechanical properties of the surface. Figure 8.3 suggests that in STM images at negative voltages  $Al_{1-x}In_xN$  only exhibits a contrast to GaN if it mechanically protrudes from the surrounding GaN. Otherwise the two materials cannot be distinguished by STM at negative voltages.

The formation of protruding  $Al_{1-x}In_xN$  layers compared to GaN might be caused by an outward relaxation of the biaxially strained  $Al_{1-x}In_xN$  layers at the cleavage surface. A compressive (tensile) strain would lead to an outward (inward) relaxation. Assuming a reasonably homogeneous  $Al_{1-x}In_xN$  layer, the strain should thus lead either to an outward or inward relaxation, which is in conflict with the contrast reversal.

Thus, most likely the contrast between the  $Al_{0.81}In_{0.19}N$  and GaN layers arises from the cleavage process. The morphology of the cleavage surface reflects the path of the crack tip through the material during the cleavage process.[177–179] Height changes in the topography relative to the intended cleavage plane indicate deflections of the crack tip. Such deflections can be caused by defects, at interfaces due to different mechanical properties of the two materials, or by strain. Indeed strained material cleaves with high step densities [172] and in XSTM steps occur preferentially at strained layers.[173–176] In addition dislocations are likely present at the interfaces, which also leads to additional steps. The cleavage behavior at the  $Al_{1-x}In_xN$ /GaN interfaces can be attributed to the sum of these effects, which govern the contrast of the  $Al_{1-x}In_xN$  layers.

## 8.3 Conclusion

In constant-current STM images of  $\text{Al}_{0.81}\text{In}_{0.19}\text{N}/\text{GaN}$  heterostructures a strong contrast was detected between the two materials. Generally the  $\text{Al}_{0.81}\text{In}_{0.19}\text{N}$  layers appear brighter than GaN with height differences of up to 3.5 nm. However, on other cleavage surfaces those protrusions were lower and even vanished in separate areas, or the contrast was found to be reversed.

Based on AFM and SNOM images, the contrast between  $\text{Al}_{0.81}\text{In}_{0.19}\text{N}$  and GaN was attributed to mechanical properties of the cleavage surface. This was corroborated by simulations of the tunnel current, which indicate that the electrical properties of the two materials cause a height difference in STM images one order of magnitude smaller than the measured protrusions. It was concluded that during the cleavage process the crack tip is deflected from the intended cleavage plane at the interfaces by defects or strain, forming the height changes in the topography of the surface.



# Chapter 9

## Summary

In this thesis different lattice-matched  $\text{Al}_{1-x}\text{In}_x\text{N}/\text{GaN}$  heterostructures were investigated with the aim to deduce strain, compositional fluctuations, defects, and electronic properties on cross-sectional  $m$ -plane  $\text{Al}_{1-x}\text{In}_x\text{N}$  cleavage surfaces.

The electronic properties of  $\text{Al}_{1-x}\text{In}_x\text{N}(10\bar{1}0)$  surfaces were investigated by cross-sectional scanning tunneling spectroscopy in combination with density functional theory calculations. The calculations revealed empty Al and/or In-derived dangling bond states at the surface, which were calculated to be within the fundamental bulk band gap for In contents smaller than 60%. For In contents of  $x = 0.19$  and  $x = 0.20$ , the energy of the lowest empty In-derived surface state was extracted from tunnel spectra acquired on  $\text{Al}_{1-x}\text{In}_x\text{N}(10\bar{1}0)$  cleavage surfaces to be  $E_C - 1.82 \pm 0.41$  eV and  $E_C - 1.80 \pm 0.56$  eV, respectively, in good agreement with the calculated energies. In addition, a polarity dependent Fermi-level pinning of the surface state was identified. Based on these results it was concluded, that under growth conditions the Fermi level is pinned by the In-derived dangling bond state for In contents smaller than about 60%. For larger In contents no Fermi level pinning is present.

In order to fit simulations to the experimentally obtained tunnel spectra, an average value of the electron affinity  $\chi_{\text{AlInN}}$  of  $3.5 \pm 0.1$  eV was necessary. A thorough literature survey of theoretically and experimentally obtained values of the electron affinities of GaN, AlN, and InN revealed two issues. First, a broad range of values was reported for the electron affinities with deviations of more than 50%. Second,

the values needed for the simulations are larger than the value obtained by linear interpolation between the binary electron affinities  $\chi_{\text{AlN}}$  and  $\chi_{\text{InN}}$  reported in literature. This discrepancy indicates either a non-linear compositional dependence of  $\chi_{\text{AlInN}}$ , or a difference of the electron affinity on non-polar surfaces and reported values obtained on polar surfaces. Both assumptions make a reassessment of the electron affinity necessary.

Strain and compositional fluctuations in an  $\text{Al}_{0.81}\text{In}_{0.19}\text{N}/\text{GaN}$  heterostructure were investigated by cross-sectional scanning tunneling microscopy and selected-area electron diffraction measurements. The cross-sectional  $(10\bar{1}0)$  cleavage surface was found to exhibit height modulations in the vicinity of the  $\text{Al}_{0.81}\text{In}_{0.19}\text{N}$  layers. Three different roughness components of the height modulations were identified with correlation length of  $133 \pm 10$  nm (F1),  $39 \pm 1$  nm (F2), and  $10 \pm 1$  nm (F3). The first component gives rise to a broad height modulation that extends from the buffer layer through the  $\text{Al}_{0.81}\text{In}_{0.19}\text{N}/\text{GaN}$  layers into the capping layer. The two other roughness components were mainly detectable in the  $\text{Al}_{0.81}\text{In}_{0.19}\text{N}$  layers. Electron diffraction patterns showed a contraction (dilatation) of the  $c$  ( $a$ ) lattice constant of  $\text{Al}_{0.81}\text{In}_{0.19}\text{N}$  relative to GaN by 0.75% (0.59%). Furthermore spatial fluctuations of the  $c$  and  $a$  lattice constant were found, which could be associated with the roughness components F1 and F2, respectively. The height modulations at the cleavage surface and the local changes of the lattice constants could be assigned to strain due to compositional fluctuations. It was shown that F1 arises from alternatingly compressive and tensile strained domains, due to compositional fluctuations, relaxing at the surface. F2 and F3 were attributed to interface misfit edge dislocations, which strain primarily the  $a$  lattice constant, and surface steps, respectively.

The presence of interface misfit dislocations were also found to induce surface steps occurring on  $(10\bar{1}0)$  cleavage surfaces of  $\text{Al}_{0.80}\text{In}_{0.20}\text{N}/\text{GaN}$  DBR heterostructures. These steps appear to form at the  $\text{Al}_{0.80}\text{In}_{0.20}\text{N}/\text{GaN}$  interfaces and annihilate at the following inverted ones. The calculation of cross-covariance functions of adjacent  $\text{Al}_{0.80}\text{In}_{0.20}\text{N}$  layers indicated that the step density reaches a saturation after three pairs of  $\text{Al}_{0.80}\text{In}_{0.20}\text{N}/\text{GaN}$  layers.

The effect of In fluctuations in lattice-matched  $\text{Al}_{1-x}\text{In}_x\text{N}/\text{GaN}$  heterostructures could be directly imaged in real space. Previously the presence of In fluctuations

---

could only be inferred from large Stokes shifts, photo-reflectance, and -luminescence measurements. Moreover the expansion of the compositional fluctuations was specified and its influence on the  $c$  and  $a$  lattice constants could be shown directly. These fluctuations, in combination with the detected dislocations developing at the  $\text{Al}_{1-x}\text{In}_x\text{N}/\text{GaN}$  interfaces, may critically affect the performance of optoelectronic devices.

Furthermore, a strong contrast between  $\text{Al}_{1-x}\text{In}_x\text{N}$  and GaN was present in constant-current scanning tunneling microscopy images of the cleavage surfaces. Based on atomic force and scanning near-field optical microscopy images, and simulations of the tunnel current, the contrast between  $\text{Al}_{0.81}\text{In}_{0.19}\text{N}$  and GaN was attributed to mechanical properties of the cleavage surface. It was concluded that the height changes are due to defects and strain at the interfaces, which lead to deflections of the propagating crack tip from the intended cleavage plane during cleavage.



# Material parameters

parameter	GaN	AlN	InN
$E_g$ [eV]	3.510[37]	6.25[37]	0.78[37]
lattice constant [pm]			
$a$ at $T = 300$ K	318.9[37]	311.2[37]	354.5[37]
$c$ at $T = 300$ K	518.5[37]	498.2[37]	570.3[37]
$c/a$	1.626	1.601	1.612
effective mass			
$m_e^{\parallel}$	$0.186m_0$ [180]	$0.322m_0$ [180]	$0.065m_0$ [180]
$m_e^{\perp}$	$0.209m_0$ [180]	$0.329m_0$ [180]	$0.068m_0$ [180]
$m_{e,\text{DOS}}$	$0.201m_0$	$0.327m_0$	$0.067m_0$
$m_{HH}^{\parallel}$	$1.76m_0$ [181]	$3.68m_0$ [182]	$1.56m_0$ [181]
$m_{LH}^{\parallel}$	$1.76m_0$ [181]	$3.68m_0$ [182]	$1.56m_0$ [181]
$m_{HH}^{\perp}$	$1.69m_0$ [181]	$6.33m_0$ [182]	$1.68m_0$ [181]
$m_{LH}^{\perp}$	$0.14m_0$ [181]	$0.25m_0$ [182]	$0.11m_0$ [181]
$m_{h,\text{DOS}}$	$1.807m_0$	$5.421m_0$	$1.710m_0$
dielectric constant $\epsilon$	10.00[183]	8.5[183]	15.3[183]
electron affinity $\chi$ [eV]	2.1 – 4.26 <sup>a</sup>	< 0 – 2.16 <sup>a</sup>	4.6 – 5.8 <sup>a</sup>
donor ionization energy $E_D$ [eV]	$E_g - 0.03$ [164]	$E_g - 0.17$ [184]	$E_g - 0.05$
acceptor ionization energy $E_A$ [eV]	0.026[164]	0.5[184]	
mobility			
$\mu_n$ [cm <sup>2</sup> /Vs]	500[183]	300[183]	1200[183]
$\mu_p$ [cm <sup>2</sup> /Vs]	20[183]	14[185]	90
elastic constants [GPa]			
$C_{11}$	$390 \pm 15$ [108]	396 [109]	223 [109]
$C_{12}$	$145 \pm 20$ [108]	137 [109]	115 [109]

parameter	GaN	AlN	InN
$C_{13}$	$106 \pm 20$ [108]	108 [109]	92[109]
$C_{33}$	$398 \pm 20$ [108]	373 [109]	224[109]
$C_{44}$	$105 \pm 10$ [108]	116 [109]	48[109]
piezoelectric coefficients [ $\text{Cm}^{-2}$ ]			
$e_{33}$	0.73[186]	1.55[187]	0.97[186]
$e_{31}$	-0.49[186]	-0.58[187]	-0.57[186]
$e_{15}$	-0.40[188]	-0.48[187]	-0.57 <sup>b</sup>
spontaneous polarization [ $\text{Cm}^{-2}$ ]			
$P_{sp}$	-0.029[186]	-0.081[186]	-0.032[186]

**Table 9.1:** Material parameters for wurtzite structure GaN, AlN and InN used for tunnel-current simulations and finite element modeling calculations.

<sup>a</sup>For references cf. Chap. 5 "About the electron affinity".

<sup>b</sup>The value of  $e_{15}$  given in Ref. [186] is set identical to that of  $e_{31}$  by Ref. [189].

# Bibliography

- [1] G. Busch. Early history of the physics and chemistry of semiconductors - from doubts to facts in a hundred years. *Eur. J. Phys.*, 10:254–264, 1989.
- [2] A. Volta. Del modo di render sensibilissima la più debole electtricità sia naturale, sia artificiale. *Phil. Trans. R. Soc.*, 72:237, 1782.
- [3] J. Weiss. *Experimentelle Beiträge zur Elektronentheorie aus dem Gebiet der Thermoelktrizität*. PhD thesis, Albert-Ludwigs Universität, Freiburg im Breisgau, 1910.
- [4] M. Faraday. On a new law of electric conduction. *Phil. Trans. R. Soc.*, 123:507, 1833.
- [5] J. W. Hittorf. Ueber das elektrische Leitungsvermögen des Schwefelsilbers und des Halbschwefelkupfers. *Ann. Phys. Lpz.*, 84:1–28, 1851.
- [6] A. H. Wilson. The Theory of Electronic Semiconductors I. *Proc. R. Soc. A*, 133:458, 1931.
- [7] A. H. Wilson. The Theory of Electronic Semiconductors II. *Proc. R. Soc. A*, 134:277, 1931.
- [8] T. Jenkins. A brief history of ... semiconductors. *Phys. Educ.*, 40(5):430, 2005.
- [9] L. Łukasiak and A. Jakubowski. History of Semiconductors. *JTIT*, 1:3–9, 2010.
- [10] R. Hilsch and R. W. Pohl. Steuerung von Elektronenströmen mit einem Dreielektrodenkristall und ein Modell einer Sperrschicht. *Z. Phys.*, 111(5):399–408, 1938.

- [11] L. Esaki. Discovery of the tunnel diode. *IEEE Trans. Electron Dev.*, 23(7):644–647, 1976.
- [12] Zh. I. Alferov. The history and future of semiconductor heterostructures. *Semiconductors*, 32(1):1–14, 1998.
- [13] D. W. Runton, B. Trabert, J. B. Shearly, and R. Vetry. History of GaN. *IEEE Microwave Magazine*, 14(3):82, 2013.
- [14] P. Gibart. Metal organic vapour phase epitaxy of GaN and lateral overgrowth. *Reports on Progress in Physics*, 67(5):667–715, 2004.
- [15] R. Butté, J.-F. Carlin, E. Feltin, M. Gonschorek, S. Nicolay, G. Christmann, D. Simeonov, A. Castiglia, J. Dorsaz, H. J. Buehlmann, S. Christopoulos, G. Baldassarri Höger von Högersthal, A. J. D. Grundy, M. Mosca, C. Pinquier, M. A. Py, F. Demangeot, J. Frandon, P. G. Lagoudakis, J. J. Baumberg, and N. Grandjean. Current status of AlInN layers lattice-matched to GaN for photonics and electronics. *J. Phys. D: Appl. Phys.*, 40:6328–6344, 2007.
- [16] M. Gonschorek, J.-F. Carlin, E. Feltin, M. A. Py, N. Grandjean, V. Darakchieva, B. Monemar, M. Lorenz, and G. Ramm. Two-dimensional electron gas density in  $\text{Al}_{1-x}\text{In}_x\text{N}/\text{AlN}/\text{GaN}$  heterostructures ( $0.03 \leq x \leq 0.23$ ). *J. Appl. Phys.*, 103:093714, 2008.
- [17] R. Butté, E. Feltin, J. Dorsaz, G. Christmann, J.-F. Carlin, N. Grandjean, and M. Ilegems. Recent Progress in the Growth of Highly Reflective Nitride-Based Distributed Bragg Reflectors and Their Use in Microcavities. *Jpn. J. Appl. Phys.*, 44(10):7207–7216, 2005.
- [18] E. Feltin, R. Butté, J.-F. Carlin, J. Dorsaz, N. Grandjean, and M. Ilegems. Lattice-matched distributed Bragg reflectors for nitride-based vertical cavity surface emitting lasers. *Electron. Lett.*, 41(2):94, 2005.
- [19] G. Cosendey, J.-F. Carlin, N. A. K. Kaufmann, R. Butté, and N. Grandjean. Strain compensation in AlInN/GaN multilayers on GaN substrate: Application to the realization of defect-free Bragg reflectors. *Appl. Phys. Lett.*, 98:181111, 2011.

- 
- [20] K. E. Waldrip, J. Han, J. J. Figiel, H. Zhou, E. Makarona, and A. V. Nurmiikko. Stress engineering during metalorganic chemical vapor deposition of AlGa<sub>N</sub>/Ga<sub>N</sub> distributed Bragg reflectors. *Appl. Phys. Lett.*, 78(21):3205, 2001.
- [21] J.-F. Carlin and M. Ilegems. High-quality AlInN for high index contrast Bragg mirrors lattice matched to GaN. *Appl. Phys. Lett.*, 83(4):668–670, 2003.
- [22] L. Vegard. Die Konstitution der Mischkristalle und die Raumfüllung der Atome. *Z. Phys.*, 5:17, 1921.
- [23] J.-F. Carlin, J. Dorsaz, E. Feltin, R. Butté, N. Grandjean, M. Ilegems, and M. Laügt. Crack-free fully epitaxial nitride microcavity using highly reflective AlInN/GaN Bragg mirrors. *Appl. Phys. Lett.*, 86:031107, 2005.
- [24] J. Dorsaz, J.-F. Carlin, S. Gradecak, and M. Ilegems. Progress in AlInN-GaN Bragg reflectors: Application to a microcavity light emitting diode. *J. Appl. Phys.*, 97:084505, 2005.
- [25] S. Nicolay, J.-F. Carlin, E. Feltin, R. Butté, M. Mosca, N. Grandjean, M. Ilegems, M. Tchernycheva, L. Nevou, and F. H. Julien. Midinfrared inter-subband absorption in lattice-matched AlInN/GaN multiple quantum wells. *Appl. Phys. Lett.*, 87:111106, 2005.
- [26] E. Feltin, J.-F. Carlin, J. Dorsaz, G. Christmann, and R. Butté. Crack-free highly reflective AlInN/AlGa<sub>N</sub> Bragg mirrors for UV applications. *Appl. Phys. Lett.*, 88(5):051108, 2006.
- [27] G. Christmann, D. Simeonov, R. Butté, E. Feltin, J.-F. Carlin, and N. Grandjean. Impact of disorder on high quality factor III-V nitride microcavities. *Appl. Phys. Lett.*, 89:261101, 2006.
- [28] G. Christmann, R. Butté, E. Feltin, J.-F. Carlin, and N. Grandjean. Room temperature polariton lasing in a GaN/AlGa<sub>N</sub> multiple quantum well microcavity. *Appl. Phys. Lett.*, 93(5):051102, 2008.
- [29] T. Someya, R. Werner, A. Forchel, M. Catalano, R. Cingolani, and Y. Arakawa. Room Temperature Lasing at Blue Wavelengths in Gallium Nitride Microcavities. *Science*, 285:1905, 1999.

- [30] Y. Higuchi, K. Omae, H. Matsumura, and T. Mukai. Room-Temperature CW Lasing of a GaN-Based Vertical-Cavity Surface-Emitting Laser by Current Injection. *Appl. Phys. Express*, 1:121102, 2008.
- [31] K. Omae, Y. Higuchi, K. Nakagawa, H. Matsumura, and T. Mukai. Improvement in Lasing Characteristics of GaN-based Vertical-Cavity Surface-Emitting Lasers Fabricated Using a GaN Substrate. *Appl. Phys. Express*, 2:052101, 2009.
- [32] T.-C. Lu, S.-W. Chen, T.-T. Wu, P.-M. Tu, C.-K. Chen, C.-H. Chen, Z.-Y. Li, H.-C. Kuo, and S.-C. Wang. Continuous wave operation of current injected GaN vertical cavity surface emitting lasers at room temperature. *Appl. Phys. Lett.*, 97:071114, 2010.
- [33] E. Feltin, G. Christmann, J. Dorsaz, A. Castiglia, J.-F. Carlin, R. Butté, N. Grandjean, S. Christopoulos, G. Baldassarri Höger von Högersthal, A. J. D. Grundy, P. G. Lagoudakis, and J. J. Baumberg. Blue lasing at room temperature in an optically pumped lattice-matched AlInN=GaN VCSEL structure. *Electron. Lett.*, 43(17):924–926, 2007.
- [34] S. Nakamura. The Roles of Structural Imperfections in InGaN-Based Blue Light-Emitting Diodes and Laser Diodes. *Science*, 281:956, 1998.
- [35] M. Asif Khan, A. Bhattarai, J. N. Kuznia, and D. T. Olson. High electron mobility transistor based on a GaN-Al<sub>x</sub>Ga<sub>1-x</sub>N heterojunction. *Appl. Phys. Lett.*, 63(9):1214–1215, 1993.
- [36] Y.-F. Wu, A. Saxler, M. Moore, R. P. Smith, S. Sheppard, P. M. Chavarkar, T. Wisleder, U. K. Mishra, and P. Parikh. 30-W/mm GaN HEMTs by field plate optimization. *IEEE Electron Device Lett.*, 25(3):117–119, 2004.
- [37] I. Vurgaftman and J. R. Meyer. Band parameters for nitrogen-containing semiconductors. *J. Appl. Phys.*, 94(6):3675–3696, 2003.
- [38] Y. Taniyasu, J.-F. Carlin, A. Castiglia, R. Butté, and N. Grandjean. Mg doping for *p*-type AlInN lattice-matched to GaN. *Appl. Phys. Lett.*, 101(8):082113, 2012.

- 
- [39] S. Marcinkevičius, V. Liuolia, D. Billingsley, M. Shatalov, J. Yang, R. Gaska, and M. S. Shur. Transient photoreflectance of AlInN/GaN heterostructures. *AIP Advances*, 2(4):042148, 2012.
- [40] S. Yamaguchi, M. Kariya, S. Nitta, T. Takeuchi, C. Wetzel, H. Amano, and I. Akasaki. Anomalous features in the optical properties of Al<sub>1-x</sub>In<sub>x</sub>N on GaN grown by metal organic vapor phase epitaxy. *Appl. Phys. Lett.*, 76(7):876–878, 2000.
- [41] V. Liuolia, S. Marcinkevičius, D. Billingsley, M. Shatalov, J. Yang, R. Gaska, and M. S. Shur. Photoexcited carrier dynamics in AlInN/GaN heterostructures. *Appl. Phys. Lett.*, 100(24):242104, 2012.
- [42] I. Gorczyca, S. P. Łepkowski, T. Suski, N. E. Christensen, and A. Svane. Influence of indium clustering on the band structure of semiconducting ternary and quaternary nitride alloys. *Phys. Rev. B*, 80(7):075202, 2009.
- [43] A. Teke, S. Gökden, R. Tülek, J. H. Leach, Q. Fan, J. Xie, Ü. Özgür, H. Morkoç, S. B. Lisesivdin, and E. Özbay. The effect of AlN interlayer thicknesses on scattering processes in lattice-matched AlInN/GaN two-dimensional electron gas heterostructures. *New J. Phys.*, 11:063031, 2009.
- [44] Th. Kehagias, G. P. Dimitrakopoulos, J. Kioseoglou, H. Kirmse, C. Giesen, M. Heuken, A. Georgakilas, W. Neumann, Th. Karakostas, and Ph. Komninou. Indium migration paths in V-defects of InAlN grown by metal-organic vapor phase epitaxy. *Appl. Phys. Lett.*, 95(7):071905, 2009.
- [45] Th. Kehagias, G. P. Dimitrakopoulos, J. Kioseoglou, H. Kirmse, C. Giesen, M. Heuken, A. Georgakilas, W. Neumann, Th. Karakostas, and Ph. Komninou. Erratum: Indium migration paths in V-defects of InAlN grown by metal-organic vapor phase epitaxy. *Appl. Phys. Lett.*, 99(5):059902, 2011.
- [46] A. Mouti, J.-L. Rouvière, M. Cantoni, J.-F. Carlin, E. Feltn, N. Grandjean, and P. Stadelmann. Stress-modulated composition in the vicinity of dislocations in nearly lattice matched Al<sub>x</sub>In<sub>1-x</sub>N/GaN heterostructures: A possible explanation of defect insensitivity. *Phys. Rev. B*, 83(19):195309, 2011.

- [47] Q. Y. Wei, T. Li, Y. Huang, Z. T. Chen, T. Egawa, and F. A. Ponce. Compositional instability in InAlN/GaN lattice-matched epitaxi. *Appl. Phys. Lett.*, 100(9):092101, 2012.
- [48] G. Perillat-Merceroz, G. Cosendey, J.-F. Carlin, R. Butté, and N. Grandjean. Intrinsic degradation mechanism of nearly lattice-matched InAlN layers grown on GaN substrates. *J. Appl. Phys.*, 113(6):063506, 2013.
- [49] T. Kajima, A. Kobayashi, K. Ueno, K. Shimomoto, T. Fujii, J. Ohta, H. Fujioka, and M. Oshima. Room-Temperature Epitaxial Growth of High-Quality *m*-Plane InAlN Films on Nearly Lattice-Matched ZnO Substrates. *Jap. J. Appl. Phys.*, 49(7R):070202, 2010.
- [50] M. R. Laskar, T. Ganguli, A. A. Rahman, A. Arora, N. Hatui, M. R. Gokhale, S. Ghosh, and A. Bhattacharya. Anisotropic structural and optical properties of *a*-plane (11 $\bar{2}$ 0) AlInN nearly-lattice-matched to GaN. *Appl. Phys. Lett.*, 98(18):181108, 2011.
- [51] C. Durand, C. Bougerol, J.-F. Carlin, G. Rossbach, F. Godel, J. Eymery, P.-H. Jouneau, A. Mukhtarova, R. Butté, and N. Grandjean. *M*-Plane GaN/InAlN Multiple Quantum Wells in Core-Shell Wire Structure for UV Emission. *ACS Photonics*, 1(1):38–46, 2014.
- [52] E. R. Buß, P. Horenburg, U. Rossow, H. Bremers, T. Meisch, M. Caliebe, F. Scholz, and A. Hangleiter. Non- and semipolar AlInN one-dimensionally lattice-matched to GaN for realization of relaxed buffer layers for strain engineering in optically active GaN-based devices. *phys. stat. sol. (b)*, 253(1):84–92, 2016.
- [53] P. Waltereit, O. Brandt, A. Trampert, H. T. Grahn, J. Menniger, M. Ramsteiner, M. Reiche, and K. H. Ploog. Nitride semiconductors free of electrostatic fields for efficient white light-emitting diodes. *Nature*, 406(6798):865–868, aug 2000.
- [54] C. G. Van de Walle and D. Segev. Microscopic origins of surface states on nitride surfaces. *J. Appl. Phys.*, 101(8):081704, 2007.

- 
- [55] L. Lymperakis and J. Neugebauer. Large anisotropic adatom kinetics on nonpolar GaN surfaces: Consequences for surface morphologies and nanowire growth. *Phys. Rev. B*, 79(24):241308, Jun 2009.
- [56] G. Binnig, H. Rohrer, Ch. Gerber, and E. Weibel. Tunneling through a controllable vacuum gap. *Appl. Phys. Lett.*, 40(2):178–181, 1982.
- [57] G. Binnig, H. Rohrer, Ch. Gerber, and E. Weibel. Surface Studies by Scanning Tunneling Microscopy. *Phys. Rev. Lett.*, 49:57–61, 1982.
- [58] G. Binnig and H. Rohrer. Scanning tunneling Microscopy. *Surf. Sci.*, 126:236–244, 1983.
- [59] J. Tersoff and D. R. Hamann. Theory of the scanning tunneling microscope. *Phys. Rev. B*, 31:805–813, Jan 1985.
- [60] F. Schwabl. *Quantum Mechanics*. Springer, 4th edition edition, 2007.
- [61] W. Nolting. *Grundkurs Theoretische Physik 5/1*. Springer, 7 edition, 2009.
- [62] J. Bardeen. Tunnelling from a many-particle point of view. *Phys. Rev. Lett.*, 6(2):57–59, 1961.
- [63] J. Tersoff and D. R. Hamann. Theory and Application for the Scanning Tunneling Microscope. *Phys. Rev. Lett.*, 50:1998–2001, Jun 1983.
- [64] A. D. Gottlieb and L. Wesoloski. Bardeen’s tunnelling theory as applied to scanning tunnelling microscopy: a technical guide to the traditional interpretation. *Nanotechnol.*, 17(8):R57, 2006.
- [65] P.A.M. Dirac. The question theory of the emission and absorption of radiation. *Proceedings of the Royal Society of London Series A*, 114(767):243–265, 1927.
- [66] G. Wentzel. Über strahlungslose Quantensprünge. *Zeitschrift für Physik*, 43:524–530, 1927.
- [67] R. J. Hamers. Methods of Tunneling Spectroscopy with the STM. In D. A. Bonnell, editor, *Scanning Tunneling Microscopy and Spectroscopy: Theory, Techniques, and Applications*, chapter 4, pages 51–103. VCH Publishers, Inc., 1993.

- [68] B. Voigtländer. *Scanning Probe Microscopy: Atomic Force Microscopy and Scanning Tunneling Microscopy*. Nanoscience and Technology. Springer, 2015.
- [69] M. Schnedler, V. Portz, P. H. Weidlich, R. E. Dunin-Borkowski, and Ph. Ebert. Quantitative description of photoexcited scanning tunneling spectroscopy and its application to the GaAs(110) surface. *Phys. Rev. B*, 91:235305, Jun 2015.
- [70] R. M. Feenstra, Y. Dong, M. P. Semtsiv, and W. T. Masselink. Influence of Tip-induced Band Bending on Tunneling Spectra of Semiconductor Surfaces. *Nanotechnol.*, 18:044015, 2007.
- [71] R. M. Feenstra and J. A. Stroscio. Tunneling spectroscopy of the GaAs(110) surface. *J. Vac. Sci. Technol. B*, 5(4):923–929, 1987.
- [72] R. Seiwatz and M. Green. Space Charge Calculations for Semiconductors. *J. Appl. Phys.*, 29:1034–1040, 1958.
- [73] S. M. Sze and Kwok K. Ng. *Physics of Semiconductor Devices*. Wiley-Interscience, New York, 3 edition, 2007.
- [74] R. A. Smith. *Semiconductors*. Cambridge University Press, Cambridge, 1959.
- [75] E. F. Schubert. *Light-Emitting Diodes*. Cambridge University Press, 2003.
- [76] D. Z. Garbuzov. Reradiation effects, lifetimes and probabilities of band-to-band transitions in direct  $A_3B_5$  compounds of GaAs type. *J. Lumin.*, 27(1):109–112, 1982.
- [77] S. Selberherr. *Analysis and Simulation of Semiconductor Devices*. Springer, Vienna, New York, 1984.
- [78] M. Schnedler, R. E. Dunin-Borkowski, and Ph. Ebert. Importance of quantum correction for the quantitative simulation of photoexcited scanning tunneling spectra of semiconductor surfaces. *Phys. Rev. B*, 93:195444, May 2016.
- [79] J. Bono and R. H. Good. Theoretical discussion of the scanning tunneling microscope applied to a semiconductor surface. *Surf. Sci.*, 175(2):415–420, 1986.

- 
- [80] J. G. Simmons. Generalized Formula for the Electric Tunnel Effect between Similar Electrodes Separated by a Thin Insulating Film. *J. Appl. Phys.*, 34(6):1793–1803, 1963.
- [81] M. Schnedler. *Quantitative scanning tunneling spectroscopy of non-polar compound semiconductor surfaces*. PhD thesis, RWTH Aachen University, 2015.
- [82] F. L. Deepak, A. Mayoral, and R. Arenal, editors. *Advanced Transmission Electron Microscopy - Applications to Nanomaterials*. Springer-Verlag, 2015.
- [83] J. Thomas and T. Gemming, editors. *Analytical Transmission Electron Microscopy - An Introduction for Operators*. Springer-Verlag, 2014.
- [84] W. L. Bragg. The Specular Reflection of X-rays. *Nature*, 90(2250):410, 1912.
- [85] F. C. Frank. On Miller-Bravais Indices and four-dimensional Vectors. *Acta Cryst.*, 18(5):862–866, 1964.
- [86] H. M. Otte and A. G. Crocker. Crystallographic Formulae for Hexagonal Lattices. *phys. stat. sol. (b)*, 9(2):441–450, 1965.
- [87] D. B. Williams and C. B. Carter. *Transmission electron microscopy II Diffraction*. A Division of Plenum Publishing Corporation, 1996.
- [88] L. Weber. Das viergliedrige Zonensymbol des hexagonalen Systems. *Z. Kristallographie*, 57:200, 1922.
- [89] Q. Fan. A new method of calculating interplanar spacing: the position-factor method. *J. Appl. Cryst.*, 45:1303–1308, 2012.
- [90] C. L. Jia, M. Lentzen, and K. Urban. Atomic-Resolution Imaging of Oxygen in Perovskite Ceramics. *Science*, 299(5608):870–873, 2003.
- [91] M. de la Mata, C. Magen, J. Gazquez, M. I. B. Utama, M. Heiss, S. Lopatin, F. Furtmayr, C. J. Fernández-Rojas, B. Peng, J. R. Morante, R. Rurali, M. Eickhoff, A. Fontcuberta i Morral, Q. Xiong, and J. Arbiol. Polarity Assignment in ZnTe, GaAs, ZnO, and GaN-AlN Nanowires from Direct Dumbbell Analysis. *Nano Lett.*, 12(5):2579–2586, 2012.
- [92] S. Kikuchi. Diffraction of Cathode Rays by Mica. *Proc. Imp. Acad*, 4(6):271–271, 1928.

- [93] P. R. Okamoto, E. Levine, and G. Thomas. Kikuchi Maps for hcp and bcc Crystals. *J. Appl. Phys.*, 38(1):289, 1967.
- [94] UM Saint Louis. Gallium Nitride (GaN) Kikuchi map.
- [95] T. Lindeberg. *Discrete Scale-Space Theory and the Scale-Space Primal Sketch*. PhD thesis, Stockholm University - Royal Institute of Technology - Stockholm, Sweden, May 1991.
- [96] I. N. Bronstein, K. A. Semendjajew, G. Musiol, and H. Mühlig. *Taschenbuch der Mathematik*. Verlag Europa-Lehrmittel, 9. edition, 2013.
- [97] S. K. Kulkarni. *Nanotechnology: Principles and Practices*. Capital Publishing Company and Springer, 3rd edition, 2015.
- [98] S. Bensmann, F. Gaußmann, M. Lewin, J. Wüppen, S. Nyga, C. Janzen, B. Jungbluth, and T. Taubner. Near-field imaging and spectroscopy of locally strained GaN using an IR broadband laser. *Opt. Express*, 22(19):22369–22381, 2014.
- [99] T. Taubner, R. Hillenbrand, and F. Keilmann. Nanoscale polymer recognition by spectral signature in scattering infrared near-field microscopy. *Appl. Phys. Lett.*, 85(21):5064, 2004.
- [100] A. J. Huber, J. Wittborn, and R. Hillenbrand. Infrared spectroscopic near-field mapping of single nanotransistors. *Nanotechnol.*, 21(23):235702, 2010.
- [101] M. Brehm, T. Taubner, R. Hilenbrand, and F. Keilmann. Infrared Spectroscopic Mapping of Single Manoparticles and Viruses at Nanoscale Resolution. *Nano Lett.*, 6(7):1307, 2006.
- [102] A. Cvitkovic, N. Ocelic, and R. Hillenbrand. Material-Specific Infrared Recognition of Single Sub-10 nm Particles by Substrate-Enhanced-Scattering-Type Near-Field Microscopy. *Nano Lett.*, 7(10):3177, 2007.
- [103] T. Taubner, R. Hillenbrand, and F. Keilmann. Performance of visible and mid-infrared scattering-type near-field optical microscopes. *J. Microsc.*, 210(3):311, 2003.

- 
- [104] A. J. Huber, A. Ziegler, T. Köck, and R. Hillenbrand. Infrared nanoscopy of strained semiconductors. *Nat. Nanotechnol.*, 4(3):153, 2009.
- [105] A. M. Gigler, A. J. Huber, M. Bauer, A. Ziegler, and R. Hillenbrand. Nanoscale residual stress-field mapping around nanoindentations in SiC by IR s-SNOM and confocal Raman microscopy. *Opt. Express*, 17(25):22351, 2009.
- [106] Y. Sun, S. E. Thompson, and T. Nishida. *Strain Effect in Semiconductors: Theory and Device Applications*. Springer Science+Business Media, 2010.
- [107] A.E. Romanov, T.J. Baker, S. Nakamura, J.S. Speck, and A.E. Romanov. Strain-induced polarization in wurtzite III-nitride semipolar layers. *J. Appl. Phys.*, 100(2):701–706, 2006.
- [108] A. Polian, M. Grimsditch, and I. Grzegory. Elastic constants of gallium nitride. *J. Appl. Phys.*, 79(6):3343–3344, 1996.
- [109] A. F. Wright. Elastic properties of zinc-blende and wurtzite AlN, GaN, and InN. *J. Appl. Phys.*, 82:2833, 1997.
- [110] F. Bernardini and V. Fiorentini. Spontaneous versus Piezoelectric Polarization in III-V Nitrides: Conceptual Aspects and Practical Consequences. *phys. stat. sol. (b)*, 216:391, 1999.
- [111] S.-H. Park and S.-L. Chuang. Crystal-orientation effects on the piezoelectric field and electronic properties of strained wurtzite semiconductors. *Phys. Rev. B*, 59(7):4725, 1999.
- [112] J. M. Bennett and L. Mattsson. *Introduction to Surface Roughness and Scattering*. Optical Society of America, Washington, D.C., second edition, 1999.
- [113] R. M. Feenstra, D. A. Collins, D. Z.-Y.-Ting, M. W. Wang, and T. C. McGill. Interface Roughness and Asymmetry in InAs/GaSb Superlattices Studied by Scanning Tunneling Microscopy. *Phys. Rev. Lett.*, 72(17):2749, 1994.
- [114] N. D. Jäger, K. Urban, E. R. Weber, and Ph. Ebert. Dopant atom clustering and charge screening induced roughness of electronic interfaces in GaAs *p-n* multilayers. *Phys. Rev. B*, 65:235302, May 2002.

- [115] J. P. Ibe, P. P. Bey, S. L. Brandow, R. A. Brizzolara, N. A. Burnham, D. P. DiLella, K. P. Lee, C. R. K. Marrian, and R. J. Colton. On the electrochemical etching of tips for scanning tunneling microscopy. *J. Vac. Sci. Technol. A*, 8(4):3570–3575, 1990.
- [116] K. H. Graf. private communication.
- [117] Ph. Ebert. Untersuchungen der InP(110)-Oberfläche mit dem Rastertunnelmikroskop. Diplomarbeit, RWTH Aachen, 1990.
- [118] Ph. Ebert and K. Szot. Scanning Probe Analysis. In R. Waser, editor, *Nanoelectronics and Information Technology*, chapter 11, pages 255–281. Wiley-VCH, Weinheim, 3 edition, 2012.
- [119] J. Wueppen, B. Jungbluth, T. Taubner, and P. Loosen. Ultrafast tunable mid IR source. In *Infrared, Millimeter and Terahertz Waves (IRMMW-THz), 2011 36th International Conference on*, pages 1–2, Oct 2011.
- [120] L. Ivanova, S. Borisova, H. Eisele, M. Dähne, A. Laubsch, and Ph. Ebert. Surface states and origin of the Fermi level pinning on nonpolar GaN(100) surfaces. *Appl. Phys. Lett.*, 93(19):192110, 2008.
- [121] M. Bertelli, P. Löptien, M. Wenderoth, A. Rizzi, R. G. Ulbrich, M. C. Righi, A. Ferretti, L. Martin-Samos, C. M. Bertoni, and A. Catellani. Atomic and electronic structure of the nonpolar GaN(1 $\bar{1}$ 00) surface. *Phys. Rev. B*, 80(11):115324, 9 2009.
- [122] Ph. Ebert, S. Schaafhausen, A. Lenz, A. Sabitova, L. Ivanova, M. Dähne, Y.-L. Hong, S. Gwo, and H. Eisele. Direct measurement of the band gap and Fermi level position at InN (11 $\bar{2}$ 0). *Appl. Phys. Lett.*, 98(6):062103, 2011.
- [123] L. Lymperakis, P. H. Weidlich, H. Eisele, M. Schnedler, J.-P. Nys, B. Grandidier, D. Stievenard, R. E. Dunin-Borkowski, J. Neugebauer, and Ph. Ebert. Hidden surface states at non-polar GaN (10 $\bar{1}$ 0) facets: Intrinsic pinning of nanowires. *Appl. Phys. Lett.*, 103(15):152101, 2013.
- [124] M. Schnedler, V. Portz, H. Eisele, R. E. Dunin-Borkowski, and Ph. Ebert. Polarity-dependent pinning of a surface state. *Phys. Rev. B*, 91:205309, May 2015.

- 
- [125] G. Kresse and J. Furthmüller. Efficient iterative schemes for *ab initio* total-energy calculations using a plane-wave basis set. *Phys. Rev. B*, 54:11169–11186, Oct 1996.
- [126] G. Kresse and J. Hafner. Ab initio molecular dynamics for liquid metals. *Phys. Rev. B*, 47(1):558–561, January 1993.
- [127] S. Schulz, M. A. Caro, L.-T. Tan, P. J. Parbrook, R. W. Martin, and E. P. O’Reilly. Composition-Dependent Band Gap and Band-Edge Bowing in AlInN: A Combined Theoretical and Experimental Study. *Appl. Phys. Express*, 6:121001, 2013.
- [128] M. S. Miao, A. Janotti, and C. G. Van de Walle. Reconstructions and origin of surface states on AlN polar and nonpolar surfaces. *Phys. Rev. B*, 80(15):155319, Oct 2009.
- [129] E. Sakalauskas, H. Behmenburg, C. Hums, P. Schley, G. Rossbach, C. Giesen, M. Heuken, H. Kalisch, R. H. Jansen, J. Bläsing, A. Dadgar, A. Krost, and R. Goldhahn. Dielectric function and optical properties of Al-rich AlInN alloys pseudomorphically grown on GaN. *J. Phys. D: Appl. Phys.*, 43:365102, 2010.
- [130] J. I. Pankove and H. Schade. Photoemission from GaN. *Appl. Phys. Lett.*, 25(1):53, 1974.
- [131] M. C. Benjamin, Cheng Wang, R. F. Davis, and R. J. Nemanich. Observation of a negative electron affinity for heteroepitaxial AlN on  $\alpha$ (6H)-SiC(0001). *Appl. Phys. Lett.*, 64(24):3288–3290, 1994.
- [132] J. Wu, W. Walukiewicz, S. X. Li, R. Armitage, J. C. Ho, E. R. Weber, E. E. Haller, Hai Lu, William J. Schaff, A. Barcz, and R. Jakiela. Effects of electron concentration on the optical absorption edge of InN. *Appl. Phys. Lett.*, 84(15):2805–2807, 2004.
- [133] P. Hacke, T. Detchprohm, K. Hiramatsu, and N. Sawaki. Schottky barrier on *n*-type GaN grown by hydride vapor phase epitaxy. *Appl. Phys. Lett.*, 63(19):2676, 1993.

- [134] V. M. Bermudez, T. M. Jung, K. Doverspike, and A. E. Wickenden. The growth and properties of Al and AlN films on GaN(0001)-(1 × 1). *J. Appl. Phys.*, 79(1):110, 1996.
- [135] S. X. Li, K. M. Yu, J. Wu, R. E. Jones, W. Walukiewicz, J. W. Ager, W. Shan, E. E. Haller, Hai Lu, and William J. Schaff. Fermi-level stabilization energy in group III nitrides. *Phys. Rev. B*, 71:161201, Apr 2005.
- [136] C. I. Wu, A. Kahn, E. S. Hellman, and D. N. E. Buchanan. Electron affinity at aluminum nitride surfaces. *Appl. Phys. Lett.*, 73(10):1346, 1998.
- [137] C.-L. Wu, H.-M. Lee, C.-T. Kuo, C.-H. Chen, and S. Gwo. Cross-sectional scanning photoelectron microscopy and spectroscopy of wurzite InN/GaN heterojunction: Measurement of "intrinsic" band lineup. *Appl. Phys. Lett.*, 92(16):162106, 2008.
- [138] E. V. Kalinina, N. I. Kuznetsov, V. A. Dimitriev, K. G. Irvine, and C. H. Carter JR. Schottky Barriers on n-GaN Grown on SiC. *J. Elec. Mat.*, 25(5):831, 1996.
- [139] C. I. Wu and A. Kahn. Electronic states at aluminium nitride (0001)-1 × 1 surface. *Appl. Phys. Lett.*, 74(4):546, 1999.
- [140] N. Spyropoulos-Antonakakis, E. Sarantopoutou, Z. Kollia, G. Dražić, and S. Kobe. Schottky and charge memory effects in InN nanodomains. *Appl. Phys. Lett.*, 99(15):153110, 2011.
- [141] V. M. Bermudez. Study of oxygen chemisorption on the GaN(0001)-(1 × 1) surface. *J. Appl. Phys.*, 80(2):1190, 1996.
- [142] V. M. Bermudez, C.-I. Wu, and A. Kahn. AlN films on GaN: Sources of error in the photoemission measurement of electron affinity. *J. Appl. Phys.*, 89(3):1991, 2001.
- [143] S.-C. Lin, C.-T. Kuo, X. Liu, L.-Y. Liang, C.-H. Cheng, C.-H. Lin, S.-J. Tang, L.-Y. Chang, C.-H. Chen, and S. Gwo. Experimental Determination of Electron Affinities for InN and GaN Polar Surfaces. *Appl. Phys. Express*, 5:031003, 2012.

- 
- [144] C. I. Wu and A. Kahn. Investigation of the chemistry and electronic properties of metal/gallium nitride interfaces. *J. Vac. Sci. Technol. B*, 16(4):2218, 1998.
- [145] C. I. Wu, A. Kahn, N. Taskar, D. Dorman, and D. Gallagher. GaN (0001)-(1×1) surface: Composition and electronic properties. *J. Appl. Phys.*, 83(8):4249, 1998.
- [146] S. P. Grabowski, M. Schneider, H. Nienhaus, W. Mönch, R. Dimitrov, O. Ambacher, and M. Stutzmann. Electron affinity of  $\text{Al}_x\text{Ga}_{1-x}\text{N}$ (0001) surfaces. *Appl. Phys. Lett.*, 78(17):2503–2505, 2001.
- [147] R. Y. Korotkov, J. M. Gregie, and B. W. Wessels. Optical properties of the deep Mn acceptor in GaN:Mn. *Appl. Phys. Lett.*, 80(10):1731, 2002.
- [148] K. M. Tracy, W. J. Mecouch, R. F. Davis., and R. J. Nemanich. Preparation and characterization of atomically clean, stoichiometric surfaces of *n*- and *p*-type GaN(0001). *J. Appl. Phys.*, 94:3163, 2003.
- [149] P. G. Moses, M. Miao, Q. Yan, and C. G. Van de Walle. Hybrid functional investigations of band gaps and band alignments for AlN, GaN, InN, and InGaN. *J. Chem. Phys.*, 134(8):084703, 2011.
- [150] J. S. Escher. NEA Semiconductor Photoemitters. In R. K. Willardson and A. C. Beer, editors, *Semiconductors and Semimetals*, volume 15 Contacts, Junctions, Emitters, chapter 3, pages 195–300. Academic Pres, Inc., 111 Fifth Avenue. New York, New York 10003, 1981.
- [151] A. Nussbaum. The Theory of Semiconducting Junctions. In R. K. Willardson and A. C. Beer, editors, *Semiconductors and Semimetals*, volume 15 Contacts, Junctions, Emitters, chapter 2, pages 39–194. Academic Pres, Inc., 111 Fifth Avenue. New York, New York 10003, 1981.
- [152] J. Wu, W. Walukiewicz, K. M. Yu, W. Shan, J. W. Ager, E. E. Haller, Hai Lu, William J. Schaff, W. K. Metzger, and Sarah Kurtz. Superior radiation resistance of  $\text{In}_{1-x}\text{Ga}_x\text{N}$  alloys: Full-solar-spectrum photovoltaic material system. *J. Appl. Phys.*, 94(10):6477–6482, 2003.

- [153] W. Walukiewicz. Fermi level dependent native defect formation: Consequences for metal-semiconductor and semiconductor-semiconductor interfaces. *J. Vac. Sci. Technol. B*, 6(4):1257, 1988.
- [154] W. Walukiewicz. Intrinsic limitations to the doping of wide-gap semiconductors. *Physica B*, 302-303:123, 2001.
- [155] G. Martin, A. Botchkarev, A. Rockett, and H. Morkoç. Valence-band discontinuities of wurtzite GaN, AlN, and InN heterojunctions measured by x-ray photoemission spectroscopy. *Appl. Phys. Lett.*, 68(18):2541, 1996.
- [156] C.-T. Kuo, S.-C. Lin, K.-K. Chang, H.-W. Shiu, L.-Y. Chang, C.-H. Chen, S.-J. Tang, and S. Gwo. Is electron accumulation universal at InN polar surfaces? *Appl. Phys. Lett.*, 98:052101, 2011.
- [157] A. R. Smith, R. M. Feenstra, D. W. Greve, J. Neugebauer, and J. E. Northrup. Reconstructions of the GaN(000 $\bar{1}$ ) Surface. *Phys. Rev. Lett.*, 79:3934–3937, Nov 1997.
- [158] D. Segev and C. G. Van de Walle. Origins of Fermi-level pinning on GaN and InN polar and nonpolar surfaces. *Europhys. Lett.*, 76(2):305–311, 2006.
- [159] S. S. Dhesi, C. B. Stagarescu, K. E. Smith, D. Doppalapudi, R. Singh, and T. D. Moustakas. Surface and bulk electronic structure of thin-film wurtzite GaN. *Phys. Rev. B*, 56:10271–10275, Oct 1997.
- [160] K. Prabhakaran, T. G. Andersson, and K. Nozawa. Nature of native oxide on GaN surface and its reaction with Al. *Appl. Phys. Lett.*, 69(21):3212–3214, 1996.
- [161] C.I. Wu and A. Kahn. Negative electron affinity and electron emission at cesiated GaN and AlN surfaces. *Appl. Surf. Sci.*, 162-163:250–255, 2000.
- [162] P. Lorenz, T. Haensel, R. Gutt, R. J. Koch, J. A. Schaefer, and S. Krischok. Analysis of polar GaN surfaces with photoelectron and high resolution electron energy loss spectroscopy. *Phys. Status Sol. B*, 247(7):1658–1661, May 2010.

- 
- [163] M. Schnedler, P. H. Weidlich, V. Portz, D. Weber, R. E. Dunin-Borkowski, and Ph. Ebert. Correction of nonlinear lateral distortions of scanning probe microscopy images. *Ultramicroscopy*, 136:86–90, 2014.
- [164] V. Bougrov. Properties of Advanced Semiconductor Materials GaN, AlN, InN, BN, SiC, SiGe. In M. E. Levinshtein, S. L. Rumyantsev, and A. Zubrilov, editors, *Gallium Nitride (GaN)*, pages 1–30. John Wiley and Sons, 2001.
- [165] H. Chen, R. M. Feenstra, R. S. Goldman, C. Silfvenius, and G. Landgren. Strain variations in InGaAsP/InGaP superlattices studied by scanning probe microscopy. *Appl. Phys. Lett.*, 72(14):1727, 1998.
- [166] Y. Goldberg. Properties of Advanced Semiconductor Materials GaN, AlN, InN, BN, SiC, SiGe. In M. E. Levinshtein, S. L. Rumyantsev, and M. S. Shur, editors, *Aluminium Nitride (AlN)*, pages 31–47. John Wiley and Sons, 2001.
- [167] A. Zubrilov. Properties of Advanced Semiconductor Materials GaN, AlN, InN, BN, SiC, SiGe. In M. E. Levinshtein, S. L. Rumyantsev, and M. S. Shur, editors, *Indium Nitride (InN)*, pages 49–66. John Wiley and Sons, 2001.
- [168] H. Chen, R. M. Feenstra, P. G. Piva, R. D. Goldberg, I. V. Mitchell, G. C. Aers, P. J. Poole, and S. Charbonneau. Enhanced group-V intermixing in InGaAs/InP quantum wells studied by cross-sectional scanning tunneling microscopy. *Appl. Phys. Lett.*, 75(1):79, 1999.
- [169] R. M. Feenstra. Comparison of electronic and mechanical contrast in scanning tunneling microscopy images of semiconductor heterojunctions. *Physica B*, 273-274:796–802, 1999.
- [170] P. H. Weidlich, M. Schnedler, V. Portz, H. Eisele, U. Strauß, R. E. Dunin-Borkowski, and Ph. Ebert. Tracking the subsurface path of dislocations in GaN using scanning tunneling microscopy. *J. Appl. Phys.*, 118(3), 2015.
- [171] Ph. Ebert, L. Ivanova, S. Borisova, H. Eisele, A. Laubsch, and M. Dähne. Electronic properties of dislocations in GaN investigated by scanning tunneling microscopy. *Appl. Phys. Lett.*, 94(6):062104, 2009.

- [172] P. Quadbeck, Ph. Ebert, K. Urban, J. Gebauer, and R. Krause-Rehberg. Effect of dopant atoms on the roughness of III-V semiconductor cleavage surfaces. *Appl. Phys. Lett.*, 76(3):300, 2000.
- [173] B. Lita, R. S. Goldman, J. D. Phillips, and P. K. Bhattacharya. Nanometer-scale studies of vertical organization and evolution of stacked self-assembled InAs/GaAs quantum dots. *Appl. Phys. Lett.*, 74(19):2824, 1999.
- [174] S. Gaan, G. He, R. M. Feenstra, J. Walker, and E. Towe. Size, shape, composition, and electronic properties of InAs/GaAs quantum dots by scanning tunneling microscopy and spectroscopy. *J. Appl. Phys.*, 108:114315, 2010.
- [175] C. Prohl, B. Höpfner, J. Grabowski, M. Dähne, and H. Eisele. Atomic structure and strain of the InAs wetting layer growing on GaAs(001)-c( $4 \times 4$ ). *J. Vac. Sci. Technol. B*, 28(4):C5E13, 2010.
- [176] F. Genz, A. Lenz, H. Eisele, L. Ivanova, R. Timm, U. W. Pohl, M. Dähne, D. Franke, and H. Künzel. InAs nanostructures on InGaAsP/InP(001): Interaction of InAs quantum-dash formation with InGaAsP decomposition. *J. Vac. Sci. Technol. B*, 28(4):C5E1–C5E7, 2010.
- [177] Ph. Ebert, B. Engels, P. Richard, K. Schroeder, S. Blügel, C. Domke, M. Heinrich, and K. Urban. Contribution of Surface Resonances to Scanning Tunneling Microscopy Images: (110) Surfaces of III-V Semiconductors. *Phys. Rev. Lett.*, 77:2997–3000, Sep 1996.
- [178] B. Siemens, C. Domke, Ph. Ebert, and K. Urban. Steps on CdSe(11 $\bar{2}$ 0) and (10 $\bar{1}$ 0) cleavage surfaces: Evidence for crack propagation in competing cleavage planes. *Phys. Rev. B*, 59:3000, 1999.
- [179] C. Rudhart, H.-R. Trebin, and P. Gumbsch. Crack propagation in perfectly ordered and random tiling quasicrystals. *J. Non-Crystalline Solids*, 334-335:453 – 456, 2004. 8th International Conference on Quasicrystals.
- [180] P. Rinke, M. Winkelnkemper, A. Qteish, D. Bimberg, J. Neugebauer, and M. Scheffler. Consistent set of band parameters for the group-III nitrides AlN, GaN, and InN. *Phys. Rev. B*, 77(15):075202, 2008.

- 
- [181] Y. C. Yeo, T. C. Chong, and M. F. Li. Electronic band structures and effective-mass parameters of wurtzite GaN and InN. *J. Appl. Phys.*, 83(3):1429, 1998.
- [182] M. Suzuki, T. Uenoyama, and A. Yanase. First-principles calculations of effective-mass parameters of AlN and GaN. *Phys. Rev. B*, 52(11):8132, 1995.
- [183] V. W. Chin, T. L. Tansley, and T. Osotchan. Electron mobilities in gallium, indium, and aluminum nitrides. *J. Appl. Phys.*, 75(11):7365, 1994.
- [184] T. L. Chu, D. W. Ing, and A. J. Noreika. Epitaxial growth of aluminum nitride. *Sol. State Electron.*, 10(10):1023–1027, 1967.
- [185] J. Edwards, K. Kawabe, G. Stevens, and R. H. Tredgold. Space charge conduction and electrical behaviour of aluminium nitride single crystals. *Sol. State Commun.*, 3(5):99–100, 1965.
- [186] F. Bernardini, V. Fiorentini, and D. Vanderbilt. Spontaneous polarization and piezoelectric constants of III-V nitrides. *Phys. Rev. B*, 56(16):R10024, 1997.
- [187] O. Ambacher, M. Eickhoff, A. Link, M. Hermann, M. Stutzmann, F. Bernardini, V. Fiorentini, Y. Smorchkova, J. Speck, U. Mishra, W. Schaff, V. Tilak, and L. F. Eastman. Electronics and sensors based on pyroelectric Al-GaN/GaN heterostructures. *phys. stat. sol. (c)*, 0(6):1878–1907, 2003.
- [188] A. E. Romanov, P. Waltereit, and J. S. Speck. Buried stressors in nitride semiconductors: Influence on electronic properties. *J. Appl. Phys.*, 97:043708, 2005.
- [189] A. D. Andreev and E. R. O'Reilly. Theory of the electronic structure of GaN/AlN hexagonal quantum dots. *Phys. Rev. B*, 62(23):15851, 2000.



# List of own publications

Publications included in this thesis in a modified version are marked with asterisks (\*).

- [P1] V. Portz, M. Schnedler, L. Lymperakis, J. Neugebauer, H. Eisele, J.F. Carlin, R. Butté, N. Grandjean, R. E. Dunin-Borkowski, and Ph. Ebert. Fermi level pinning and intrinsic surface states of  $\text{Al}_{1-x}\text{In}_x\text{N}(10\bar{1}0)$  surfaces. *Appl. Phys. Lett.*, 110(2):022104, 2017\*
- [P2] V. Portz, M. Schnedler, M. Duchamp, F.-M. Hsiao, H. Eisele, J.F. Carlin, R. Butté, N. Grandjean, R. E. Dunin-Borkowski, and Ph. Ebert. Strain and compositional fluctuations in  $\text{Al}_{1-x}\text{In}_x\text{N}/\text{GaN}$  heterostructures. *Appl. Phys. Lett.*, 109(13):132102, 2016\*
- [P3] F.-M. Hsiao, M. Schnedler, V. Portz, Y.-C. Huang, B.-C. Huang, M.-C. Shih, C.-W. Chang, L.-W. Tu, H. Eisele, R. E. Dunin-Borkowski, Ph. Ebert, and Y.-P. Chiu. Probing defect states in polycrystalline GaN grown on Si(111) by sub-bandgap laser-excited scanning tunneling spectroscopy. *J. Appl. Phys.*, 121(1):015701, 2017.
- [P4] H. Eisele, J. Schuppang, M. Schnedler, M. Duchamp, C. Nenstiel, V. Portz, Th. Kure, M. Bügler, A. Lenz, M. Dähne, A. Hoffmann, S. Gwo, S. Choi, J. S. Speck, R. E. Dunin-Borkowski, and Ph. Ebert. Intrinsic electronic properties of high-quality wurtzite InN. *Phys. Rev. B*, 49(24):245201, 2016.
- [P5] M. Schnedler, I. Lefebvre, T. Xu, V. Portz, G. Patriarche, J.-P. Nys, S. R. Plissard, P. Caroff, M. Berthe, H. Eisele, R. E. Dunin-Borkowski, Ph. Ebert, and B. Grandidier. Lazarevicite-type short-range ordering in ternary III-V nanowires. *Phys. Rev. B*, 94(19):195306, 2016.

- [P6] M. Schnedler, V. Portz, P. H. Weidlich, R. E. Dunin-Borkowski, and Ph. Ebert. Quantitative laser-excited scanning tunneling spectroscopy on the GaAs(110) surface. *Phys. Rev. B*, 91(23):235305, 2015.
- [P7] M. Schnedler, V. Portz, H. Eisele, R. E. Dunin-Borkowski, and Ph. Ebert. Polarity dependent pinning of a surface state. *Phys. Rev. B*, 91(20):205309, 2015.
- [P8] P. H. Weidlich, M. Schnedler, V. Portz, H. Eisele, U. Strauß, R. E. Dunin-Borkowski, and Ph. Ebert. Tracking the subsurface path of dislocations in GaN using scanning tunneling microscopy. *J. Appl. Phys.*, 118(3):035302, 2015.
- [P9] M. Schnedler, P. H. Weidlich, V. Portz, D. Weber, R. E. Dunin-Borkowski, and Ph. Ebert. Correction of nonlinear lateral distortions of scanning probe microscopy images. *Ultramicroscopy*, 136:86, 2014.
- [P10] P. H. Weidlich, M. Schnedler, V. Portz, H. Eisele, R. E. Dunin-Borkowski, and Ph. Ebert. Meandering of overgrown v-shaped defects in epitaxial GaN layers. *Appl. Phys. Lett.*, 105(1):012105, 2014.

# Acknowledgement

First of all I would like to thank Prof. Dr. R. Dunin-Borkowski for generously giving me the opportunity to prepare my PhD thesis at the Institute for Microstructure Research of the Peter Grünberg Institute at the Forschungszentrum Jülich.

I am especially grateful to Priv.-Doz. Dr. Ph. Ebert for supervising this thesis and for his guidance and support during measurements and the analysis and interpretation of the data.

Furthermore I would like to thank Prof. Dr. T. Taubner from the I. Physikalisches Institut A der RWTH Aachen for the co-supervision. I am also grateful to Prof. Dr. T. Taubner and Dr. F. Gaussmann from the Fraunhofer-Institut für Lasertechnik in Aachen for the performance of the SNOM measurements.

I would like to thank Prof. Dr. N. Grandjean, Dr. R. Butté, and Dr. J.-F. Carlin from École Polytechnique Fédérale de Lausanne, Switzerland for generously providing me with the samples and for their help with the interpretation and assessment of the experimental results.

Moreover I would like to thank Prof. Dr. J. Neugebauer and Dr. L. Lymperakis from the Computational Materials Department at the Max-Planck-Institute für Eisenforschung GmbH for the performance of the DFT calculations.

In addition I would like to thank Dr. M. Duchamp from the Ernst-Ruska-Centre at the Forschungszentrum Jülich for the STEM and electron diffraction measurements.

I also would like to thank Dr. B. Grandidier and J. P. Nys from the Institute d'Electronique, de Microélectronique et de Nanotechnologie in Lille, France for enabling me to perform measurements using their microscopes.

My thanks also go to Prof. Dr. M. Dähne, Dr. A. Lenz, and in particular Prof. Dr. H. Eisele from the Institut für Festkörperphysik at the Technische Universität Berlin for numerous scientific discussions.

For technical support and the maintenance of the technical equipment I would like to thank K. H. Graf.

Furthermore I would like to thank my colleagues and former colleagues Dr. M. Schnedler, Dr. P. H. Weidlich, and M. Sc. F.-M.Hsiao for the companionship and countless scientific discussions.

Moreover my thanks go to my family and friends for their support and patience.

Band / Volume 34

**Structure, electronic properties, and interactions of defects in epitaxial GaN layers**

P. H. Weidlich (2014), 139 pp

ISBN: 978-3-89336-951-5

Band / Volume 35

**Defect Engineering of SrTiO<sub>3</sub> thin films for resistive switching applications**

S. Wicklein (2014), xi, 144 pp

ISBN: 978-3-89336-963-8

Band / Volume 36

**Integration and Characterization of Atomic Layer Deposited TiO<sub>2</sub> Thin Films for Resistive Switching Applications**

M. Reiners (2014), xiv, 166 pp

ISBN: 978-3-89336-970-6

Band / Volume 37

**Resistive switching in ZrO<sub>2</sub> based metal-oxide-metal structures**

I. Kärkkäinen (2014), xviii, 125 pp

ISBN: 978-3-89336-971-3

Band / Volume 38

**Resistive switching phenomena of extended defects in Nb-doped SrTiO<sub>3</sub> under influence of external gradients**

C. Rodenbücher (2014), xiii, 200 pp

ISBN: 978-3-89336-980-5

Band / Volume 39

**Micro-spectroscopic investigation of valence change processes in resistive switching SrTiO<sub>3</sub> thin films**

A. Köhl (2014), viii, 166 pp

ISBN: 978-3-89336-988-1

Band / Volume 40

**Strained Silicon and Silicon-Germanium Nanowire Tunnel FETs and Inverters**

S. Richter (2014), iii, 117 pp

ISBN: 978-3-95806-002-9

Band / Volume 41

**Integration of Redox-Based Resistive Switching Memory Devices**

F. Lentz (2014), i, 166 pp

ISBN: 978-3-95806-019-7

Band / Volume 42

**Ladungstransportuntersuchungen an nanofunktionalen Bauelementen mit Diodencharakteristik basierend auf funktionalisierten Nanopartikeln**

N. Babajani (2015), iv, 138, XLVII

ISBN: 978-3-95806-026-5

Band / Volume 43

**Transport and Noise Properties of Nanostructure Transistors for Biosensor Applications**

J. Li (2015), vii, 175 pp

ISBN: 978-3-95806-034-0

Band / Volume 44

**Quantitative scanning tunneling spectroscopy of non-polar III-V compound semiconductor surfaces**

M. Schnedler (2015), 122 pp

ISBN: 978-3-95806-075-3

Band / Volume 45

**Model-based Algorithm Development with Focus on Biosignal Processing**

Y. Yao (2015), x, 169 pp

ISBN: 978-3-95806-080-7

Band / Volume 46

**Growth and characterization of crystalline rare-earth based thin oxide films for the application as gate dielectric in nanotechnology**

A. B. Schäfer (2015), xiii, 157 pp

ISBN: 978-3-95806-111-8

Band / Volume 47

**TEM/STEM Investigations of Phase Change Materials for Non-volatile Memory Applications**

M. Bornhöfft (2017), viii, 135 pp

ISBN: 978-3-95806-221-4

Band / Volume 48

**Investigation of ternary nitride semiconductor alloys by scanning tunneling microscopy**

V. Portz (2017), 140 pp

ISBN: 978-3-95806-232-0



**Information**  
**Band / Volume 48**  
**ISBN 978-3-95806-232-0**

